



Catalytic Conversion of Biomass-derived C_1 - C_3 Compounds to Value-added Chemicals

Pulikkal Thumbayil, Rouzana

Publication date:
2020

Document Version
Publisher's PDF, also known as Version of record

[Link back to DTU Orbit](#)

Citation (APA):
Pulikkal Thumbayil, R. (2020). *Catalytic Conversion of Biomass-derived C_1 - C_3 Compounds to Value-added Chemicals*. Technical University of Denmark.

General rights

Copyright and moral rights for the publications made accessible in the public portal are retained by the authors and/or other copyright owners and it is a condition of accessing publications that users recognise and abide by the legal requirements associated with these rights.

- Users may download and print one copy of any publication from the public portal for the purpose of private study or research.
- You may not further distribute the material or use it for any profit-making activity or commercial gain
- You may freely distribute the URL identifying the publication in the public portal

If you believe that this document breaches copyright please contact us providing details, and we will remove access to the work immediately and investigate your claim.

DTU Chemistry
Department of Chemistry

Catalytic Conversion of Biomass-derived $C_1 - C_3$ Compounds to Value-added Chemicals

Rouzana Pulikkal Thumbayil

Kongens Lyngby
March 2020



Rouzana Pulikkal Thumbayil

Catalytic Conversion of Biomass-derived C_1 - C_3 Compounds to Value-added Chemicals

Ph.D. Thesis

Department of Chemistry

Technical University of Denmark

Kemitorvet

Building 206

2800 Kongens Lyngby, Denmark

Preface

This thesis is submitted in partial fulfilment of the requirements to obtain the Ph.D. degree at the Technical University of Denmark (DTU). The work was carried out at the Centre for Catalysis and Sustainable Chemistry (CSC) at DTU Chemistry, from May 2016 to February 2020 under the supervision of Professor Søren Kegnæs. This work was supported by research grand 13158 from VILLUM FONDEN. The aim of the project was to synthesise industrially significant chemicals from biomass-derived compounds using heterogeneous catalysis.

First and foremost, I would like to express my sincere gratitude to my main supervisor, Professor Søren Kegnæs for his close guidance, friendly supervision, valuable inputs, encouragement and never-ending support. It was an honour and a pleasure for me to work with him in his research group. I would like to thank my co-supervisor, Senior Researcher Jerrik J. Mielby for his valuable guidance, bright insights, ideas and fruitful discussions. Within the Ph.D. period, I have carried out research work at Haldor Topsøe A/S for three months under the supervision of Senior Scientist Finn Joensen. I am grateful for his relentless support and valuable guidance.

My sincere acknowledgement to the technical staff at CSC. I thank Bodil Fliis Holten for her assistance with physisorption instrument, Maria Blanner Bang and Johanne M. Nielsen for their help with XRD sample analysis and Betina Margrethe Farrington Roesdahl with the ICP-OES instrument. My acknowledgement to the electronic Physical Science Imaging Centre (ePSIC) at Diamond Light Source, UK for STEM-HAADF and EDS images.

I would like to thank Assistant Professor Søren Kramer for his support and guidance in the early part of my Ph.D. I am grateful to Dr. Leonhard Schill for his help with chemisorption experiments. I would also like to thank my fellow Ph.D. colleagues in the Kegnæs group. Some of the work in this project has been carried out in collaboration with them. Special acknowledgement to Dr. Farnoosh Goodarzi

and David B. Christensen for their contributions, help and support in the project. I would like to acknowledge Kristoffer H. Rasmussen and Kai Gao for their help with XPS data. I am deeply grateful to all the colleagues and friends at Catalysis and Sustainable Chemistry (CSC) because you have contributed to making a very pleasant working environment.

My parents, brother, sister and in-law family deserve a particular note of thanks. Despite the distance and seeing each other once a year, their unconditional support, prayer and affection have been fundamental to reach my goals. I want to profoundly thank my soul mate Shihab, for his support, engineering ideas and giving me strength and determination to complete the Ph.D. and for being awake with me for many sleepless nights. Finally, thanks to my two and a half-year-old son, Fayz, for his love and affection. You never complained about me for not spending time with you. Thank you for being such a darling and I promise I will compensate for all the lost fun.

Rouzana Pulikkal Thumbayil

Lyngby, March 3, 2020

Abstract

With the demand for energy-efficient and environmentally friendly processes, chemical industries are moving towards the production of bulk and fine chemicals from renewable resources such as biomass. The transition from fossil to renewable resources is necessary to meet the growing demand for clean energy and chemicals while reducing the CO₂ emission. This thesis aims to investigate and develop new efficient methods to convert biomass-derived compounds to value-added chemicals using heterogeneous catalysts comprising highly active, selective and stable nanostructured materials.

Chapter 1 gives a short description of the challenges with the production of chemicals from non-sustainable sources and introduces biomass-derived chemicals. Furthermore, the chapter presents three biomass-derived platform chemicals, i.e. formic acid, ethanol and acetone, and their potential for production of value-added chemicals. The chapter then addresses the basic concept of heterogeneous catalysis with focus on supported nanoparticles. Furthermore, the chapter highlights how detailed understanding of size, shape and structure can help in the development of new and more efficient heterogeneous catalysts.

Chapter 2 deals with the different porous support used in this thesis. The chapter gives a short introduction to zeolites and ordered mesoporous carbon and describes briefly general strategies to improve the efficiency in heterogeneous catalysis. Furthermore, the chapter describes the synthesis methodology of various porous support used in this work.

Chapter 3 deals with the major analytical techniques used to characterise catalytic materials. The techniques include: X-ray powder diffraction, nitrogen physisorption, electron microscopy, temperature-programmed desorption, elemental analysis, X-ray photoelectron spectroscopy, diffuse reflectance infrared Fourier transformation spectroscopy and thermo-gravimetric analysis.

Hydrogen holds great promise for resolving the storage of intermittent and highly weather-dependent renewable energy. Chapter 4 describes a novel heterogeneous catalytic system for the continuous production of hydrogen through the decomposition of formic acid. The reaction occurs over a heterogeneous bimetallic catalyst comprising Pd-Au metal nanoparticles encapsulated in zeolite silicalite-1. The chapter describes different methods to support gold on silicalite-1 and identifies an optimum catalyst for the efficient production of hydrogen via decomposition of formic acid.

Acetaldehyde is an organic intermediate used commercially as a food preservative and an ingredient in fuels, glues, and caulking compounds. Chapter 5 describes an efficient synthesis of acetaldehyde from the dehydrogenation of ethanol. The reaction occurs over a heterogeneous catalyst comprised of Cu nanoparticles supported on nitrogen-doped ordered mesoporous carbon. The chapter studies the effect of nitrogen doping on the mesoporous carbon support and identifies the optimum catalyst for the synthesis of acetaldehyde. The chapter also investigates the catalytic effect of important synthetic parameters, such as polymerisation and calcination temperature.

1,3-Butadiene is an important chemical intermediate used in synthetic rubber and polymers. Chapter 6 describes a method to synthesise 1,3-butadiene from ethanol using a heterogeneous catalyst comprised of Zn containing zeolite. The chapter describes the effect of the zeolite morphology on butadiene selectivity and ethanol conversion and identifies the optimum catalyst for ethanol to butadiene conversion.

Methyl isobutyl ketone (MIBK) is an organic solvent used for the production of gums, paints and varnishes. Chapter 7 describes a novel one-step synthesis of MIBK from acetone at 150 °C and atmospheric pressure in a fixed bed continuous flow set-up. The reaction occurs over a heterogeneous bifunctional catalyst comprised of Pd nanoparticles supported on HZSM-5 zeolite. The chapter describes incipient wetness impregnation and in-situ encapsulation methods to support Pd nanoparticles in conventional and mesoporous zeolite and identifies the optimum catalyst for MIBK synthesis.

Dansk Resumé

Grundet de stigende krav til energi effektive og miljøvenlige processer styrer den kemiske industri sig imod en kemikalieproduktion, der er baseret på fornybare ressourcer såsom biomasse. Overgangen fra fossile til vedvarende ressourcer er nødvendig for at imødekomme den voksende efterspørgsel efter ren energi og miljøvenlige kemikalier, samtidig med at CO₂ udledningen reduceres. Formålet med denne afhandling er at undersøge og udvikle nye effektive metoder til at omdanne biomasse-baserede udgangsstoffer til mere værdifulde kemikalier vha. heterogene katalysatorer, der består af højaktive, selektive og stabile nano-strukturerede materialer.

Kapitel 1 giver en kort beskrivelse af udfordringerne ved kemikalier fra ikke-bæredygtige ressourcer og introducerer bio-baserede kemikalier. Efterfølgende præsenteres der tre bio-baserede kemikalier, herunder myresyre, ethanol og acetone, og deres potentiale for produktion af mere værdifulde kemikalier. Kapitlet fokuserer herefter på det grundlæggende koncept bag heterogen katalyse med fokus på nanopartikler og bærermaterialer. Endvidere fremhæver kapitlet, hvordan partikelstørrelse, form og struktur kan hjælpe med udviklingen af nye og mere effektive heterogene katalysatorer.

Kapitel 2 handler om de forskellige porøse bærermaterialer, der er anvendt i denne afhandling. Kapitlet giver en kort introduktion til zeolitter og ordnede mesoporøse carbon materialer, og beskriver kort generelle strategier til at forbedre effektiviteten i heterogen katalyse. Efterfølgende beskrives de syntese metoder, der er anvendt til at fremstille de forskellige porøse materialer, som er brugt i dette projekt.

Kapitel 3 handler om de vigtigste analyse metoder, der er brugt til at karakterisere katalysatorerne. Blandt de anvendte teknikker er X-ray pulver diffraktion, nitrogen fysisorption, elektronmikroskopi, temperaturprogrammeret desorption, elementar analyse, røntgenfotoelektronspektroskopi, diffus reflektants infrarød Fourier transformeret spektroskopi og termo-gravimetrisk analyse.

Hydrogen kan spille en vigtig rolle i at løse problemet med oplagring af intermitterende og meget vejrafhængig bæredygtig energi. Kapitel 4 giver en beskrivelse af et nyt heterogent katalytisk system til kontinuerlig produktion af hydrogen ved omdannelse af myresyre. Reaktionen forløber vha. en bimetallisk katalysator, der består af zeolit-indkapslede Pd-Au nanopartikler. Kapitlet beskriver forskellige metoder til at fastgøre Au på silicalite-1 zeolit og identificerer den optimale katalysator til effektiv produktion af hydrogen ved omdannelse af myresyre.

Acetaldehyd er et organisk intermediat, der kommercielt anvendes som et fødevarekonserveringsmiddel og en ingrediens i brændstoffer, lim og blødgøringsforbindelser. Kapitel 5 beskriver en effektiv syntese af acetaldehyd ved dehydrogenering af ethanol. Reaktionen forløber vha. en heterogen katalysator, der består af Cu nanopartikler fastgjort på et nitrogen-dopet ordnet mesoporøs carbon materiale. Kapitlet undersøger effekten af nitrogen doping på den mesoporøse bærermateriale og identificerer den optimale katalysator til syntese af acetaldehyd. Kapitlet undersøger også den katalytiske effekt af vigtige syntese parametre såsom polymerisering- og carboniseringstemperatur.

1,3-Butadien er et vigtigt kemisk intermediat, der anvendes i syntetisk gummi og polymere. Kapitel 6 beskriver en metode til syntese af 1,3-butadien fra ethanol vha. en heterogen katalysator, der består af en zeolit indeholdende Zn. Kapitlet beskriver indflydelsen af zeolitternes morfologi på omdannelse og selektivitet og identificere den optimale katalysator for omdannelse af ethanol til 1,3-butadien.

Methyl isobutyl keton (MIBK) er et organisk solvent, der anvendes i produktionen af klæbemidler, maling og lakker. Kapitel 7 beskriver en ny et-trins syntese af MIBK fra acetone ved 150 °C og atmosfærisk tryk i et kontinuert flow set-up. Reaktionen forløber vha. heterogene bifunktionelle katalysatorer, der består af Pd nanopartikler indkapslet i HZSM-5 zeolitter. Kapitlet beskriver to metoder, herunder incipient-wetness imprægnering og in-situ indkapsling, til at fremstille Pd nanopartikler i konventionelle og mesoporøse zeolitter og identificerer den optimale katalysator til syntese af MIBK.

Contents

Preface	i
Abstract	iii
Dansk Resumé	v
Contents	vii
1 Introduction	1
1.1 Biomass to value-added chemicals	1
1.1.1 Bio formic acid	3
1.1.2 Bioethanol	3
1.1.3 Bioacetone	5
1.2 Heterogeneous catalysis	5
1.3 Catalysis with supported nanoparticles	6
1.4 Summary	8
2 Porous Supports	9
2.1 Introduction	9
2.2 Zeolites	10
2.2.1 Catalysis with zeolite	11
2.2.2 Diffusion in zeolite micropores	13
2.2.3 Mesoporous zeolites	14
2.2.4 Synthesis of zeolites	16
2.3 Mesoporous carbon	18
2.3.1 Ordered mesoporous carbon	18
2.3.2 Nitrogen-doped ordered mesoporous carbon	20
2.4 Summary	20
3 Charecterisation Techniques	23
3.1 Introduction	23
3.2 X-ray powder diffraction	23
3.3 Nitrogen physisorption	24
3.4 Electron microscopy	28

3.4.1	Scanning electron microscopy	29
3.4.2	Transmission electron microscopy	30
3.5	Ammonia temperature-programmed desorption	32
3.6	Hydrogen temperature programmed reduction	33
3.7	Elemental analysis	33
3.7.1	Energy dispersive X-ray spectroscopy	33
3.7.2	Inductively coupled plasma-optical emission spectroscopy	34
3.7.3	X-ray photoelectron spectroscopy	34
3.7.4	CHN analysis	34
3.8	In-situ diffuse reflectance infrared Fourier transform spectroscopy	35
3.9	Thermo-gravimetric analysis	35
3.10	Summary	35
4	Decomposition of Formic acid	37
4.1	Introduction	37
4.2	Experimental Section	40
4.2.1	Materials	40
4.2.2	Synthesis of materials	41
4.2.3	Characterisation	42
4.2.4	Gas-phase dehydrogenation of formic acid	43
4.3	Results and discussions	43
4.3.1	Characterisation results	43
4.3.2	Catalytic activity	50
4.4	Summary	56
5	Selective Conversion of Ethanol to Acetaldehyde	57
5.1	Introduction	57
5.2	Experimental Section	60
5.2.1	Materials	60
5.2.2	Synthesis of materials	60
5.2.3	Characterisation	62
5.2.4	Gas-phase conversion of bioethanol to acetaldehyde	62
5.3	Results and discussions	63
5.3.1	Characterisation results	63
5.3.2	Catalytic activity	73
5.4	Modification to mesoporous carbon for improved catalytic performance	83
5.4.1	Characterisation results	84
5.4.2	Catalytic activity	88
5.5	Summary	90
6	One-step Conversion of Ethanol to Butadiene	91
6.1	Introduction	91
6.2	Experimental section	94
6.2.1	Materials	94

6.2.2	Synthesis of materials	94
6.2.3	Charecterisation	94
6.2.4	Gas-phase conversion of bioethanol to butadiene	95
6.3	Results and discussions	96
6.3.1	Characterisation results	96
6.3.2	Catalytic activity	101
6.4	Summary	106
7	One-step Conversion of Acetone to MIBK	107
7.1	Introduction	107
7.2	Experimental section	109
7.2.1	Materials	109
7.2.2	Synthesis of materials	110
7.2.3	Charecterisation	111
7.2.4	Gas-phase conversion of acetone to MIBK	111
7.3	Results and discussions	112
7.3.1	Characterisation results	113
7.3.2	Catalytic activity	118
7.4	Summary	124
8	Conclusion	125
	Bibliography	127
A	Publications and Disseminations	143
B	Declaration of Co-authorship	145

CHAPTER 1

Introduction

As a consequence of stringent environmental regulations on reducing the greenhouse gases and demand for developing energy-efficient sustainable solutions, conversion of biomass-derived compounds to value-added chemicals hold great promises for the future of the chemical industry. This chapter gives a short introduction to the significance of biomass-derived chemicals and introduces three biomass-derived platform chemicals, i.e. formic acid, ethanol and acetone, and their potential for production of value-added chemicals. The chapter then addresses the basic concept of heterogeneous catalysis with focus on supported nanoparticles. Furthermore, the chapter highlights how detailed understanding of size, shape and structure can help in the development of new and more efficient heterogeneous catalysts.

1.1 Biomass to value-added chemicals

The enormous fossil fuel consumption has generated major environmental challenges such as increased CO₂ emission and global warming. The ultimate solution to overcome the impact caused by fossil fuel consumption is to produce chemicals and fuels from renewable resources [1, 2]. Biomass has been discussed as an alternative carbon source to fossil reserves to meet the growing demand for clean energy and chemicals while reducing the CO₂ emission. Conversion of biomass to fuels and chemicals via microbial fermentation process can resolve the effect caused by the accumulation of greenhouse gases and can provide a viable route to relieve our robust dependence on fossil fuel supplies [1, 3]. Numerous ongoing researches on biomass conversion points towards the development of the biomass-based long-term solution for the prevailing scenario on fossil fuels [4, 5]. The prospect of bio-based chemicals in the European bioeconomy emphasizes EU's collective target to accelerate the deployment of a sustainable bioeconomy via achieving more innovative and low-emissions economy. The solution to meet the target is by utilising the

renewable biological resources for industrial purposes while ensuring the biodiversity and environmental protection [3, 6–8].

Conversion of biomass-derived compounds to value-added chemicals is one of the hot topics in current researches. The key stage to utilize biomass depends on the effectiveness of the chemical processes like hydrolysis, pyrolysis, dehydrogenation, etc. [9]. For instance, hydrolysis/dehydration of cellulose and hemicellulose produces two important platform molecules, 5-hydroxymethylfurfural (HMF) and furfural. Likewise, catalytic biorefinery offers a variety of chemicals including alcohols, aldehydes and hydrocarbons [9–11]. Figure 1.1 shows the list of chemicals produced from biomass.

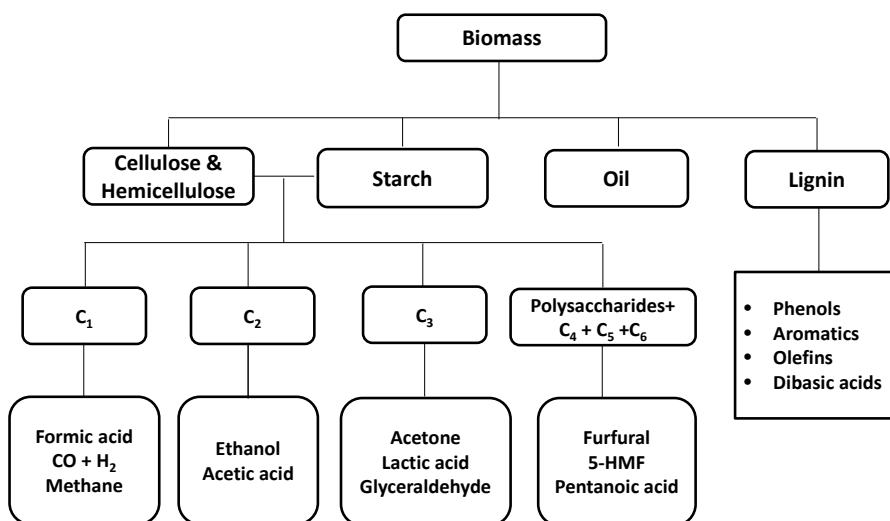


Figure 1.1: Conversion of biomass to value-added chemicals.

Biomass-derived chemicals can help to replace a large fraction of industrial chemicals and materials from fossil resources. Biomass-derived chemicals, such as 5-HMF, levulinic acid, furfural, alcohols, lactic acid, succinic acid, and phenols, are excellent platform chemicals, which can be further used for the production of an extensive range of important chemicals on an industrial scale [12–14].

This thesis focuses on the conversion of biomass-derived C_1 (formic acid), C_2 (ethanol) and C_3 (acetone) to value-added chemicals such as hydrogen, acetaldehyde, 1,3-butadiene and methyl isobutyl ketone.

1.1.1 Bio formic acid

Formic acid, the simplest carboxylic acid with the chemical formula HCOOH , is widely used in the pharmaceutical, chemical and textile industries [15]. Recently, formic acid is proposed as a sustainable hydrogen source, serving a platform for chemical energy storage. Formic acid is produced through carbonylation of methanol to methyl formate followed by hydrolysis and acidolysis of alkyl formate [16]. However, both methods use fossil fuel raw materials.

There are many research outcomes proposing commercialization of formic acid production from biomass derivatives, some of which include:

1. Acid hydrolysis of biomass-based carbohydrate [13].
2. Hydrothermal oxidation of carbohydrate [17].
3. Electrochemical transformation of carbohydrate [18].

The chemical reaction for the conversion of carbohydrate to formic acid is shown below.

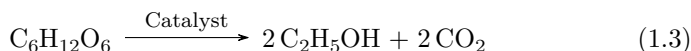
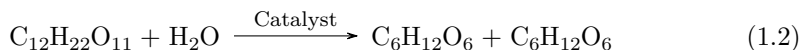


Bio formic acid can be used as a potential chemical hydrogen storage material. Hydrogen can offer a clean alternative to fossil fuels and can provide an efficient energy storage solution for the intermittent renewable energy sources. The solution can ultimately lead the way for developing low-cost and highly efficient rechargeable hydrogen fuel cells. Chapter 4 describes decomposition of formic acid to produce hydrogen and CO_2 using heterogeneous catalysis.

1.1.2 Bioethanol

Of many biomass derivatives, bioethanol got high attention for its easy way of production [2]. Owing to the wide range of applications, technologies for producing cost-effective bioethanol is expected to enhance rapidly [31]. Bioethanol is typically made via fermentation of first-generation feedstock such as carbohydrate. The fermentation process breaks down the cellulosic part of the biomass into glucose and fructose with the help of yeast. The process then follows the conversion of fructose and glucose sugars to ethanol and carbon dioxide. The chemical reaction for this

process is shown below.



The feasibility of production is questioned by the feedstock used whether it is a food-based or non-food based. However, results has shown that other types of feedstocks of lignocellulosic biomass such as agricultural and forestry residues could serve as feedstocks for the production of bioethanol [5, 19, 22].

With the annual production of bioethanol in 2017 over 100 billion litres, bioethanol is extensively used as fuel, fuel additive and intermediate for chemical synthesis [19, 20]. Some of the value-added chemicals that can be synthesised from bioethanol are shown in Figure 1.2 [21]. However, bioethanol produced in the majority of the cases is not absolute and contains a high amount of water (as for example 90% water when formed by fermentation). This limits its application where pure ethanol is required. The cost-effective approach to utilise bioethanol is to convert bioethanol to value-added chemicals through reactions that are not sensitive to the water content as for example in synthesis of acetaldehyde and 1,3-butadiene [6, 22–25].

Acetaldehyde is used for the production of acetic acid, ethyl acetate, acetic anhydride, pyridine, vinyl acetate and other commercially important products [26, 27]. Currently, acetaldehyde is produced via Hoechst-Wacker process and utilises oxidation of ethylene (non-renewable feedstock) via homogeneous catalysis like PdCl_2 , chromite and other hazardous materials in a corrosive acidic solution. Chapter 5 describes a method to synthesis acetaldehyde from dehydrogenation of ethanol.

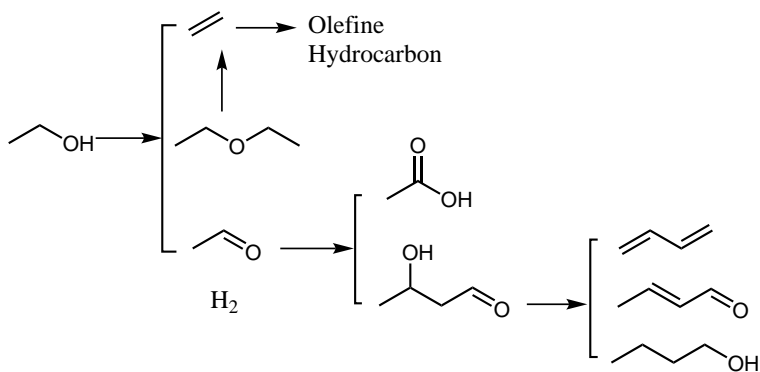


Figure 1.2: Bioethanol to value-added chemicals.

1,3-Butadiene is an important chemical which can be also synthesised from bioethanol. 1,3-Butadiene is a versatile raw ingredient used to produce a variety of synthetic rubber, polymer resins and intermediate in chemical synthesis [6, 21, 28]. Currently, more than 95% of 1,3-butadiene is produced from crude C_4 component of steam cracking. Global market value for 1,3-butadiene is expected to reach a value of around USD 33.5 billion over the forecast period from 2017 to 2024, due to the huge demand of tyres in growing automobile sector [29]. Chapter 6 describes a method to convert ethanol to 1,3-butadiene.

1.1.3 Bioacetone

Acetone is commonly used as a solvent in the pharmaceutical industry, laboratory, paint, plastics synthesis, resins, etc. Acetone also acts as an intermediate solvent for industrially important chemicals [30]. Fortunately, acetone can be synthesised from carbohydrates and starch using acetone–butanol–ethanol (ABE) fermentation process with the aid of certain microorganism (clostridia), which results in the formation of acetone, butanol and ethanol. This process was among the very first biofuel production processes commercialized during the First World War [6, 21, 31, 32].

Bioacetone can be used to produce methyl isobutyl ketone (MIBK), a low volatile intermediate solvent used for resins, paints, varnishes, lacquers, etc. Because of low solubility in water, it is useful for solvent extraction and shows greater stability towards aqueous acid and base [33]. Chapter 7 describes a method to synthesise MIBK from acetone.

1.2 Heterogeneous catalysis

Catalysis plays a significant role to meet the increasing demands for sustainable chemical industry by converting biomass derivatives to value-added chemicals in an efficient and environmentally friendly way. Catalysis is employed in all its forms in a wide range of industries, from refineries to pharmaceuticals and commodity chemicals to energy conversion. Studies show that around 60% of all chemical products utilise catalysts in at least one step of their manufacturing cycle [34–36].

A catalyst in a reaction enhances the rate of a reaction by providing an alternative reaction pathway that requires less energy to reach the transition state [12, 35]. Moreover, catalysts can increase the rate of formation of one specific product by

improving the selectivity. The activity of the catalyst is specified using turnover frequency (TOF). TOF is the number of revolutions of the catalytic cycles per unit time.

$$TOF = \frac{\text{moles of substrate converted}}{\text{moles of active sites} \times \text{time}} \quad (1.4)$$

The efficiency of the catalyst is a measure of the number of cycles observed before the catalyst dies [37, 38]. This number must be larger than unity; otherwise, the substance used becomes a reagent instead of the catalyst. For true catalysis, the complete cycle shall happen with no interruptions in a single reaction.

Catalysis are classified into homogeneous, heterogeneous and bio-catalysis. Bio-catalysis takes place in biological systems in the presence of natural catalysts, e.g. enzymes. Heterogeneous catalysis refers to the form of catalysis where the catalyst and reactant are in different phases. In contrary, homogeneous catalysis has both reactant and catalyst in similar phase [39]. Although catalyst tuning is simpler in homogeneous catalysis and has no mass and heat transfer limitations as compared to heterogeneous catalysis, it has a major drawback of challenge in separating the catalyst from product post reaction [40–42]. On the other hand, heterogeneous catalysis are often less active, difficult to tune and often can be challenging for the application of traditional organic reactions.

1.3 Catalysis with supported nanoparticles

Nanoparticles are denoted to the materials having at least one dimension less than 100 nm and consists of clusters with ten to several thousands of metal atoms. The small size and large surface area of nanoparticles hold distinctive physical and chemical properties, which are different from the corresponding bulk component. The size, structure, composition and shape of these particles significantly effect the toughness, reactivity, optical and catalytic properties [43]. Consequently, in last decade, the catalytic activity of nanoparticles is explored in many studies. Few examples are listed in Table 1.1. Due to high degree of exposed active site, they often agglomerate to form large particles with low surface area. This results in the availability of less number of active sites for catalysis or deactivation of the nanoparticles.

In order to achieve highly active and stable nanoparticles, nanoparticles are often supported on porous high surface area support materials. The support can be chemically active or inert. These porous surfaces can affect the chemical and

Table 1.1: Catalytic activity of nanoparticles.

Nanoparticles	Size(nm)	Reaction	Selectivity	Reference
Au	1-3	Oxidation of alcohol	99	[44]
Au	1,5-2,5	Hydrogen evolution	99	[45]
Pd	1.6	Suzuki coupling reaction	90-95	[46]
Pd	7-10	Sonogashira coupling	99	[46]
Pd	1.4	Formic acid dehydrogenation	99	[47]

physical properties of nanoparticles, which in turn can influence the catalytic activity of nanoparticles.

The support materials play a vital role in heterogeneous catalysis. A support with the large surface area can assist the dispersion of small nanoparticles. The large surface area of support and the small and well-dispersed nanoparticles helps to keep them separated from each other resulting in the stabilisation of nanoparticle from sintering under harsh reaction conditions [43]. The support materials can be classified based on the pore size as micro, meso and macroporous for the pore sizes <2 nm, 2-50 nm and >50 nm, respectively. A detailed description of the porous support is given in Chapter 2.

The catalytic activity of supported nanoparticles also depends on shape and size of nanoparticles and nature of metal nanoparticles. Although it may not be possible to determine the direct dependency between the shape and size of nanoparticles with the activity and selectivity of heterogeneous catalysis, the utilisation of the potential of nanoparticles lies in the control of the particle sizes. The target for the optimum size regime is 1-10 nm in which the nanoparticles are dispersed wide apart [46, 48]. The size of nanoparticles can be controlled by the methods used for the immobilization of nanoparticles [49]. The smaller the nanoparticles, the higher the surface energy and therefore the higher the activity is.

Supported nanoparticles are commonly synthesised using precipitation and impregnation methods. In the precipitation method, a metal salt solution is used as a nanoparticle precursor. Precipitation can be carried out either via co-precipitation or deposition precipitation. If the precipitation of metal nanoparticle precursor and support are mixed together and the nucleation and growth of both solid support and nanoparticle occurs in a single step, it is called as co-precipitation. In deposition precipitation method, the deposition of metal on the solid support is induced by

factors such as temperature, pH etc. The co-precipitation method is called as in-situ synthesis if the synthesis of support and nanoparticles occur together as one-pot method [50]. In the impregnation method, the metal precursor (metal salt solution) is diluted in an appropriate amount of solvent and mixed with the support followed by drying and calcination. The precursor solution is added to the support just enough to fill the pores of the support for incipient wetness impregnation.

Nanoparticles are dispersed on porous support to obtain small nanoparticles with adjustable porosity. Normally, the interaction between metal nanoparticles and support is a beneficial factor for the activity of the catalyst. Recent work by Tom et al. reported a four-fold product enhancement by tuning the interaction between metal nanoparticles and support. Nanoparticles supported on acidic or basic support can function as a bifunctional catalyst [51, 52]. In a bifunctional catalyst, two different catalytic sites can catalyze two independent reactions. One of the most important advantages of these types of system is that the highly reactive intermediate formed by one site can readily convert to the most desirable product without being deposited as a carbonaceous substance. Therefore, the stability of the catalysts and the selectivity of the products can be improved substantially. Additionally, the number of reaction steps such as separation, filtration or purification for each product can be reduced, which can lower the cost of the process significantly. For instance, Xiaoliang et al. reported a bi-functional catalyst Zn-ZrO_2 supported on SSZ-13 for the direct conversion of syngas in to lower olefin via methanol with 87% selectivity [53]. However, optimising reaction temperature, pressure and other reaction conditions for each consecutive step to obtain the best possible yield could be a challenging task.

1.4 Summary

To summarise, heterogeneous catalysis can provide a viable and efficient solution to convert biomass-derived compounds to value-added chemicals. The development of new and more efficient heterogeneous catalysts requires understanding of size, shape and structure of the materials. This Ph.D. thesis aims at synthesising industrially significant chemicals from biomass-derived compounds by utilising the high catalytic performance of nanoparticles supported on porous supports.

CHAPTER 2

Porous Supports

The nanoparticles are often supported on a porous and high surface area support materials to achieve highly active and stable heterogeneous catalysts. This chapter provides an introduction to two types of porous support materials such as zeolites and ordered mesoporous carbon used in this Ph.D. work. The support materials were used to immobilise nanoparticles. The chapter gives a general overview of the properties of zeolites and ordered mesoporous carbon. Later, the chapter describes the synthesis methods of porous materials used in Chapter 4 to 7.

2.1 Introduction

Heterogeneous catalysts often consists of nanoparticles supported on a porous and high surface area support materials to achieve highly active and stable catalysts as discussed in Chapter 1. Generally, the expensive transition metal nanoparticles are required to be dispersed on a bulk and cheap porous oxide with high surface area to investigate their catalytic activity, selectivity and efficiency [54]. This immobilization of nanoparticles essentially improves the surface-to-volume ratio of the active phase of the catalysts and makes the catalysts applicable for commercial application. The immobilisation of nanoparticles on porous support makes the catalytic system to be reusable and stable under harsh condition [39]. A porous material is mainly composed of an interconnected system of pores which are solid in its nature. Generally, the porosity of a porous material (microporous, mesoporous, macroporous or combination of any) is one of the determining factors for catalytic application. Other factors include its textural and physico-chemical properties [55].

Two types of porous support used as part of this thesis (HZSM-5 zeolite and ordered mesoporous carbon) are described in the following sections.

2.2 Zeolites

Zeolites are a class of aluminosilicates characterised by a well-defined crystal structure integrated with pore or cavities of molecular dimension. Structurally, zeolites consist of tetrahedral TO_4 units of silicon or aluminium that are interconnected via an oxygen atom to form a large three-dimensional framework. Generally, zeolite consists of silicon, oxygen and aluminium, but materials with a similar structures and different elements such as gallium and phosphorous are also possible. This class of materials is recognized as zeotypes. A typical zeolite is characterized by a pore width in the range of 3 to 7 Å [35].

Zeolites can be considered as an assemblage of numerous small building units. These small units are known as the secondary building units (SBU) that can be arranged in many regular and repeating forms and can consist maximum up to 16T atoms by oxygen linkage. Figure 2.1 gives an illustration of SBU for MFI zeolite having 12T atoms [56]. The arrangement of these building units results in the formation of many well-ordered and unique zeolites. The pore diameter in the zeolite crystal is determined by the number of T-atoms involved in forming the ring surrounding the pores. Depending on the number of T-atom (ring size), zeolites are categorized into four groups. i.e. small-pore zeolites with T-atoms upto 8, medium-pore zeolites with T-atoms upto 10, large-pore zeolites with T-atoms upto 12 and extra-large pore zeolites with T-atoms more than 12 [57]. As more than 200 zeolites are known today, the International Union of Pure and Applied Chemistry Commission (IUPAC) assigned a unique three-letter code to distinguish between different structures of zeolite. This three-letter code only considers the structural parameters and not the chemical composition of the framework. For instance, the well-known ZSM-5 zeolite belongs to MFI, which is an abbreviation for mordenite

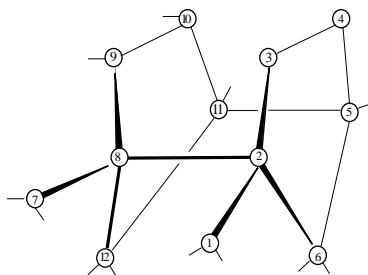


Figure 2.1: SBU of MFI zeolite with 12T atoms.

framework inverted [58].

Figure 2.2 shows the build-up of an MFI framework zeolite from tetrahedral TO_4 units. The MFI structure can be defined from the arrangement of six SBU5-1 tetrahedra with the SBU5-1 groups combined to form pentasil subunits which further form pentasil chains. These pentasil chains interconnected by the oxygen bridge forms the layers of tetrahedra consists of 10-ring holes [59].

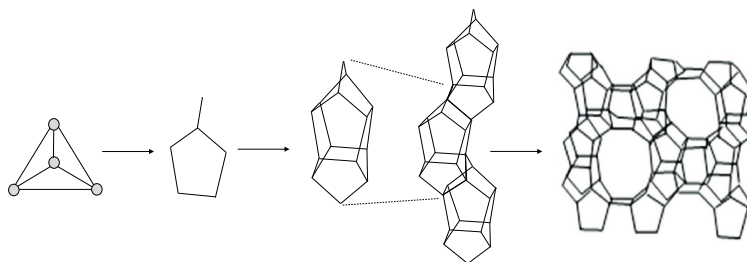


Figure 2.2: Construction of MFI framework from an SBU [57].

2.2.1 Catalysis with zeolite

Zeolites are widely used as industrial catalysts for wide application including in petrochemical industry, chemical industry, catalysts in environmental applications etc. Zeolites work as catalysts due their molecular porosity and ability to provide an acidic site. The presence of trivalent Al in the zeolite framework introduces a charge deficiency that needs to be compensated by a cation. These extra cations can be an alkali or alkaline-earth metal ions or in principle any cations with a small size that can fit into the micropores of zeolites channels. The cation is exchanged with a proton to provide an acidic property, thereby making the zeolite to act as a solid acid catalyst [35, 52]. Figure 2.3 shows the protonated zeolite with Brønsted acid sites. The proton is connected to the oxygen atoms bridging between Si and Al atoms.

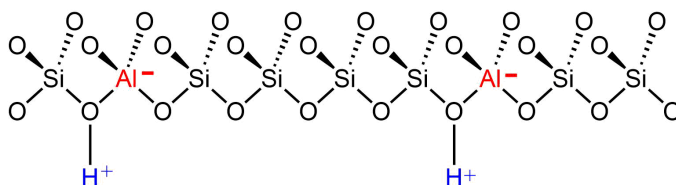


Figure 2.3: Illustration of Brønsted acid sites in an Al containing zeolite.

The acidity of the zeolite depends on the Si/Al or $\text{SiO}_2/\text{AlO}_2$ ratio and therefore the degree of Al substitution. Zeolites are classified into low silica, intermediate silica and high silica zeolites based on Si/Al ratio of 1 to 1.5, 1.5 to 10 and above 10, respectively. The Si/Al ratio in a zeolite cannot be smaller than unity due to Lowenstein's rule, i.e., Al-O-Al linkage is forbidden in a zeolite framework [37, 60, 61]. Zeolite with no Al such as silicalite-1 is a non-acidic zeolite with Si/Al ratio of ∞ . Other heteroatoms such as Ga, Fe, B or Ge can be also introduced in the zeolite structure instead of Al to tune Brønsted acidic strength. The strength of Brønsted acid sites follows the order $\text{Ge} < \text{B} < \text{Fe} < \text{Ga} < \text{Al}$. On the other hand, the substitution of Ti or Sn can be incorporated to introduce redox property or Lewis acidity in zeolites [62, 63].

The inherent property of the micropore system throughout the crystals enables the zeolite to become shape-selective. This shape selectivity, also known as the molecular sieve effect, is particularly important for the catalytic application. In other words, certain catalytic application of zeolites can be achieved through the reactive separation process wherein only a few molecules are allowed to enter the reactive interior part of zeolites [64]. Therefore, in such systems, only certain molecules penetrate through the microporous active part of zeolites. In general, zeolite can induce three types of shape selectivity.

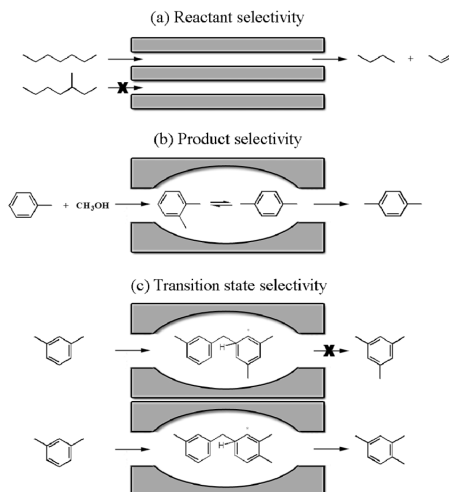


Figure 2.4: Illustration of different shape selectivity in zeolite. The figure was adapted from [65].

1. *Reactant selectivity*: Reactant selectivity occurs when only certain molecules can diffuse through the pores and undergo reaction at the catalytically active sites.
2. *Product selectivity*: Product selectivity occurs when, out of several possible products, only products with certain dimensions can diffuse out of the pores.
3. *Restricted transition-state selectivity*: In this case, certain reactions are prevented as the corresponding transition state would fit in the pores of zeolite.

Figure 2.4 is an illustration of three types of shape selectivity in zeolites. In summary, the shape selectivity enables the zeolite to give better selectivity of the desired product.

2.2.2 Diffusion in zeolite micropores

The inherent micropore system in zeolites is the fundamental reason for their many remarkable properties. Nevertheless, this microporous structure can induce diffusion limitation and can act as a barrier for its application. The reason for diffusion limitation is the constant contact of reactant and product molecules on the pore walls when the molecules are having the same size as that of pores. This results in a lower diffusion rate through the channels of zeolites. This diffusion rate often referred to as the rate of intracrystalline diffusion, can be orders of magnitude lower than molecular or Knudsen diffusion. Consequently, this can result in poor utilisation of the zeolite catalysts [35, 66]. The slow transport of products from the active sites can also lead to the formation of unwanted by-products which can result in the deactivation of catalysts. The utilisation of catalysts is defined by effectiveness factor, η , which is given by the equation

$$\eta = \frac{\tanh\phi}{\phi} \quad (2.1)$$

where

ϕ is the Thiele modulus. The value of η approaches unity when ϕ reduces. ϕ for a first order reaction is given by the equation

$$\phi = \sqrt{\frac{k}{D_e/L^2}} \quad (2.2)$$

where

k is the reaction rate constant

D_e is the effective diffusivity

L is the diffusion path length

A lower ϕ can be obtained either by increasing the D_e or by decreasing the L .

The effective diffusivity (D_e) in zeolites can be improved by increasing the pore size of zeolites. Several zeolites with larger pore sizes and having more than 12 T-atoms are synthesised over the last decades [67]. However, in addition to higher cost, these zeolites in most cases had to compromise on catalytic properties such as stability, selectivity and activity [68].

The second method to improve the effectiveness factor (η) is to decrease the diffusion path length (L). This can be achieved either by decreasing the size of zeolite crystal or by introducing additional mesopores and/or macropores systems. Nanosized zeolites often suffer from low crystalline yield and challenges with scaling up and separation [68]. On the other hand, several works were reported to synthesise mesoporous zeolites due to their potential to combine fast diffusion of mesoporous materials and the higher catalytic performance of microporous zeolites [64, 69–73].

2.2.3 Mesoporous zeolites

Mesoporous zeolites are synthesised using two different approaches. In the first approach, also known as the top-down approach, the microporous zeolite crystals are modified via demetallation or steaming. Here, mesopores are made by removing some parts of the zeolite structure. Desilication and dealumination are generally employed for the demetallation. In desilication method, zeolite is treated with a dilute base under moderate temperature. This method is relatively cheap and the porosity can be easily controlled by adjusting pH, temperature, concentration of base, etc [74]. However, the degree of desilication is highly inclined by the Si/Al ratio of zeolites and often results in a low yield of below 50% of parent zeolite. Figure 2.5 shows the different degrees of mesoporosity using NaOH.

The bottom-up approach to synthesise mesoporous zeolite is by manipulating the crystallisation process through secondary templating. This method involves the application of solid materials to direct the creation of additional porosity during the zeolite crystallisation. Several materials are used as templates in this method.

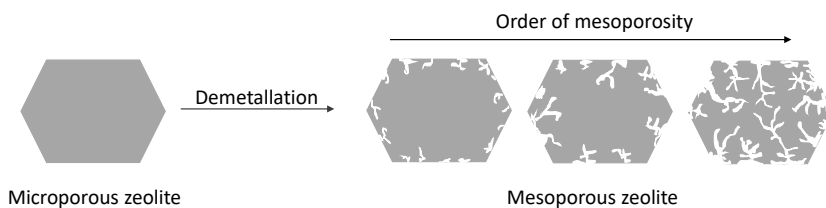


Figure 2.5: Demetallation of zeolite by NaOH.

There are two major subgroups of this approach based on the template material used. Templating with carbon black, carbon nanofibers, aerogel etc. are known as hard templating whereas templating with surfactant or polymer is referred to as soft templating. Preparation of mesoporous zeolite by carbon templating is shown in Figure 2.6. The method developed by Haldor Topsøe involves the nucleating zeolite precursors inside a carbon material. The zeolite then grows and encapsulate the carbon. The carbon template is finally removed by combustion after complete crystallisation to produce the mesoporous zeolite. The template-assisted method results in the formation of very high mesoporous volume together with micropores and can be easily controlled by choosing different templates [52, 75].

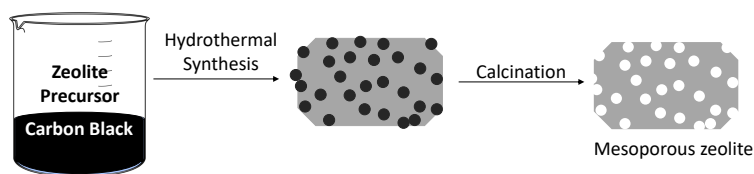


Figure 2.6: Mesoporous zeolite using carbon black as template.

“Recrystallisation” is another post-synthetic approach which is carried using a dissolution followed by reassembly typically carried out in the presence of a surfactant such as cetyltrimethylammonium bromide (CTAB). The process involves the reassembling of dissolved species of zeolite formed during desilication. The surfactant plays a major role in the protection of zeolite from non-uniform leaching [23, 76, 77].

2.2.4 Synthesis of zeolites

This section describes the synthesis methodology for various types of zeolites used as part of this Ph.D. work. Generally, zeolite synthesis involves the crystallisation of zeolite precursor gel under hydrothermal static conditions. The synthesis gel of zeolite consists of silica precursor, metal precursor, mineralizing agent and structure-directing agent. The silica precursor commonly used is tetraethyl orthosilicate (TEOS), tetramethyl orthosilicate (TMOS) or silicic acid, whereas NaAlO_2 and aluminium isopropoxide is used as Al precursor. The mineralising agent (e.g. hydroxide and fluoride) is used to provide a neutral pH in the synthesis media of zeolite. Although the role of the structure directing agent (SDUs) is not fully revealed yet, its application is highly significant in the zeolite synthesis. The commonly used SDA is quaternary alkylammonium ions although Na^+ and K^+ can be also used as SDA. After the hydrothermal synthesis in an autoclave, the products are collected and washed to remove the remaining reagents of synthesis and followed by calcined typically at 550 °C.

2.2.4.1 Materials

Material used for the reaction includes tetrapropylammonium hydroxide (TPAOH, 1M aqueous solution, Sigma Aldrich), tetraethylorthosilicate (TEOS, Sigma Aldrich), carbon black (Black Pearls 2000, Carbot Corporation), sodium aluminate (NaAlO_2 , 54 wt% AlO_2 and 41 wt% Na_2O , Riedel-de Haen), ammonium nitrate (NH_4NO_3 , 98%, Aldrich), ammonium hydroxide (NH_4OH , 28%), cetyltrimethylammonium bromide (CTAB, Sigma Aldrich), Pluronic F-127 (F-127, $M_w \sim 12600$ g/mol, Sigma Aldrich) and deionized water. All above chemicals were reagents grade and used without further purification.

2.2.4.2 Synthesis of HZSM-5

Conventional HZSM-5 synthesis includes two consecutive steps starting from the synthesis of NaZSM-5 followed by ion exchange to get HZSM-5. NaZSM-5 zeolite was first synthesized using the hydrothermal synthesis procedure at 170 °C. In a 100 ml Teflon beaker, 8.6 ml of TPAOH was stirred with 6.9 ml of water and 0.015 g of NaAlO_2 to get a clear solution. To this clear solution, 4.46 ml of TEOS was added dropwise and stirred at room temperature for 1 h. The reaction mixture was then transferred to a Teflon-lined stainless-steel autoclave and crystallisation was

conducted in a conventional oven at 170 °C for 72 h under static condition. The crystallised product was washed with water and ethanol several times. Resulting solid product was separated by centrifugation and dried under 80 °C overnight and then calcined at 550 °C for 12 h. Synthesis of silicalite-1 zeolite follows the same procedure with the only exception that NaAlO_2 is not added during the synthesis process.

The as-synthesised NaZSM-5 was then subjected to ion exchange steps to get acidic zeolite HZSM-5. 1 g of NaZSM-5 was added to 1.0M aqueous NH_4NO_3 solution (80 ml) and stirred for 2 h at 80°C. The resulting solid materials collected after centrifugation was subjected to ion-exchange two times again before it was dried at 80 °C overnight and heated in air at 550 °C for 5 h to produce HZSM-5 with Si/Al ratio of 120.

2.2.4.3 Synthesis of MesoHZSM-5

Carbon template was used to make MesoHZSM-5. In a Teflon beaker, 2 g of pre-dried carbon black is taken and impregnated with clear solution 8.6 ml of TPAOH and 0.015 g of NaAlO_2 . The material was dried at room temperature overnight and then impregnated with TEOS (4.46 ml) and allowed to dry at room temperature overnight again. The Teflon beaker was placed in a Teflon-lined stainless-steel autoclave (130 ml) containing distilled water (15 ml) and heated to 180 °C for 72 h. The product was collected and then washed using distilled water. The material was dried at 80 °C overnight and then calcined at 550 °C for 20 h to get a fine white powder. The obtained mesoporous zeolite was ion-exchanged, following the same procedure mentioned above for synthesis of HZSM-5 with Si/Al ratio of 120.

2.2.4.4 Synthesis of DesHZSM-5

Synthesis of mesoporous zeolites through desilication is as follows. NaZSM-5 was prepared using the method described in Section 2.2.4.2. 1.4 g of CTAB was dissolved in 100 ml NH_4OH (15% aqueous NH_3). 2 g of the zeolite was then added to the above solution and stirred at room temperature for 3 h. The resulting mixture was transferred to a Teflon-lined stainless autoclave (300 ml) and heated at 90 °C under the hydrothermal static condition for 24 h. The product was centrifuged and washed with deionized water for several times. The solid product was dried at 80 °C overnight and calcined at 550 °C for 10 h. The obtained mesoporous zeolite was ion-exchanged,

following the same procedure mentioned for synthesis of HZSM-5 with Si/Al ratio of 120.

2.2.4.5 Synthesis of F127-HZSM-5

The mesoporosity in F127-HZSM-5 is done through bottom-up approach using secondary soft template F127 block copolymer. The synthesis procedure is as follows. F-127 (3.2 g) was dissolved in 40 ml deionized water by stirring at room temperature. To the solution, NaAlO_2 (0.022 g) was added followed by TEOS (8.3 g). The solution mixture was stirred for 3 h. To the resulting mixture, TPAOH (2.6 g, 25%) was added dropwise and the mixture was stirred at 40 °C overnight. The obtained gel mixture was continued to stir at 60 °C for 6 h followed by drying at 90 °C in an oven overnight. The solid materials was transferred to a Teflon-lined stainless-steel autoclave containing 20 ml deionized water. The autoclave was heated to 160 °C and kept at static condition for 18 h. Following this, material was collected and washed several times with deionized water by centrifugation and dried at 80 °C overnight. The solid white product was calcined at 600 °C for 10 h to form F127-NaHZSM-5. The obtained mesoporous zeolite was ion-exchanged, following the same procedure mentioned for synthesis of HZSM-5 with Si/Al ratio of 150.

In this work, zeolite were used as the porous support for the encapsulation of

- Pd and Au nanoparticles in formic acid decomposition described in Chapter 4.
- Zn in the conversion of ethanol to butadiene described in Chapter 6.
- Pd nanoparticle in one-step synthesis of MIBK from acetone described in Chapter 7.

2.3 Mesoporous carbon

2.3.1 Ordered mesoporous carbon

Ordered mesoporous carbon is widely used for many electrochemical applications due to their inherent chemical inertness, low background current, good thermal and mechanical stabilities etc. Besides, the highly ordered mesoporous structures with tunable porosity, high pore volume and narrow pore size distribution make ordered mesoporous carbon suitable support materials for the application in catalysis. They

are characterised by long-range order of mesoporous channels which results in fast mass transfer for substrates and products [78–80].

Ordered mesoporous carbon can be synthesized using hard templates such as silica, MCM-48, polymer beads and colloidal silica nanoparticles or by soft templates such as surfactant F-127 and P-123. The extent of mesoporosity can be tuned by adjusting the amount of template [81]. In hard templating approach, an ordered mesoporous solid act as a mould for the negative replication followed by the post-synthetic removal of the template from the mesoporous carbon. The pore size is controlled by the template. See Figure 2.7(a). Although the silica-based template-assisted method results in highly ordered architectures of mesoporous system, the removal of silica by acid (HF) or base (OH^-) treatment is a significant disadvantage of this method [82].

The soft-template method occurs via self-assembly of surfactants and organic carbon precursors. The surfactant is later removed by carbonisation as shown in Figure 2.7(b). The pore structure and extent of mesoporosity is determined by the carbon precursor-surfactant interaction and the amount and nature of surfactant. Mesoporous carbon with a pore size of 3–7 nm can be synthesized by the soft-template method. This mesoporous carbon can be used to confine metal nanoparticles in the mesopores and can act as a suitable support material for the application in heterogeneous catalysis. However, in some cases, the chemically inert behaviour can limit its application for catalysis due to the weak interaction between metal nanoparticles and mesoporous carbon support. This can lead to aggregation of nanoparticles thereby resulting in deactivation [83]. The interaction between metal

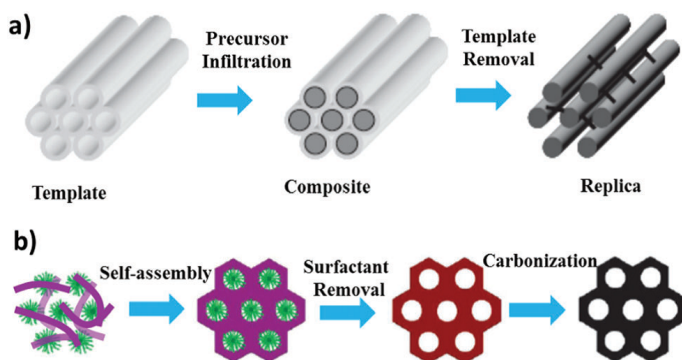


Figure 2.7: Synthesis of ordered mesoporous carbon using a) hard templating and b) soft templating [80].

nanoparticles and mesoporous carbon support can be improved to achieve good catalytic application through secondary functional groups such as nitrogen-doping.

2.3.2 Nitrogen-doped ordered mesoporous carbon

Studies have shown that doping nitrogen on ordered mesoporous carbon can enhance the performance of porous support in electrochemical application, metal-free catalysis and catalytic reaction. In the application for nanoparticles support, the nitrogen can act as an anchor for stabilizing the nanoparticle. Upon N-doping, the adsorption properties of mesoporous doping can be significantly improved into its structure. This is possibly due to the extra lone-pair of an electron from nitrogen which can activate p-electron in the carbon materials. This induces more hydrophilic properties on the surface and electron-donor properties of the carbon matrix in nitrogen-doped ordered mesoporous carbon [84–86].

Typically, there are two methods for the synthesis of nitrogen-doped ordered mesoporous carbon [87].

1. Heat treatment of ordered mesoporous carbon under a nitrogen atmosphere.
2. Direct synthesis from a precursor solution containing a mixture of nitrogen and carbon precursors.

The loading of nitrogen in the mesoporous carbon can be tuned by choosing different N-containing precursors.

In this Ph.D. work, both ordered mesoporous carbon and nitrogen-doped ordered mesoporous carbon are synthesized via soft template method. Selective dehydrogenation of ethanol to acetaldehyde described in Chapter 5 utilised both ordered mesoporous carbon and nitrogen-doped ordered mesoporous carbon as the porous support for the immobilisation of Cu nanoparticles.

2.4 Summary

In summary, porous support plays a significant role in the application of nanoparticles in heterogeneous catalysis. The porous support offers a unique interconnected system of pores and provides selectivity and stability even under harsh conditions. In this

work, both zeolites and ordered mesoporous carbon were used as support materials. Zeolites were used as catalyst support for the formic acid decomposition to hydrogen, conversion of ethanol to butadiene and synthesis of MIBK from acetone whereas ordered mesoporous carbon was used as porous support for dehydrogenation of ethanol to acetaldehyde.

CHAPTER 3

Characterisation Techniques

Characterisation techniques are used to investigate the structure, composition, physical and chemical properties of the porous support and nanomaterials in heterogeneous catalysis. This chapter introduces major techniques used for the characterisation of synthesised catalysts. The chapter gives a brief overview to X-ray powder diffraction, nitrogen physisorption, electron microscopy, temperature-programmed desorption, elemental analysis, X-ray photoelectron spectroscopy, in-situ diffuse reflectance infrared Fourier transform spectroscopy and thermo-gravimetric analysis which were used to analyse different aspects of catalysts.

3.1 Introduction

Characterisation techniques can provide valuable information about the structural and physicochemical properties of catalysts to better understand the relationship between catalyst properties and catalytic performance. This knowledge is vital to develop an optimum and efficient catalyst, which is more active, selective, and stable. The following sections in this chapter discuss various characterisation methods and equipment used as part of this thesis work.

3.2 X-ray powder diffraction

X-ray powder diffraction (XRD) technique is used to characterise the crystal structure of catalysts. The technique is based on the interaction of the X-ray with a powdered sample and uses Bragg's law to determine the resulting diffraction pattern.

$$n\lambda = 2d\sin\theta \quad (3.1)$$

where

n is a positive integer known as order of reflection

λ is the incident X-ray wavelength

d is the separation distance in crystal lattice

θ is the Bragg's angle

XRD patterns are generally presented as a function of 2θ with the interval ranging from 5 to 100°. The peak position, intensities and width are characteristics of the crystalline materials in the powdered sample with width of major peaks providing the information of the crystal size and quality of the sample. Scherrer equation is used to determine the average size of the crystallite material from diffraction pattern [88].

$$\tau = \frac{K\lambda}{\beta \cos\theta} \quad (3.2)$$

where

τ is the mean size of the crystalline domains

K is the shape factor

λ is the incident X-ray wavelength

β is the full width at half maximum of the intense peak

θ is the Bragg's angle

XRD for this work is carried out using Huber G670 diffractometer with Cu-K α radiation having a wavelength of $\lambda = 1.5406$ Å for confirming the crystallinity of porous supports and presence of nanoparticles in the samples.

3.3 Nitrogen physisorption

Nitrogen physisorption technique is used to determine the specific surface area, microporous and mesoporous volume and pore size distribution of the porous support and is calculated based on physical adsorption of nitrogen on the surface of sample. The adsorption measurements are generally plotted as adsorption-desorption isotherm which is a graphical representation of amount of gas adsorbed versus equilibrium relative pressure (p/p^0). The nature of adsorbent (microporous, mesoporous, macroporous, non-porous, etc.) and adsorbate determine the shape of the isotherm exhibited by the material [89]. The IUPAC classification grouped

adsorption isotherms into 6 types as shown in Figure 3.1. The classification is based on the behavior of isotherm at high relative pressure.

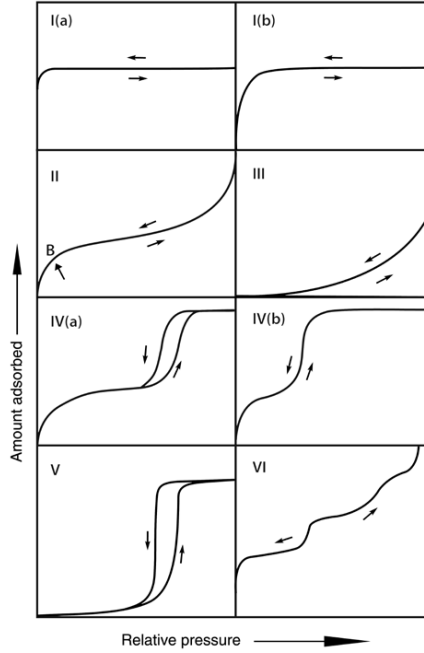


Figure 3.1: The IUPAC classification of physisorption isotherm. The figure was adapted from [90].

- Type I isotherm is the most common type exhibited by microporous materials such as zeolites characterized by relatively smaller external surface. Type I(a) are given by materials with narrow micropores of width less than < 1 nm whereas type I(b) are exhibited by materials with both narrow mesoporous and wide microporous width less than < 2.5 nm for nitrogen physisorption.
- Type II isotherm corresponds to non-porous or macroporous materials with no saturation for monolayer adsorption.
- Type III isotherm is a rare isotherm where the amount of adsorbate increases with no limit.
- Type IV isotherm represents a hysteresis loop often exhibited at relatively high p/p^0 . This type of isotherm is characteristics of mesoporous materials. Type IV(a) is accompanied with hysteresis loop due to capillary condensation whereas type IV(b) is observed for mesopores with smaller width.

- Type V is similar to type III and is attributed to the weak interaction between adsorbent and adsorbate gas molecules.
- Type VI isotherm is not common and represents stepwise adsorption leading to multilayer formation shown by non-porous materials. Example of type VI isotherm is the physisorption of argon on graphite or methane on magnesium oxide surface.

Hysteresis loops observed in type IV isotherm is further categorised into six types by IUPAC classification, as shown in Figure 3.2. Each hysteresis loop is associated with a specific mesoporous material [23, 89].

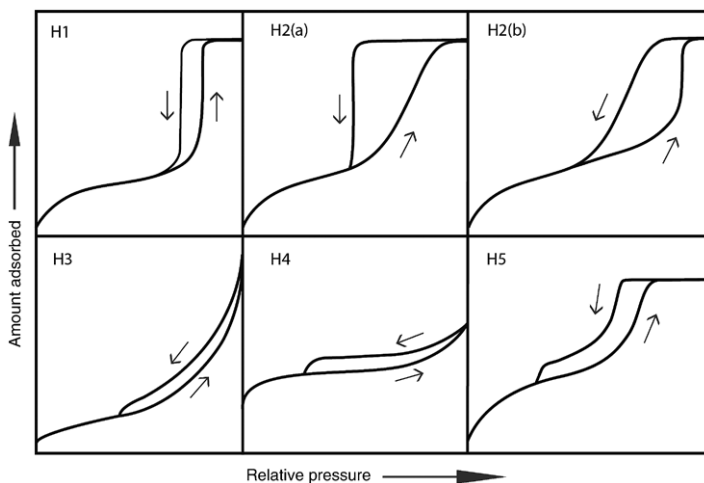


Figure 3.2: The IUPAC classification of hysteresis loops. The figure was adapted from [90].

- H1 loop for porous materials with narrow distributions of pore size.
- H2(a) loop for silica gels, porous glasses and ordered mesoporous materials.
- H2(b) loop for mesocellular silica foams.
- H3 loop for non-rigid aggregate of plate like particles.
- H4 loop for materials with narrow slit-pores.
- H5 loop for pore structure with open and partially blocked mesopores.

Several methods are used to determine the structural parameters from physisorption data [89].

- **Brunauer-Emmett-Teller (BET) equation:** This equation is popularly used to determine the surface area of the adsorbent, which is an extension of the Langmuir adsorption model [89, 91]. The calculation using BET method follows two stages, i.e. the transformation of physisorption isotherm to BET plot to derive a value of BET monolayer adsorption capacity (n_m) followed by calculation of BET area by adopting an appropriate value of the molecular cross-sectional area, σ using the BET equation.

$$\frac{p/p^0}{n(1 - p/p^0)} = \frac{1}{n_m C} + \frac{C - 1}{n_m C} p/p^0 \quad (3.3)$$

where

p is the equilibrium pressure

p^0 is the saturated pressure

n is the specific amount adsorbed at the relative pressure p/p^0

n_m is the specific monolayer capacity

C is the BET constant linked to energy of monolayer adsorption

The BET surface area can be calculated using the following equation:

$$S_{BET} = \frac{n_m N \sigma}{m N_m} \quad (3.4)$$

where

S_{BET} is the BET surface area

n_m is the specific monolayer capacity

N is the Avogadro's number

σ is the cross section of molecule adsorbed

m is the mass of the adsorbent

N_m is the molar volume of adsorbate

- **t -plot:** This is a common method for calculating the microporous and mesoporous volumes and the specific surface area of the adsorbent. The method assumes complete filling of micropores of the adsorbent [92].

- **The Barrett-Joyner-Halenda (BJH) method:** BJH method is used for calculating the pore size distributions of the adsorbent from experimental isotherms. This method assumes the porous structures as cylindrical and non-connecting geometry [23]. This method is most applicable for large and medium-sized mesopores and is not accurate for small mesopores.

The nitrogen physisorption for this work is carried out using the instrument Micromeritics 3Flex at liquid nitrogen temperature. Prior to the analysis, the samples were outgassed at 400 °C (zeolite) and 200 °C (mesoporous carbon) overnight. The total pore volume is calculated from the amount of nitrogen adsorbed at a relative pressure of $p/p^0 = 0.95$.

3.4 Electron microscopy

Electron microscopy is an imaging technique used for structural characterisation of the materials. This technique is used to determine size and shape of crystals, porosity on the surface of the crystals, size, shape and distribution of nanoparticles. In electron microscopy, the interaction between the electron beam and the specimen is utilised for exploring the information of material used for the analysis. When the electron beam

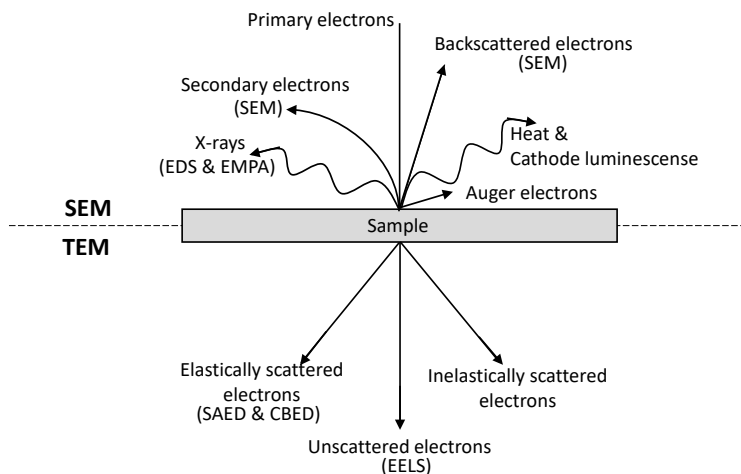


Figure 3.3: Schematic representation of electron beam interaction with specimen resulting different types of detectable signal.

with the characteristic wavelength of less than 1 Å hits the specimen, several sets of the detectable signal are generated as shown in Figure 3.3 [93]. Each type of electron beam provides different information on the characteristics of the specimen. As part of this work, scanning electron microscopy (SEM) and transmission electron microscopy (TEM) are used for the characterisation of catalysts and are briefly discussed in the following sections.

3.4.1 Scanning electron microscopy

Scanning electron microscopy (SEM) is used to investigate the morphology of samples and provides information about surface topography, for instance, crystal size and shape of materials. In SEM, electron beam emitted from an electron source (e.g. tungsten filament or field emission gun (FEG)) are accelerated to 1-30 keV and passed through a series of lenses and apertures to produce a focused beam of electrons that hits the surface of the specimen. This electron-specimen interaction results in the generation of several signals which are then detected by appropriate detectors [94].

Figure 3.4 is the representation of electron-specimen interaction and the regions with different electron signals which can be detected with SEM [95]. Both secondary electron beam and backscattered electron beam are useful for SEM analysis. The

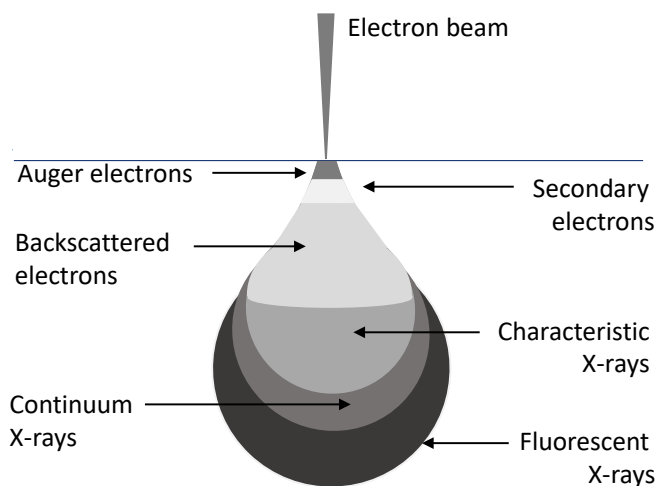


Figure 3.4: Schematic representation of interaction volume of the specimen and the regions with different electron signals for SEM.

secondary electrons are generated by inelastic scattering of electrons at the surface or near-surface region of the sample. The secondary electrons have less energy ($\approx 5 - 50$ eV) as compared to backscattered electrons. Therefore, the collected secondary electrons in SEM originate from an area slightly below the incident electron beam and give good resolution compared to the backscattered electron. Backscattered electrons are the elastically scattered electron and come from a deeper volume of the specimen. Backscattered electron is high energy electron and contains information regarding the composition of the sample [94]. Figure 3.5 shows SEM image taken for carbon nanotubes. The image provides a good indication of the size and shape of carbon nanotubes.

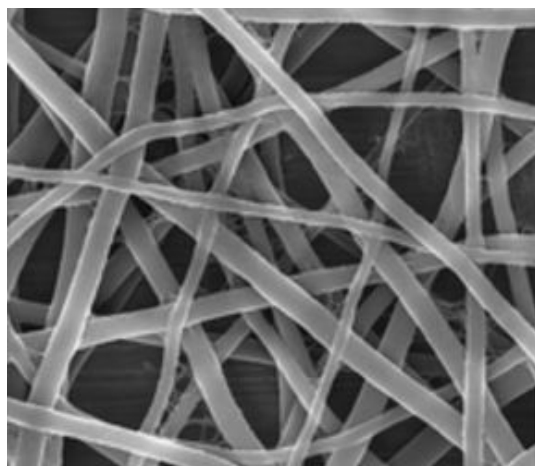


Figure 3.5: SEM image of carbon nanotubes [96].

SEM analysis for this work is carried out using Quanta 200 ESEM. The solid samples such as zeolite and carbon were dispersed on 9 mm carbon tape and gold sputtering was done at 20 mA for 45 s. The gold sputtering prevents charge accumulation of the materials and helps to detect more secondary electron beams from the specimen. This enhances the image resolution and decreases the damage caused by the electron beam [97].

3.4.2 Transmission electron microscopy

Transmission electron microscopy (TEM) is used to analyse morphologies of sample, size, shape and distribution of nanoparticles, etc. TEM is often an important

method to characterise heterogeneous catalysts. In TEM, a high energy electron beam is emitted from an electron gun which passes through a series of lenses and apertures (condenser lens, condenser aperture, objective lens and objective aperture) and is transmitted through a very thin specimen [98]. The beam is then passed through diffraction lens and projector lens which magnifies and project the image on a fluorescent screen and records the image in the charge-coupled device (CCD) camera. Figure 3.6 shows the schematic representation of transmission electron microscopy.

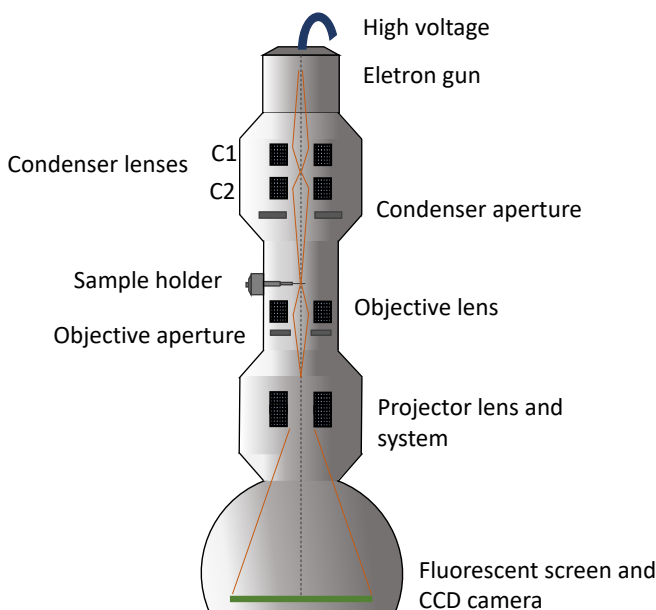


Figure 3.6: Schematic representation of transmission electron microscope.

Normally, TEM images are collected using bright field imaging. In bright field imaging, the elastically transmitted/unscattered electron beams are collected with the objective aperture whereas the scattered electron beams are blocked. This results in the area with crystalline and large mass materials appearing dark and transmitted region looking bright. For instance, the heavier elements will appear as a dark region in the TEM image [99]. On the contrary, in dark-field imaging, the scattered electrons are selected and the unscattered electron beams are avoided, thereby displaying the empty area as a dark region in the TEM image [99, 100]. An example of TEM image for Pd supported on carbon nitride is shown in Figure 3.7.

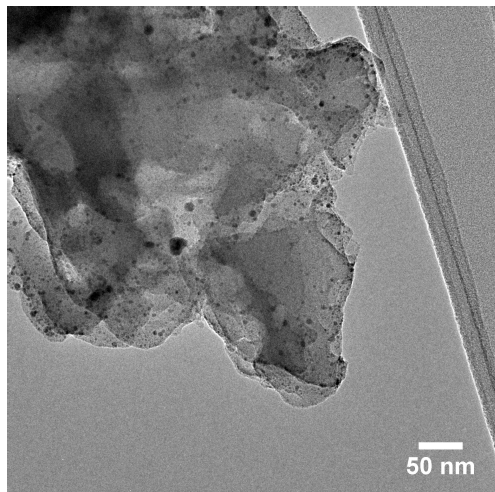


Figure 3.7: TEM image of Pd supported on carbon nitride

TEM image for this work is collected using FEI Tecnai T20 G2 microscope operated at 200 kV. The samples were dispersed on Lacey copper grid. High-angle annular dark-field scanning transmission electron microscopy (HAADF-STEM) analysis is performed on an aberration-corrected JEOL ARM300CF instrument operated at 300 kV. The samples were dispersed on gold grid.

3.5 Ammonia temperature-programmed desorption

Ammonia temperature-programmed desorption (NH_3 -TPD) is used for measuring the acidity of the catalysts [101, 102]. This technique consists of the following steps:

1. Outgassing the material at 500 °C under the flow of an inert gas, such as Ar and He followed by cooling down to 100 °C.
2. Pre-adsorption of NH_3 for 1 h.
3. Evacuation after pre-adsorption to remove the physically adsorbed gas for 3 h.
4. Programmed desorption of the residual chemisorbed gas into the stream of carrier gas with heating the sample from 100 to 500 °C.
5. Measurement of desorbed gas in the carrier using a TCD (Thermal conductivity detector) for analysing the acidic property of materials.

The acidic properties of H-form zeolites like HZSM-5, faujasite, etc. are generally measured using NH_3 -TPD technique. Typically, the TPD of HZSM-5 shows two peaks l(low) and h(high) with peak maximum around 150 and 400 °C, respectively [103].

This work utilises Micrometrics Autochem-II 2920 device for performing NH_3 -TPD with approximately 100 mg of the sample.

3.6 Hydrogen temperature programmed reduction

Hydrogen-temperature programmed reduction (H_2 -TPR) is used to examine the surface chemistry of catalysts by capturing the data relating to the reducibility of materials.

In this Ph.D., the reduction temperature of the catalysts are analyzed by H_2 -TPR using a Micromeritics Autochem-II instrument. Samples were heated up to 500 °C at a ramp of 10 °C per minute in 5% H_2 in Ar gas flow (50 mL/min). The H_2 consumption was monitored using a thermal conductivity detector (TCD). A cold trap with dry ice was used to trap the water formed during the reduction with H_2 .

3.7 Elemental analysis

Elemental analysis is used to record the elemental distribution of the test specimen. This work utilises four different elemental analysis methods depending on the application including Energy dispersive X-ray spectroscopy, inductively coupled plasma-optical emission spectroscopy, X-ray photoelectron spectroscopy and CHN analysis.

3.7.1 Energy dispersive X-ray spectroscopy

Energy dispersive X-ray spectroscopy (EDS) is a technique used to determine the elemental distribution in the catalysts. EDS is used to map the elements using an electron beam by focussing a sample in either SEM or TEM and therefore is combined with the respective electron microscopy.

For this work, EDS is combined with TEM. The analysis is carried out using Oxford Instruments XMAX 100 EDX detector.

3.7.2 Inductively coupled plasma-optical emission spectroscopy

Inductively coupled plasma-optical emission spectroscopy (ICP-OES) is an elemental analysis technique used for the identification and quantification of the elements present in the sample. When a sample is treated with plasma radiation, the elements absorb some amount of energy and are excited to a higher energy level. The excited (high energy) element releases a certain amount of energy and return to its ground state to stay in low energy position. The photon wavelength of emitted radiations is determined to analyse the element present in the sample. The position and the intensity of the photon rays provide the information on the identity and quantity of the elements, respectively [104, 105].

In this work, the metal loadings of catalysts were determined using ICP-OES. The measurements were carried out in Thermo ScientificTM iCAPTM 7200 ICP-OES. The sample (20 mg) is dissolved in aqua regia (20 ml) by heating at 80 °C followed by filtering the mixture using sintered glass crucible (porosity grade G4) assisted by a vacuum pump. The clear filtrate was diluted with milli-Q water to get 2% HNO₃ solution.

3.7.3 X-ray photoelectron spectroscopy

X-ray photoelectron spectroscopy (XPS) is surface sensitive technique which can be used to determine the surface elemental composition, empirical formula, electronic state, etc.

In this work, XPS is performed using ThermoScientific device with Al-K α radiation under ultra-high vacuum. Analysis of the XPS data is done via *Avantage* software to identify the binding energy of various elements.

3.7.4 CHN analysis

CHN analysis is to determine the percentage of carbon, hydrogen and nitrogen concentrations in the bulk of samples with precision and accuracy. The technique calculates the composition of C, H and N based on Dumas method [106].

For this work, CHN is measured using Thermo Scientific FlashSmartTM CHNS/O Elemental Analyzer. Around 2-3 mg of the material is injected into a high-temperature furnace (~ 1000 °C). The sample is combusted in the presence of pure oxygen and followed by conveying the gas mixture by helium gas flow that

sweeps through a GC-column. The gas is analysed by GC and detected by Thermal conductivity detector (TCD). The procedure is repeated for three times and correlated with the calibration made with a standard [107].

3.8 In-situ diffuse reflectance infrared Fourier transform spectroscopy

In-situ diffuse reflectance infrared Fourier transform spectroscopy (in-situ DRIFTS) study is used to determine the surface characterisation of non-transparent or solid samples, where the temperature and environment of the samples can be controlled in-situ in the DRIFTS cell. Additionally, this technique is used to study the mechanism of gaseous phase reaction by analysing the intermediates formed. In a typical experiment, the infrared radiation incident on the sample results in different types of the process such as scattering, reflecting, absorbing or penetrating before reflecting out of the sample. The randomly oriented diffuse-reflected light is collected using two plane mirrors or paraboloid or ellipsoid mirrors and then detected by an IR detector for characterisation of chemical and structural properties of the solid sample [108].

DRIFTS for this work is carried out using Thermo Nicolet 6700 FTIR using a reactor and Praying Mantis diffuse reflectance accessory from Harrick Scientific Products.

3.9 Thermo-gravimetric analysis

Thermo-gravimetric Analysis (TGA) is a thermal analysis technique used to test the stability of samples under the effect of temperature.

In this work, TGA is performed using Mettler Toledo instrument for a temperature range from 20 to 600 °C with ramp of 10 °C under N₂ (50 ml/min) flow.

3.10 Summary

To summarise, various analytical methods are used to characterise and investigate heterogeneous catalysis. These methods can provide valuable information about the

structural and physicochemical properties of catalysts to develop an highly active, selective, and stable catalysts for any reaction.

CHAPTER 4

Decomposition of Formic acid

Hydrogen can play a vital role in resolving the issue of renewable energy storage. This chapter describes a novel heterogeneous catalytic system for the continuous production of hydrogen through the decomposition of formic acid. The bimetallic catalyst consists of Pd - Au metal nanoparticles encapsulated in zeolite silicalite-1. The chapter addresses synthesis methodology, characterisation, catalytic test results and identifies the optimum catalyst for the decomposition of formic acid.

4.1 Introduction

The production of energy from renewable sources such as solar and wind is steadily increasing over the past years. Due to the intermittent nature of the renewable sources, the demand for an efficient energy storage solution storage has become more acute [19, 109, 110]. Hydrogen as an energy storage option is very promising due to its high energy density, increased efficiency and cleanliness as compared to conventional non-renewable resources [111, 112]. Hydrogen is used as the source for various fuel cells such as proton exchange membrane fuel cells (PEMFCs), alkaline fuel cells (AFCs), solid oxide fuel cells (SOFCs) etc. due to the energy capacity of H—H bond (approx. 120 kJ g⁻¹). The only by-product formed via fuel cell is water [24, 37, 113–116].

Hydrogen is mainly produced through steam reforming of natural gas, which accounts for > 90% of total hydrogen production [117]. Alternatively, hydrogen is also produced via electrolysis of water by splitting water into hydrogen and oxygen using the surplus of renewable energy [21, 111, 118].

Hydrogen can be stored and transported in both gaseous and liquid phase. However, storage and transport of hydrogen in the gaseous state in high pressurised containers limit its practical application due to concern over safety [110, 119, 120]. An alternative way to store hydrogen is via adsorption method on/within the surface of

porous adsorbent material like zeolites, metal-organic frameworks (MOFs), porous organic polymers (POP), metal hydrides etc [60, 110, 121–123]. However, lack of reversibility, need for high temperature and lack of storage capacity at room temperature limits these methods of storage [17, 124].

Hydrogen can be also stored in chemical compounds i.e. a chemical hydrogen storage system like amines, metal ammine complexes, alcohols, formic acid, etc [125, 126]. Recently, formic acid has got great attention towards hydrogen storage system due to its possibility to be produced via biomass conversion [15, 18, 127]. For instance, it is an important by-product formed during the biomass conversion process. Formic acid is a non-toxic and liquid compound at room temperature with high hydrogen density (4.4 wt%). The decomposition of formic acid is a promising route for hydrogen as formic acid can be transferred as liquid form, which requires no additional energy compared to the high-pressure system [15, 128]. Figure 4.1 illustrates the possible formic acid cycle using CO_2 for the hydrogen storage system [129]. In this method, formic acid undergoes decomposition to release H_2 and CO_2 . In the hydrogen storage phase, CO_2 and H_2 are combined to form formic acid. Therefore, CO_2 act as the hydrogen carrier that can be captured or released accordingly.

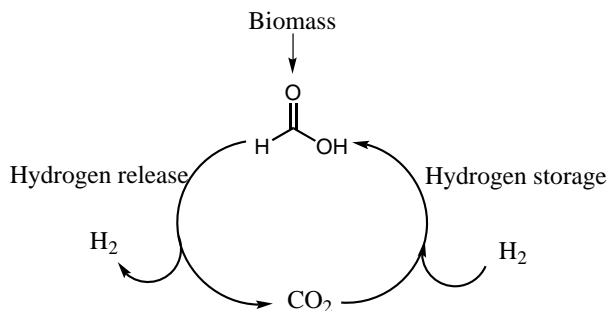


Figure 4.1: A possible cycle for the production, storage and release of H_2 via formic decomposition.

Formic acid decomposition may undergo two pathways (dehydrogenation to form CO_2 and H_2 or dehydration to form CO and H_2O) as shown in Figure 4.2 [127]. The nature of both reactions is different with dehydration being slightly exothermic and dehydrogenation being slightly endothermic [130]. As CO can cause electrode poisoning in the fuel cell, the design of a suitable catalyst to selectively choose the dehydrogenation pathway is quite significant in formic acid decomposition [131].

Although the mechanism of formic acid decomposition using heterogeneous

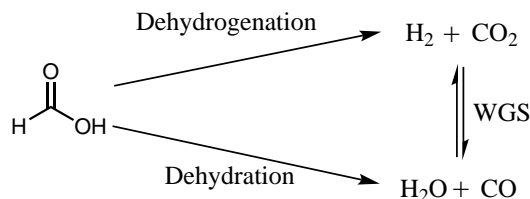


Figure 4.2: Pathways for formic acid decomposition.

catalysis is not fully understood, the nature of active surface can affect the type of intermediate species formed. Presence of several metal atoms closely can lead to the formation of bidentate formate species whereas isolated and small active metal can lead to the formation of monodentate formate species as shown in Figure 4.3. Although both bidentate and monodentate formate can lead to the production of CO_2 , CO is most likely produced when monodentate formate species are formed as intermediate [132].

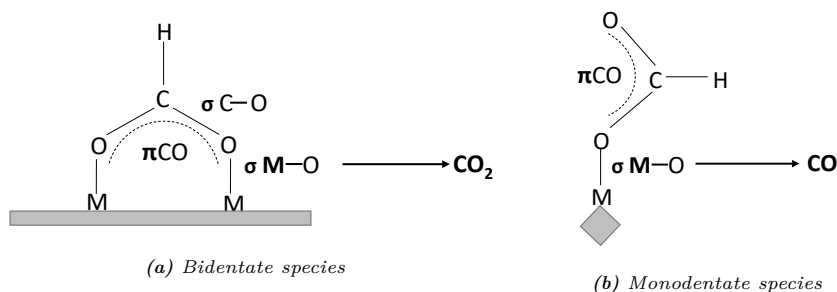


Figure 4.3: Dependency of surface structure of metal nanoparticles in formic acid decomposition [133].

Both homogeneous and heterogeneous catalysts have previously been used for the formic acid decomposition [132, 134]. Formic acid decomposition via homogeneous catalytic systems with iridium-based and iron pincer complexes has been reported in the literature with high TOF of 22800 h^{-1} and TON of close to 1000000, respectively. The heterogeneous catalytic system with Pd supported on carbon, Pd on resin, Pd or Au nanoparticles on metal oxide support etc. were reported for the formic acid decomposition [128, 135–143]. However, the continuous production of hydrogen via a fixed flow reactor with high TOF, good selectivity and reusability is a challenge for its commercial application. Recently, Wang et al. reported heterogeneous catalyst

comprised of Pd encapsulated in silicalite-1 for the formic acid decomposition. They proposed in-situ encapsulation method to synthesis ultra-small Pd nanoparticles for a highly stable catalyst [144]. Studies have shown that supported bimetallic nanoparticles such as Ag-Pd, Au-Pd, Pt-Pd etc, often perform better than the mono-metallic nanoparticle [132, 145–150].

As part of this thesis work, Pd-Au metal nanoparticles encapsulated in the zeolite silicalite-1 (Si1) were tested for formic acid decomposition. The catalysts were synthesised using in-situ encapsulation method as proposed by Wang [144]. Different ratios of Pd and Au were studied to find the optimum catalyst. To distinguish Pd and Au loading of synthesised catalysts, the terminology xPd-yAu@Si1 was used where x represents the relative mass of Pd over Au and y represents the relative mass of Au over Pd. Table 4.1 shows the various bimetallic catalysts synthesised with the approx. Pd/Au ratio. To compare the performance, single metallic catalytic systems such as Pd@Si1, Au@Si1 and Au/Si1 were also synthesised and analysed.

Table 4.1: *Synthesised catalysts for decomposition of formic acid.*

Catalysts	Pd:Au mass ratio approx.
2Pd-1Au@Si1	2:1
1Pd-1Au@Si1	1:1
1Pd-2Au@Si1	2:1
Pd@Si1 and Pd/Si1	1:0
Au@Si1 and Au/Si1	0:1

4.2 Experimental Section

4.2.1 Materials

Chemicals used for the reaction includes tetraethylorthosilicate (TEOS, Sigma Aldrich), tetrapropylammonium hydroxide (TPAOH, 1.0 M aqueous solution, Sigma Aldrich), palladium chloride (PdCl_2 , 99%, Sigma Aldrich), ethylenediamine ($\text{NH}_2\text{CH}_2\text{CH}_2\text{NH}_2$, 99%, Sigma Aldrich) and gold chloride (AuCl_3 , 98%, Sigma Aldrich). All the above chemicals were reagents grade and used without further purification.

4.2.2 Synthesis of materials

Pd nanoparticles were encapsulated in silicalite-1 zeolite using both incipient wetness impregnation and in-situ encapsulation. Additionally, Au nanoparticles were encapsulated in silicalite-1 zeolite using pressure-assisted impregnation and in-situ encapsulation. Moreover, bi-metallic catalysts comprised of both Pd and Au in three different Pd/Au metal loading ratios encapsulated in silicalite-1 zeolite using in-situ method were also synthesised.

Silicalite-1 (Si1) zeolite was synthesised following the same method as described in Section 2.2.4.2 with the only exception that NaAlO_2 is not added.

4.2.2.1 Synthesis of Pd/Si1

Si1 (0.99 g) was vacuum dried at 50 °C overnight. An aqueous solution of PdCl_2 (0.012 g) was prepared with deionized water for incipient wetness impregnation. The Pd precursor was then added to the pre-dried silicalite-1 dropwise and the solid mixture was hand-mixed thoroughly in a mortar after each drop. The resulting Pd precursor-silicalite mixture was dried at room temperature for overnight. The mixture was reduced at 300 °C in H_2 (10% H_2/N_2) flow (50 ml/min) for 2 h with a heating ramp 5 °C/min to obtain Pd/Si1 with 0.6 wt% Pd.

4.2.2.2 Synthesis of Au/Si1-PAIR

Si1 (0.99 g) was vacuum dried at 50 °C overnight. An aqueous solution AuCl_3 (0.012 g) was prepared with deionized water for incipient wetness impregnation to prepare 0.6 wt% of Au/Si1-PAIR. The gold precursor was impregnated with silicalite-1 and placed in a stainless-steel autoclave. The sample was subjected to pressure-assisted impregnation under 3 bar N_2 for 2 h. The resulting material was subjected to 5 bar H_2 and reduced at 150 °C with a total pressure of 8 bar to produce Au/Si1-PAIR with 0.64 wt% Au.

4.2.2.3 Synthesis of Pd@Si1 and Au@Si1

Synthesis of Pd@Si1 was carried out based on the method reported in the literature [144] whereas Au@Si1 was synthesised with a modification of the same method. First of all, PdCl_2 (0.027 g) and ethylenediamine (0.3 ml) was mixed in 2.5 ml water to get a clear solution of ethylenediamine complex of palladium. Similarly, ethylenediamine

complex of gold was synthesized by mixing AuCl_3 (0.042 g) and ethylenediamine (0.4 ml) in water to get a clear solution. In a 100 ml Teflon beaker, TPAOH (16.1 ml) and deionized water (6.9 ml) were stirred at room temperature for 5-10 min. TEOS (8.32 ml) was added dropwise to the resulting solution and stirred at room temperature for 6 h. To the above homogeneous mixture, a solution of either ethylenediamine complex of palladium in water or ethylenediamine complex of gold in water was added and stirred it for 30 min. The reaction mixture was transferred to a Teflon-lined stainless-steel autoclave to perform the crystallization in a conventional oven at 170 °C for 96 h under static condition. The crystallized product was centrifuged and washed with water several times. The resulting solid product was dried at 80 °C overnight and calcined at 550 °C for 12 h followed by the reduction under the flow of formier gas for 2 h at 350 °C with a heating ramp of 5 °C/min. Both catalysts contained 0.6 wt% metal loading.

4.2.2.4 Synthesis of 1Pd-1Au@Si1

In a 100 ml Teflon beaker, TPAOH (16.1 ml) and deionized water (6.9 ml) was stirred at room temperature for 5-10 min. TEOS (8.32 ml) was added dropwise to the resulting solution and stirred at room temperature for 6 h. To the above homogeneous mixture, a solution of ethylenediamine complex of palladium in water was added and stirred it for 10 min. Following this, a solution of ethylenediamine complex of gold in water was added and stirred at room temperature for another 30 min. The reaction mixture was transferred to a Teflon-lined stainless-steel autoclave to perform the crystallization in a conventional oven at 170 °C for 96 h under static condition. The crystallized product was centrifuged and washed with water several times. The resulting solid product was dried at 80 °C overnight and calcined at 550 °C for 12 h followed by the reduction under the flow of formier gas for 2 h at 350 °C with a heating ramp of 5 °C/min. The same procedure is repeated to synthesis 2Pd-1Au@Si1 and 1Pd-2Au@Si1 by altering the quantity of PdCl_2 and AuCl_3 .

4.2.3 Charecterisation

All synthesized samples were characterised using various techniques including XRD, nitrogen physisorption, TEM, HAADF-STEM, ICP-OES, XPS and H_2 -TPR. The equipment used and conditions applied for different analysis are specified in Chapter 3. Additionally, in-situ DRIFTS measurements were carried as follows. About 15 mg

of the sample was mixed thoroughly with 135 mg of KBr and placed in a Harrick Scientific Praying Mantis DRIFTS attachment with a high-temperature reaction chamber. The cell was heated to 100 °C in the flow of N₂ gas (100 ml/min). Once the steady flow has reached, formic acid (60 µl/h) was passed over the catalysts with a N₂ gas flow (100 ml/min). An MCT detector is used to detect the product. The spectra were recorded over 20 periods with each period consisting of 41 spectra of formic acid/N₂ flow and 41 spectra of pure N₂ flow. The shift between formic acid/N₂ and N₂ was performed by a VIGI switch valve from Valco Instruments.

4.2.4 Gas-phase dehydrogenation of formic acid

The catalytic activity test was performed at atmospheric pressure in a quartz fixed bed reactor (3 mm diameter). The quartz reactor was loaded with 30 mg of fractionated catalyst diluted with 270 mg quartz crystals (180-355 µm). N₂ (50 ml/min) was bubbled through the formic acid which was stirring at 40 °C to obtain a steady flow rate of 4.5 ml/min for the formic acid gas. The gaseous mixture was passed through the catalysts bed at atmospheric pressure. The product was analysed continuously by an online non-dispersive infrared detector to quantify the amount of CO and CO₂ formed during the reaction. All catalysts were tested under the same condition with a temperature range of 40 to 200 °C with a heating ramp of 3 °C/min.

4.3 Results and discussions

This section describes the results obtained through various characterisation techniques used for as-synthesised materials. This is followed by the test for performance of all the synthesised catalyst for the decomposition of formic acid.

4.3.1 Characterisation results

4.3.1.1 XRD

Figure 4.4 shows the XRD patterns of all investigated materials. For comparison, XRD of silicalite-1 zeolite was also shown in the Figure 4.4. All materials showed the characteristic diffraction pattern of MFI structured silicalite-1. Au@Si1 showed a peak at 38.1° corresponds to Au(111) plane. However, no peak were observed at $2\theta = 40.1^\circ$ and 46.4° (Pd) corresponding to lattice plane (111) and (200) and $2\theta = 38.1^\circ$

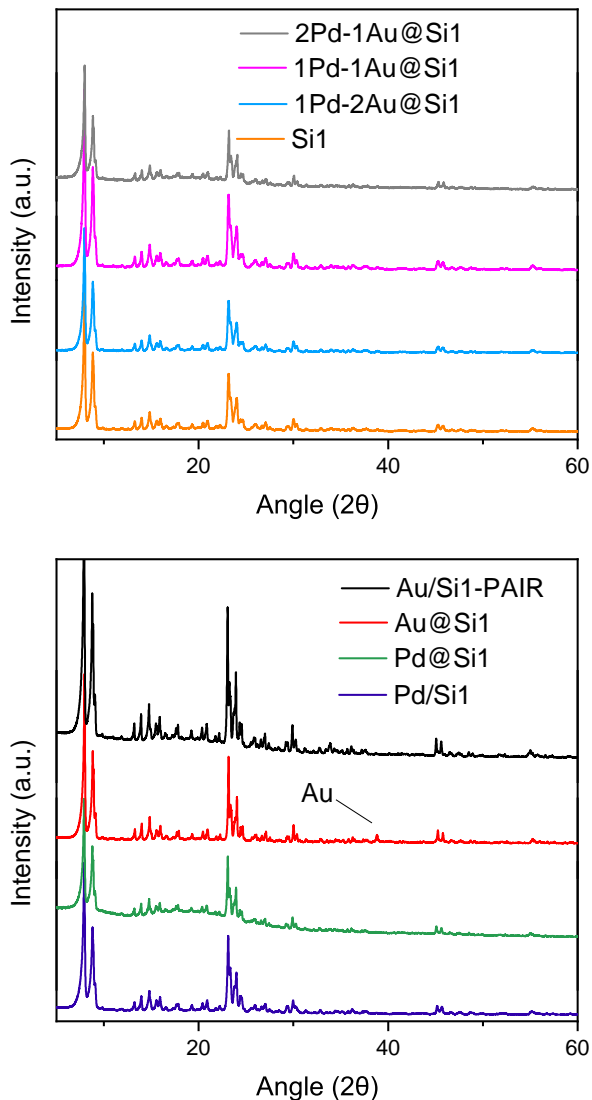


Figure 4.4: XRD of prepared materials.

and 44.3° (Au) corresponding to lattice plane (111) and (200) for other samples. This can be either due to the overlap of diffraction peak of Pd and Au nanoparticles with the diffraction peak of silicalite-1 or due to the small size of Pd and Au nanoparticles making it insufficient to result in a diffraction pattern [144].

4.3.1.2 Nitrogen physisorption

Figure 4.5 shows the isotherms and pore width of Pd@Si1, Au@Si1, 1Pd-1Au@Si1 and 2Pd-1Au@Si1. In general, the materials showed the isotherm of typical microporous materials. The isotherm of Au@Si1, 1Pd-1Au@Si1 and 2Pd-1Au@Si1 showed small hysteresis loop of p/p^0 in the range of 0.14 to 0.18. This is possibly due to the fluid-crystal phase transition, which is typical for nitrogen in MFI micropores [151]. Moreover, isotherm showed a hysteresis loop around $p/p^0 = 0.41$ which can be originated from the tensile strength effect (TSE) [98, 151].

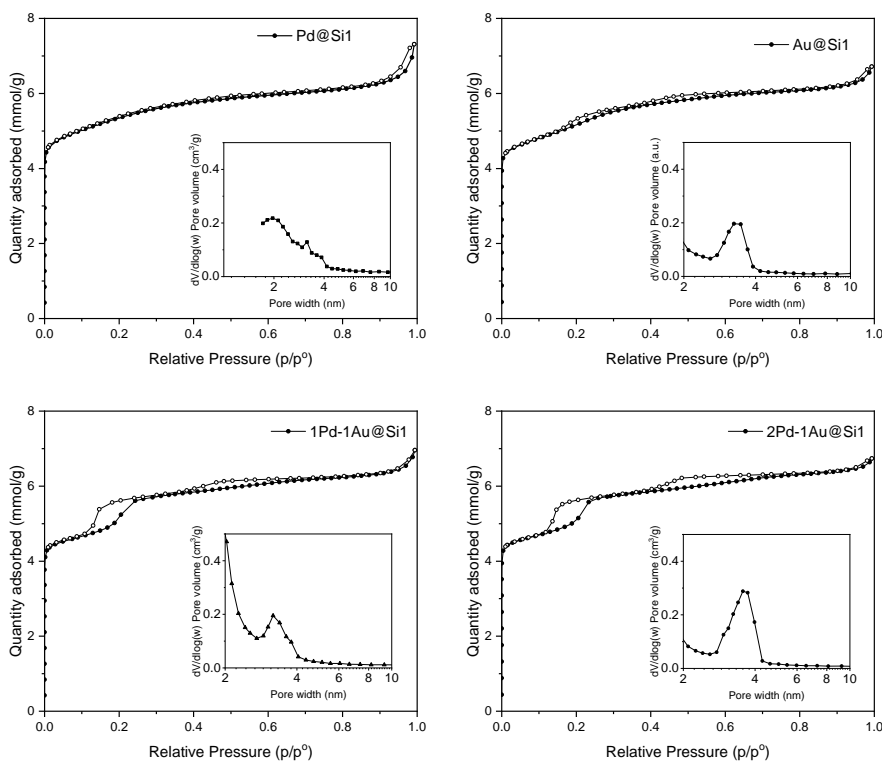


Figure 4.5: Physisorption isotherms and pore width distribution of synthesised materials.

4.3.1.3 TEM

In order to get the detailed information of size and distribution of nanoparticles, TEM was performed on the samples. Figure 4.6 shows the TEM images of Au/Si1-PAIR

and Pd/Si1. The average particle size from the TEM image showed that Au/Si1-PAIR crystals had smaller nanoparticles (4.2 ± 1.7 nm) compared to Pd/Si1 (5.4 ± 1.6 nm). Both TEM images showed the distribution of nanoparticles throughout the crystal of silicalite-1 support. Figure 4.7 shows the TEM images of Pd@Si1, Au@Si1, 1Pd-1Au@Si1 and 2Pd-1Au@Si1. Pd and Au nanoparticles were not visible in any of the TEM images. This could be due to the small nanoparticles formed in silicalite-1 crystals as the in-situ method used for the synthesis mostly results in the formation of ultra small nanoparticles [144]. To observe the nanoparticles of one of the in-situ synthesized materials, an ultra-high resolution STEM in High-Angle Annular Dark-Field (HAADF) image was collected for the sample 2Pd-1Au@Si1 using JOEL ARM300F. The STEM-HAADF image is given in the Figure 4.8(a), whereas Figure 4.8(b) shows the particles size distribution of Pd-Au nanoparticles. The STEM-HAADF image showed small and uniformly distributed nanoparticles where most the nanoparticles are situated inside the core of the silicalite-1 making it difficult to image the nanoparticles of Au and Pd in the samples and investigate whether the bimetallic system forms alloys, shell-around or discrete metal nanoparticles. Average particle size for different catalysts observed from TEM images are listed in Table 4.2.

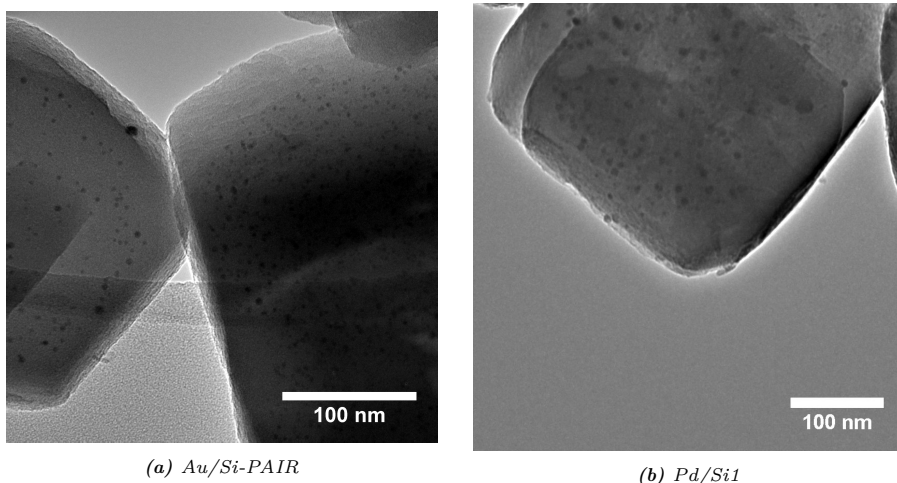


Figure 4.6: TEM images of Au/Si-PAIR and Pd/Si1.

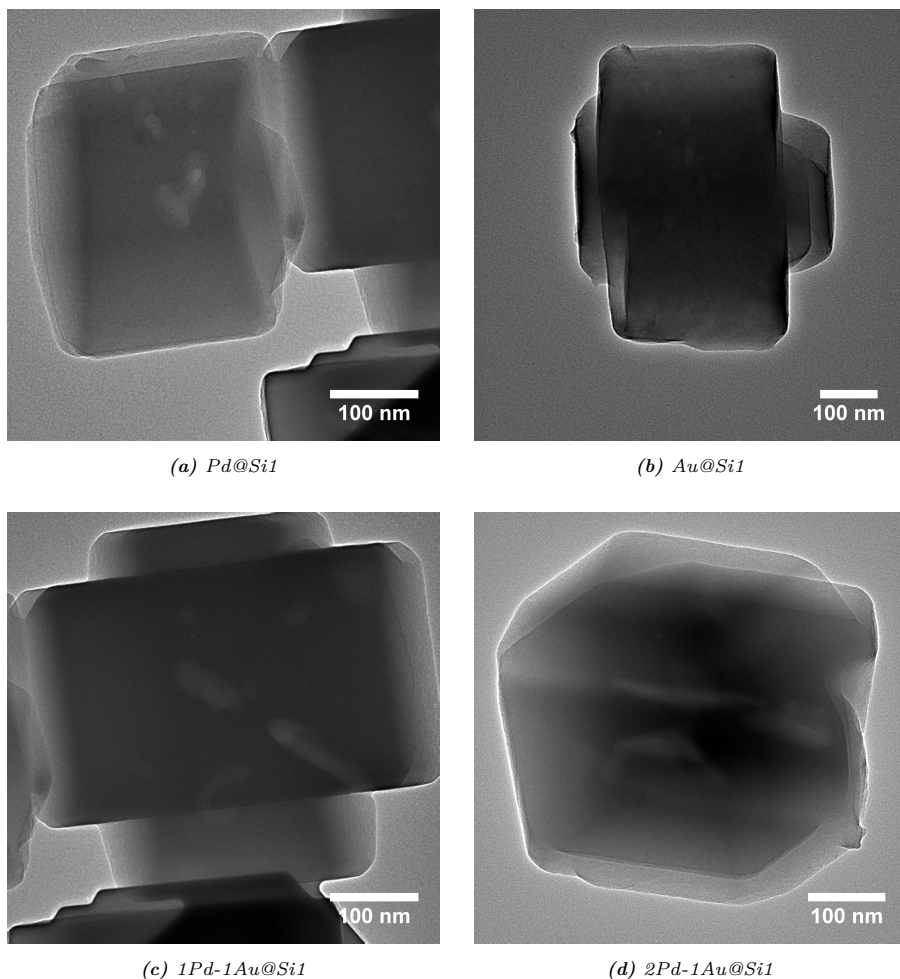


Figure 4.7: TEM images of prepared materials.

4.3.1.4 ICP-OES

ICP-OES is an elemental analysis technique used for the identification and quantification of the elements present in the sample. In this case, the metal loading of synthesised catalysts were measured using ICP-OES and results are given in Table 4.2. The results matches the amount of Pd and Au metal precursor used during the synthesis process and Pd/Au mass ratio for the bimetallic catalysts. For instance Pd:Au ratio for 1Pd-2Au@Si1 is 0.20:0.42 which is approx. 1:2.

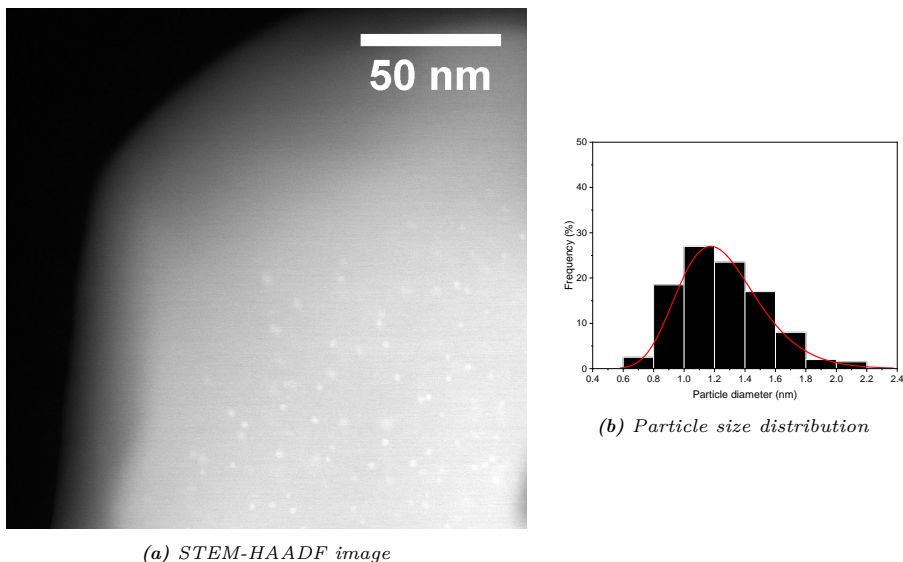


Figure 4.8: HAADF image and particle size distribution of 2Pd-1Au@Si1.

Table 4.2: Metal loading and particle size of synthesised materials.

Catalysts	Average particle size nm	Pd loading wt%	Au loading wt%
2Pd-1Au@Si1	1.1 ± 0.6	0.42	0.18
1Pd-1Au@Si1	Not detectable	0.33	0.32
1Pd-2Au@Si1	Not detectable	0.20	0.42
Pd@Si1	Not detectable	0.60	-
Pd/Si1	5.4 ± 1.6	0.60	-
Au@Si1	Not detectable	-	0.60
Au@Si1-PAIR	4.2 ± 1.7	-	0.64

4.3.1.5 XPS

Figure 4.9 shows XPS of investigated materials. The samples Au/Si1-PAIR and Pd/Si1 showed the presence of gold and palladium photopeak, respectively in the XPS spectra while no gold and palladium photopeaks were observed for all other investigated samples. Since the XPS is a surface analysis, the absence of gold and palladium photopeaks indicates that the metal nanoparticles were successfully encapsulated inside silicalite-1 crystals [152].

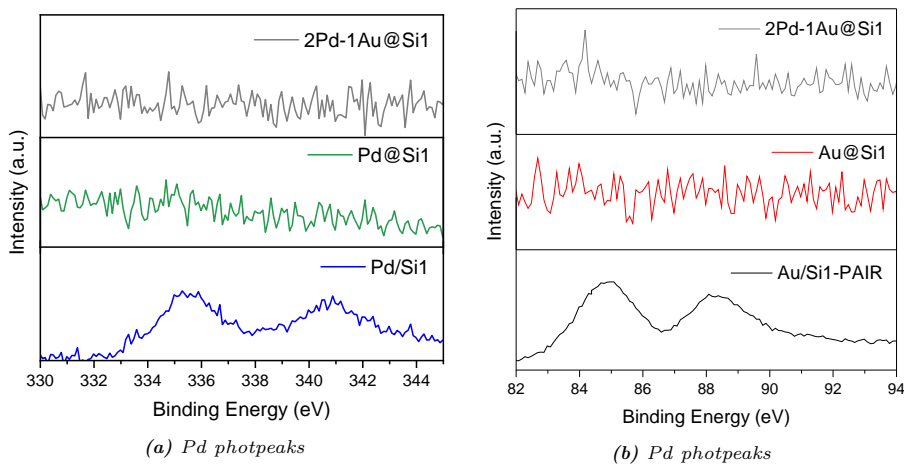


Figure 4.9: XPS spectra of synthesised materials.

4.3.1.6 H₂-TPR

Figure 4.10 shows the H₂-TPR of the investigated materials in the temperature range 50 to 200 °C. The sample Pd@Si1 showed the TCD signal in the range of 115 – 125 °C whereas Au@Si1 and Au/Si1-PAIR showed higher TCD signals in the range 75 – 90 °C. The bimetallic catalyst 2Pd-Au@Si1 showed a shift in the TCD signals

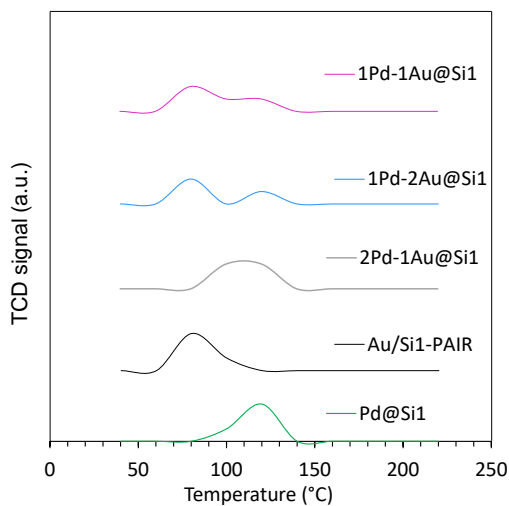


Figure 4.10: TPR profile of investigated materials.

with a broad peak in the range 90 to 130 °C. The samples 1Pd-1Au@Si1 and 1Au-2Pd@Si1 showed two distinct TCD signals, one in Au region and other in Pd region. Additionally, the TCD signals of 1Pd-Au@Si1 was more broader as compared to 1Pd-2Au@Si1. The appearance of broader TCD signals was possibly due to the alloys formed in the bimetallic system as the TCD is the characteristics of reducibility of metal nanoparticles [26, 139].

4.3.2 Catalytic activity

The catalytic activity for formic acid decomposition to CO_2 and H_2 were tested using all synthesised catalysts for temperature ranging from 20 to 200 °C. Figure 4.11(a) shows the hydrogen yield of Pd/Si1 and Pd@Si1. The material Pd@Si1 was highly active and showed 50% conversion at 98 °C while Pd/Si1 showed 50% activity at 140 °C. The activity of Pd@Si1 reached to full conversion at 140 °C. At 200 °C, both Pd/Si1 and Pd@Si1 showed 92% yield of H_2 . Figure 4.11(b) shows the yield of H_2

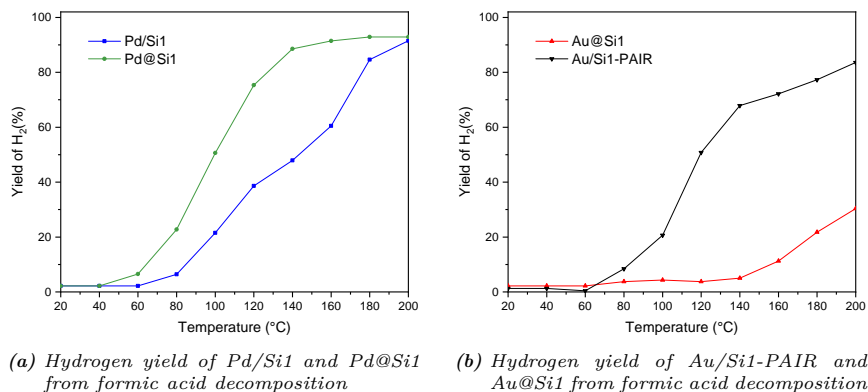


Figure 4.11: Hydrogen yield for synthesised materials.

for Au/Si1-PAIR and Au@Si1. Surprisingly, the Au@Si1 showed least activity and reached only 30% yield of H_2 at 200 °C. The Au/Si1-PAIR showed 50% yield of H_2 at 117 °C and was significantly higher as compared to Au@Si1. Figure 4.12 shows the yield of H_2 for the bimetallic catalytic system (2Pd-1Au@Si1, 1Pd-1Au@Si1 and 1Pd-2Au@Si1) and Pd@Si1 and Au/Si1-PAIR. Pd@Si1 and Au/Si1-PAIR were used to compare the activity as they showed higher catalytic activity over its counterpart. Additionally, the effect of ratio between Pd and Au on H_2 yield over the temperature 120 and 200 °C was plotted in Figure 4.13. Among all synthesised materials, 2Pd-

1Au@Si1 showed the best catalytic performance with 50% yield of H_2 at 85 °C and 99% yield of H_2 from 130 °C. 1Pd-1Au@Si1 showed 50% yield at 110 °C whereas 50% yield for 1Pd-2Au@Si1 was obtained at 137 °C. Furthermore, 98% H_2 yield was achieved with 1Pd-1Au@Si1 from 160 °C. Among all synthesised materials, 50% yield

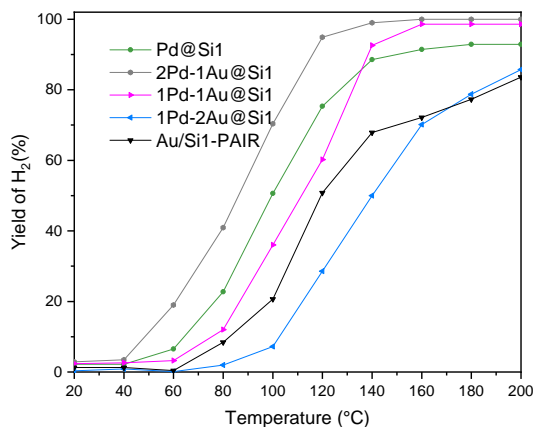


Figure 4.12: Hydrogen yield for bimetallic catalytic system.

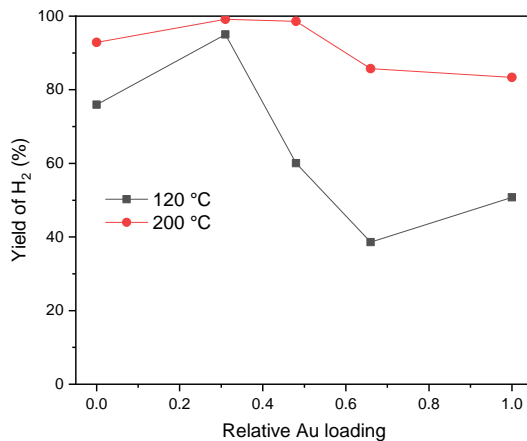


Figure 4.13: Effect of Pd/Au loading on hydrogen yield.

was achieved in the decreasing order of the temperature as 2Pd-1Au@Si1 > Pd@Si1 > 1Pd-1Au@Si1 > Au/Si1-PAIR > 1Pd-2Au@Si1. In general, the bimetallic catalysts 2Pd-1Au@Si1 and 1Pd-1Au@Si1 showed high H_2 yield. This high activity can be due to the formation of Pd-Au alloy when mixed. According to Hume-Rothery rule,

two metals (in this case, Pd and Au) can incorporate into fcc lattice of each other to form alloys when the atomic radii of both metals are relatively small and the relative difference between the radii is less than 15% [128, 153]. The TEM images of the catalysts and absence of additional peaks in XRD patterns have already confirmed the size of nanoparticles to be very small. Additionally, the broad TPR profile in H_2 -TPR plots further strengthens the argument of the formation of Pd-Au alloys in bimetallic catalysts 2Pd-1Au@Si1 and 1Pd-1Au@Si. The high activity of 2Pd-1Au@Si1 as compared to 1Pd-1Au@Si has possibly emerged from the Pd enriched site of Pd-Au alloys at high Pd:Au ratio [154]. Table 4.3 gives the site time yield at 120 °C for all investigated materials. 2Pd-Au@Si1 showed high site time yield of 7054 mol(H_2)/mol(Pd-Au)/h.

Table 4.3: *STY of investigated materials.*

Catalysts	Yield of Hydrogen at 120 °C (%)	STY mol(H_2)/mol(Pd-Au)/h
Pd/Si1	38.0	2213
Pd@Si1	75.0	4659
Au@Si1-PAIR	50.7	5433
Au@Si1	3.7	491
2Pd-1Au@Si1	94.1	7054
1Pd-1Au@Si1	60.2	4753
1Pd-2Au@Si1	28.5	1991

As discussed in the introduction, it is critical to reduce or eliminate CO formation and therefore higher selectivity towards H_2 in formic acid decomposition. CO can cause electrode poisoning in the fuel cell and therefore CO-free decomposition is significant for its commercial application. Figure 4.14 shows the CO selectivity of all investigated materials for temperature ranging from 20 to 200 °C. As the temperature goes up, the CO selectivity of all materials was increased. The catalyst Au/Si1 showed least CO selectivity while Pd@Si1 showed highest CO selectivity of all investigated materials. All materials showed <1% CO selectivity up to 150 °C. Moreover, 2Pd-1Au@Si1 exhibited only 0.7% CO selectivity even at 200 °C, which even can be due to some artefacts related to IR instruments used for the catalytic activity testing.

The catalysts stability test was carried at 120 °C for 25 h. Figure 4.15 shows the yield of H_2 over time for 2Pd-1Au@Si1 and Pd@Si1. The catalyst 2Pd-1Au@Si1

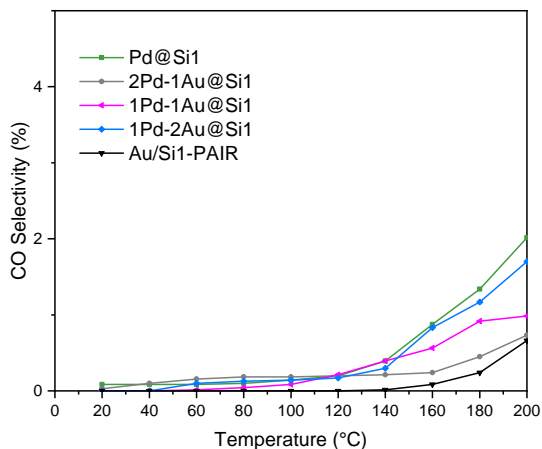


Figure 4.14: Selectivity towards CO for investigated materials.

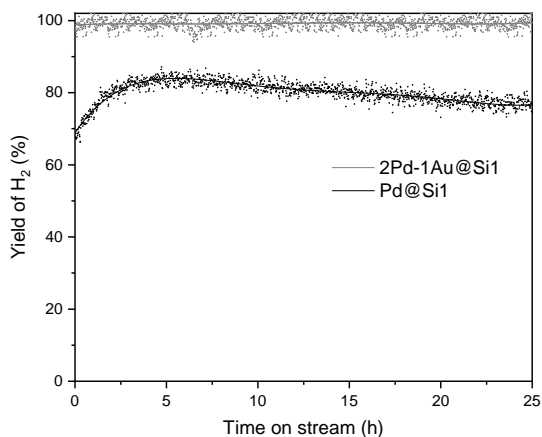


Figure 4.15: STY at 120 °C over 25 h of formic acid decomposition.

showed retained its activity even after 25 h under continuous formic acid flow while the hydrogen yield of Pd@Si1 was slowly reduced over time.

To distinguish the mechanism for formic acid between various investigated materials, in-situ DRIFT was carried out. The experiment was conducted by ME-PSD-DRIFTS method reported by Priya et al [155]. This method can reduce or avoid the unreacted and background noises during the DRIFTS measurement. Figure 4.16 shows the DRIFT spectra for Si1 and Pd@Si1 whereas Figure 4.17 shows the DRIFT spectra for 2Pd-Au@Si1 and Au@Si1-PAIR. The spectra were plotted over the

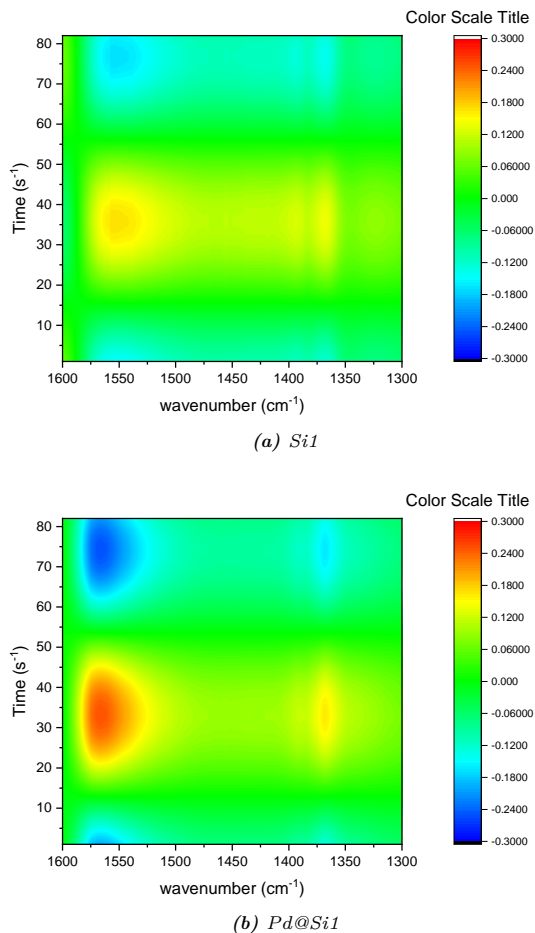


Figure 4.16: *In-situ DRIFT spectra for Si1 and Pd@Si1.*

wavenumber range of 1300 to 1600 cm^{-1} , where the bidentate and monodentate formate species were expected to appear [156]. The in-situ DRIFT spectra of silicalite-1 zeolite shown in Figure 4.16(a) showed less intense spectra as no reaction occurred at silicalite-1 surface [131]. The spectra of other materials were characterized by the presence of peaks in the region 1600 - 1300 cm^{-1} . These peaks can be assigned for the ν_{as} (OCO) and ν_s (OCO) stretching modes of carboxyl species of formate corresponding to the pathway for CO_2 . The presence of peaks at 1380 and 2345 cm^{-1} corresponding to physisorbed CO_2 confirms the production of CO_2 . Although a peak appeared at 1340 cm^{-1} for all catalysts which correspond to monodentate

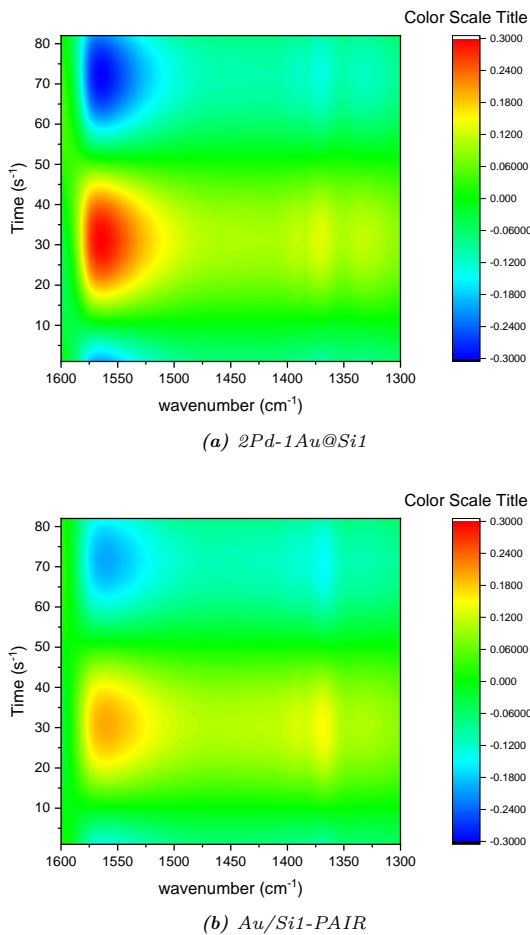


Figure 4.17: In-situ DRIFT spectra for *2Pd-1Au@Si1* and *Au/Si1-PAIR*.

formate species, no adsorption peaks corresponding to CO were detected in the range of 1900 to 2100 cm^{-1} for any of the investigated catalysts. This confirms that CO was not formed in the decomposition of formic acid [157]. Apart from Pd@Si1 having slightly higher intensity at 1340 cm^{-1} , the DRIFT spectra were almost identical for all catalysts and therefore shows a similar reaction mechanism for all the synthesised catalysts in the decomposition of formic acid [158].

4.4 Summary

The work reports an efficient and highly selective bimetallic heterogeneous catalyst comprised of Au and Pd metal nanoparticles encapsulated in silicalite-1 zeolite for the decomposition of formic acid to hydrogen. Au and Pd nanoparticles were encapsulated in silicalite-1 using various methods including incipient wetness impregnation, in-situ encapsulation and pressure-assisted impregnation. Among all synthesised materials, the bi-metallic catalyst comprised of Au and Pd, 2Pd-1Au@Si1, showed the best catalytic performance with 50% yield of H₂ at 85 °C and 99% yield of H₂ from 130 °C. The catalyst 2Pd-1Au@Si1 also showed the highest stability and retained its activity even after 25 h under continuous formic acid flow. The high activity of the bimetallic catalyst 2Pd-1Au@Si1 can attribute to the formation of Pd-Au alloy and enriched Pd site on the alloy due to higher Pd:Au ratio. The catalyst 2Pd-1Au@Si1 also exhibited the lowest selectivity of 0.7% for CO even at 200 °C. The in-situ DRIFTS further confirmed that no CO was formed in the decomposition of formic acid.

Considering the future need of hydrogen storage system and demand for biomass-derived chemicals, the bimetallic heterogeneous catalyst comprised of Au and Pd metal nanoparticles supported on silicalite-1 is a potential candidate for large scale production of hydrogen from bio formic acid. Although the activity of synthesised catalysts is lower than homogeneous catalysts, factors such as stability, separability and low-cost solution can still favour the heterogeneous systems for the commercial application.

CHAPTER 5

Selective Conversion of Ethanol to Acetaldehyde

Acetaldehyde is an organic intermediate used commercially as a food preservative and an ingredient in fuels, glues, and caulking compounds. This chapter describes an efficient production of acetaldehyde from dehydrogenation of ethanol. The reaction occurs over a heterogeneous catalyst comprising Cu nanoparticles supported on nitrogen-doped ordered mesoporous carbon. The chapter addresses synthesis methodology, characterisation, catalytic test results and identifies the optimum catalyst for the synthesis of acetaldehyde. The chapter also investigates the catalytic effect of important synthetic parameters, such as polymerisation and calcination temperature. Some of the results presented in this chapter are based on the manuscript “Dehydrogenation of bioethanol using Cu nanoparticles supported on N-doped ordered mesoporous carbon”.

5.1 Introduction

Acetaldehyde with the chemical formula CH_3CHO is an organic intermediate, which is used in the manufacture of perfumes, leather tanning, dyes, drugs, silvering of mirrors, etc. It is an ingredient in some fuels, glues, and caulking compounds and is used to preserve fish and fruits. The largest application segment for acetaldehyde market is the food and beverage segment. The acetaldehyde has a global market size of USD 1.6 billion in 2018 and is projected to reach USD 1.80 billion by 2022, at a CAGR of 6.24% during the forecast period [159, 160]. Traditionally, acetaldehyde is synthesised by the oxidation of ethylene, also known as the Wacker process and uses a non-renewable starting material [37, 161]. The alternative way to synthesis acetaldehyde is utilising bioethanol as the starting material, which can be produced

from biomass through the fermentation process as described in Chapter 1.

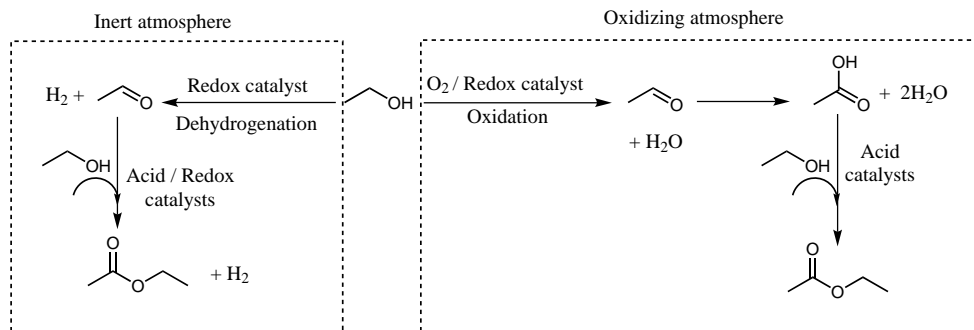


Figure 5.1: Conversion of ethanol to acetaldehyde.

Ethanol can be converted to acetaldehyde via oxidation or dehydrogenation pathway. Figure 5.1 shows oxidation and dehydrogenation pathways and the possible products formed during the conversion of ethanol to acetaldehyde [25, 162, 163]. The selective dehydrogenation of ethanol under the inert atmosphere can produce acetaldehyde and H_2 stoichiometrically [164, 165]. The dehydrogenation of ethanol has been extensively studied using Cu-based catalysts due to its relatively good selectivity towards acetaldehyde. The reaction utilised copper chromite catalysts in the past. However, it always ended up with the formation of side products such as ethyl acetate, acetic acid, crotonaldehyde and chromic compounds making it both less selective and environmentally hazardous [27, 161, 166–168]. In recent studies, supported copper catalysts such as Cu/Zeolites [169], Cu-ZnO [27], Cu-SiO₂ [15, 170], Cu-Al₂O₃ [171], Cu-ZnO-Al₂O₃ [2], Cu/carbon [172, 173], Cu/GO [174] etc., were reported in research outcomes for dehydrogenation reaction. However, the low melting point of Cu nanoparticles resulting in rapid sintering and fast oxidation of Cu to its oxide in the presence of an oxidising atmosphere like water or oxygen/air leads to the deactivation of Cu-based catalyst and thus limit the application of Cu based catalysts for industrial application [168].

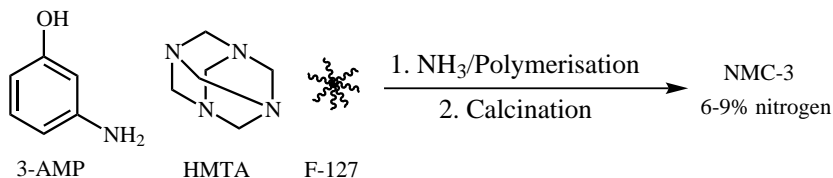
The immobilisation of Cu nanoparticles in mesoporous carbon is particularly interesting for several reasons. First of all, the confinement can help to stabilise the Cu nanoparticles during catalytic reactions [173]. Moreover, it can increase the selectivity towards acetaldehyde by providing an inert environment which can prevent the formation of side products. However, the weak interaction between Cu and carbon can result in the increased migration of Cu nanoparticles on the carbon

support. Carbon materials with their neutral surface and sp² planar structure tend to interact with Cu nanoparticles in a feeble manner which results in the destabilisation and deactivation of Cu nanoparticles [174, 175].

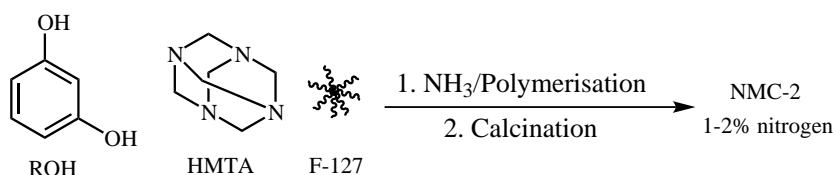
Studies have shown that copper supported over carbon materials doped with nitrogen can exploit the advantage of the known high attraction of Cu towards nitrogen species [15, 175–177]. Dimitri et al. reported nitrogen-doping for the stabilisation of Cu nanoparticles on a carbon support and its application for formic acid decomposition [175]. Moreover, studies have shown that graphitic-nitrogen can be used to stabilise Cu nanoparticles in different N-doped carbon supports such as PPC, CMC in ethanol dehydrogenation to acetaldehyde [78]. M.V. Morales et al. reported Cu supported on graphite and reduced graphene oxide functionalised with nitrogen group for bioethanol conversion to acetaldehyde [174]. However, a comprehensive study relating the effect of nitrogen content and nature on stability, activity and dispersion of Cu nanoparticles are still lacking in any of these reported cases.

As part of this Ph.D. work, copper nanoparticle supported on ordered mesoporous carbon was used for the selective formation of acetaldehyde via dehydrogenation pathway of ethanol in a heterogeneous gas-phase catalytic system. The performance of synthesised catalysts are compared with the commercially available Cu on activated carbon. Three types of ordered mesoporous carbon were synthesised by altering the nitrogen content. To distinguish the nitrogen loading of synthesised mesoporous carbon, the terminology NMC-1, NMC-2 and NMC-3 were used throughout the course of this chapter. NMC-1 is used for ordered mesoporous carbon with zero nitrogen doping, whereas NMC-2 and NMC-3 represent approx. 2 and 7% nitrogen doping. Figure 5.2 shows the synthesis scheme for three synthesised materials with different carbon-nitrogen precursors. The synthesis of NMC-3 uses nitrogen-containing functional groups 3-AMP (3-aminophenol) and hexamethylenetetramine (HMTA) as the precursor contributing to the high nitrogen content of ordered mesoporous carbon. In NMC-2 synthesis, one precursor 3-AMP was replaced with ROH (resorcinol) having no nitrogen functional group whereas both 3-AMP and HMTA was exchanged with nitrogen-free reagents like ROH, formaldehyde (FA) and Na₂CO₃ for the synthesis of NMC-1.

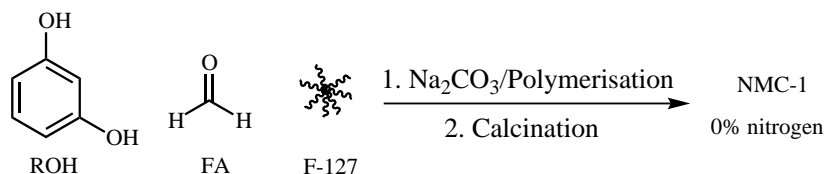
The later section of this chapter investigates the impact of synthesis parameters such as polymerisation and calcination temperatures on pore structure, surface area of mesoporous carbon and subsequently on the catalytic activity of mesoporous carbon.



(a) Synthesis of NMC-3



(b) Synthesis of NMC-2



(c) Synthesis of NMC-1

Figure 5.2: Synthesis of nitrogen-doped ordered mesoporous carbon.

5.2 Experimental Section

5.2.1 Materials

Chemicals used for this reaction includes hexamethylenetetrammine (HMTA, 99%), Pluronic F-127 ($M_n \sim 12\,500$), 3-aminophenol (98%), resorcinol ($\geq 99\%$), formaldehyde (37%), sodium carbonate (99%), aqueous ammonia solution (28% in water), copper nitrate ($\text{Cu}(\text{NO}_3)_2 \cdot 2.5 \text{H}_2\text{O}$, $\geq 99.99\%$), ethanol ($> 99.8\%$) and copper on activated carbon (commercially available, 3% Cu). All above chemicals were reagents grade and used without further purifications.

5.2.2 Synthesis of materials

This section describes the synthesis process of various ordered mesoporous carbon and catalysts prepared for the dehydrogenation reaction.

5.2.2.1 Synthesis of NMC-3

In a 500 ml round bottom flask, F-127 (8.8 g) was dissolved in 208 ml deionised water by stirring it for 10 min at room temperature. 3-AMP (4.4 g) and HMTA (2.8 g) were added to the above mixture and stirred it for another 30 min at room temperature. To the resulting clear solution, aqueous ammonia solution (28%, 8 ml) was added and stirred at 80 °C for 24 h. The resulting dark-brown mixture was centrifuged and washed with deionised water several times under 12000 rpm (20 min each time). The product was kept in an oven at 80 °C and then ground into powders. The resulting brown powder was carbonised at 600 °C under the flow of Ar (50 ml/min) by heating with 1 °C/min ramp and kept for 3 h.

5.2.2.2 Synthesis of NMC-2

The synthesis of NMC-2 and NMC-3 differed only in one of the precursor and therefore followed the same procedure of NMC-3 described in Section 5.2.2.1 except that 4.4 g of resorcinol was used instead of 3-aminophenol.

5.2.2.3 Synthesis of NMC-1

To make nitrogen-free mesoporous carbon NMC-1, HMTA was replaced with formaldehyde (37%, 8.85 ml) and sodium carbonate (20 mg) was added instead of aqueous ammonia solution. All other procedure remained the same as NMC-3 described in Section 5.2.2.1.

5.2.2.4 Synthesis of Catalysts

Incipient wetness impregnation described in Chapter 1:Section 1.3 was used for the synthesis of Cu supported on ordered mesoporous carbon. The impregnation was carried out using $(\text{Cu}(\text{NO}_3)_2 \cdot 2.5 \text{H}_2\text{O})$ as Cu precursor. As an example, $(\text{Cu}(\text{NO}_3)_2 \cdot 2.5 \text{H}_2\text{O})$ (0.0511 g) was dissolved in absolute ethanol (0.11 g). The prepared solution was added to the NMC-3(0.485 g) in drops and mixed thoroughly after the addition of each drop. The resulting material was dried at 80 °C for overnight and reduced with H_2 (50 ml/min) at 450 °C for 2 h with a heating rate of 5 °C/min to synthesis 3 wt% Cu supported NMC-3. A similar procedure was carried out for preparing catalysts with different wt% Cu (1, 3 and 8%) over NMC-1, NMC-2 and NMC-3. Catalysts

were numbered xCu/NMC-y (with x being the Cu loading and y representing the nitrogen doping).

5.2.3 Characterisation

All the samples were characterised using various techniques including XRD, nitrogen physisorption, SEM, TEM, CHN analysis, ICP-OES, XPS and DRIFTS. The equipment used and conditions applied for different analysis are specified in Chapter 3.

5.2.4 Gas-phase conversion of bioethanol to acetaldehyde

A fix-bed quartz tubular reactor under atmospheric pressure was used for the gas-phase dehydrogenation of ethanol to acetaldehyde. For the synthesis of 3Cu/NMC-3, the reactor was loaded with 18.5 mg of catalyst mixed with fractionated quartz crystals of the size 300-355 μm . This was followed by the reduction at 450 $^{\circ}\text{C}$ for 90 min under the flow of 10% H_2/N_2 (50 ml/min). After lowering the temperature to 350 $^{\circ}\text{C}$, 10% ethanol-water solution with a weight hourly space velocity (WHSV) = 12.79 g ethanol/g catalyst h^{-1} , was introduced along with nitrogen gas (50 ml/min)

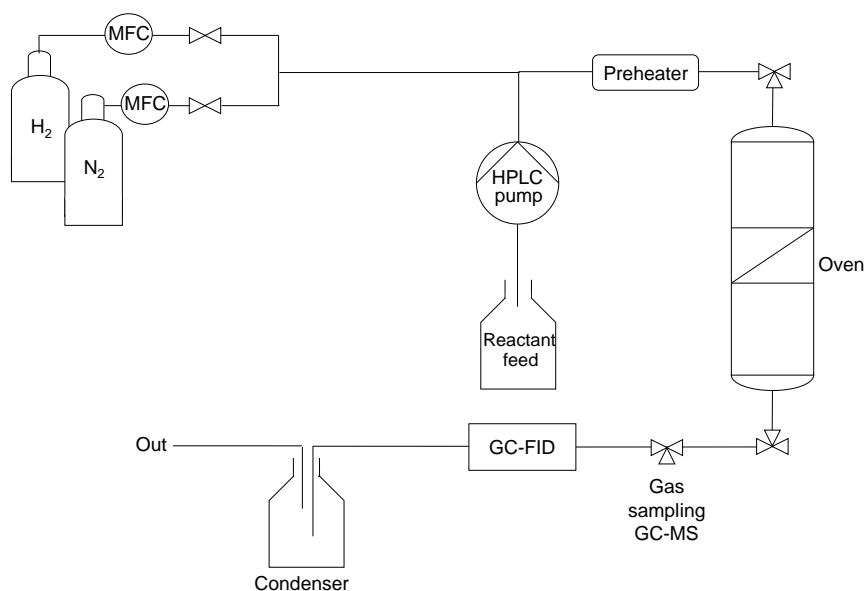


Figure 5.3: Schematic illustration of reactor flow setup.

into an evaporator (120 °C) with gas hourly space velocity (GHSV) = 21250 h⁻¹. The outlet of the reactor was set with a cold trap which leads the product mixture to an online GC, equipped with a flame ionisation detector (FID). The product was analysed using GC-FID on every 20 min. To identify the product components, gas samples were collected from the outlet of the reactor set-up and injected in GC-MS. The schematic for the reactor flow setup is shown in Figure 5.3.

5.3 Results and discussions

This section describes the results obtained through various characterisation techniques used for as-synthesised catalysts. This is followed by the test for performance of all the synthesised catalyst for the dehydrogenation reaction. In total, NMC-1 with 3 wt% Cu loading and NMC-2 and NMC-3 with 1, 3 and 8 wt% Cu loading were synthesised and studied.

5.3.1 Characterisation results

5.3.1.1 CHN analysis

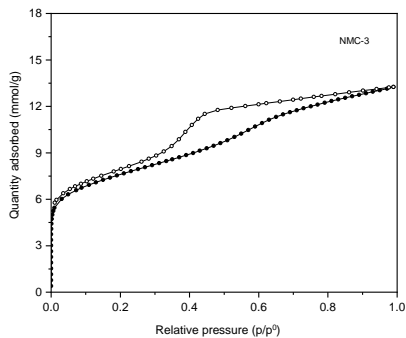
The elemental composition(carbon, nitrogen and hydrogen) of the mesoporous carbon support were analysed through CHN analyser and the results are shown in Table 5.1. As expected, nitrogen content increased in the order NMC-3 > NMC-2 > NMC-1, with NMC-3, NMC-2 and NMC-1 having \approx 9.4%, 1.5% and 0.4% of N. 0.4% N in the elemental analysis for NMC-1 could be due to the atmospheric nitrogen or some artefacts during the measurements.

Table 5.1: Elemental composition (CHN) of mesoporous carbon support.

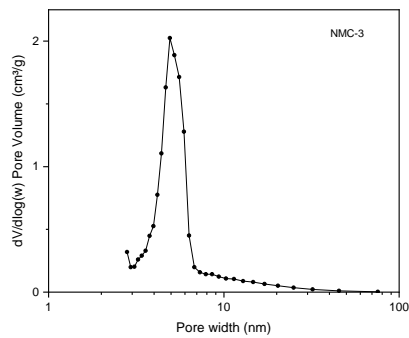
Catalyst	Carbon (%)	Nitrogen (%)	Hydrogen (%)
3Cu/NMC-3	84.1	9.4	6.5
3Cu/NMC-2	86.1	1.5	12.4
3Cu/NMC-1	89.1	0.4	9.7

5.3.1.2 Nitrogen physisorption

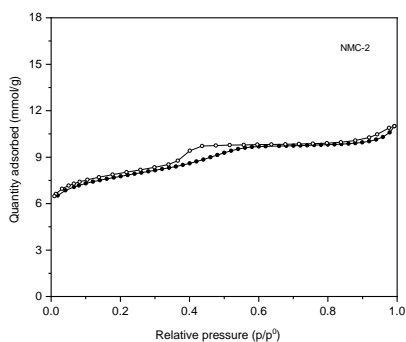
Figure 5.4(a),(c) and (e) show the nitrogen physisorption isotherm of three ordered mesoporous carbon NMC-3, NMC-2 and NMC-1, respectively.



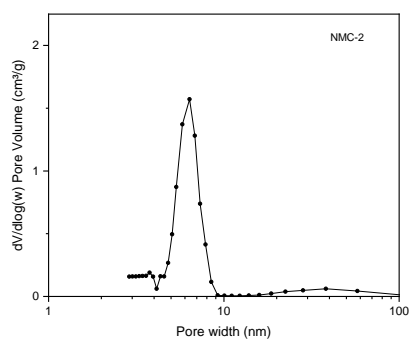
(a) Physisorption isotherm of NMC-3



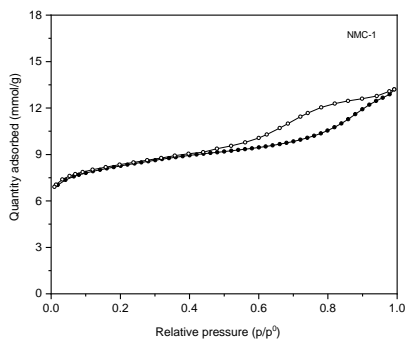
(b) Pore width distribution of NMC-3



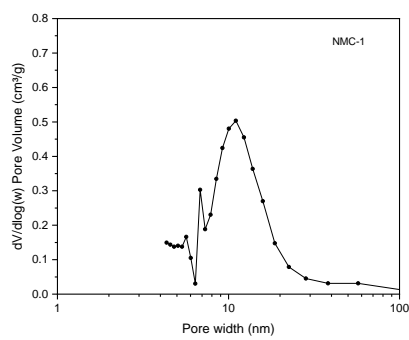
(c) Physisorption isotherm of NMC-2



(d) Pore width distribution of NMC-2



(e) Physisorption isotherm of NMC-1



(f) Pore width distribution of NMC-1

Figure 5.4: Nitrogen physisorption analysis of prepared materials.

All ordered mesoporous carbon support showed type IV(a) isotherm with hysteresis loop H4 [98, 178]. As described in Chapter 3, this type of isotherm is typical for mesoporous support where capillary condensation takes place in mesopores of the materials. Hysteresis loops for NMC-1, NMC-2 and NMC-3 closes at $p/p^0 = 0.3, 0.38$ and 0.45 , respectively. Figure 5.4(b), (d) and (e) show the pore width distribution of the samples, where NMC-1, NMC-2 and NMC-3 showed the pore size distribution around 10 nm, 7 nm and 5 nm, respectively. However the presence of mesoporosity is clear from the pore size distribution plot, the size of pores is different for all samples. This is possibly due to the different carbon precursors used for the synthesis.

Table 5.2: Nitrogen physisorption data.

Catalysts	V_{total}^a cm^3g^{-1}	V_{micro}^b cm^3g^{-1}	S_{BET}^c m^2g^{-1}
NMC-3	0.529	0.09	578
NMC-2	0.478	0.11	602
NMC-1	0.411	0.17	590

^a V_{total} determined from the isotherm adsorption branch at around $p/p^0 = 0.95$.

^b V_{micro} calculated by the t -plot method.

^c S_{BET} calculated by the BET method.

Table 5.2 shows the total pore volume, micropore volume of the ordered mesoporous carbon support and specific surface area calculated by the BET method. The S_{BET} increased in the order $\text{NMC-2} > \text{NMC-1} > \text{NMC-3}$.

5.3.1.3 XRD

Figure 5.5(a) shows the XRD pattern of 1Cu/NMC-3, 3Cu/NMC-3 and 8Cu/NMC-3. The materials with 3 and 8 wt% of Cu showed a characteristic peak at 43° (2θ) corresponding to Cu(III) plane. However, the XRD pattern of 1Cu/NMC-3 showed no characteristic peak of copper owing to the highly dispersed copper particle at low concentration on the carbon support [82]. The formation of larger nanoparticles at high metal loading resulted in a high Cu(111) peak.

Cu(111) plane intensity of three ordered mesoporous carbon was compared and results are shown in Figure 5.5(b). Although the metal loading was similar for all three samples, the intensities of Cu(111) plane decreased in the order $\text{NMC-3} < \text{NMC-2} < \text{NMC-1}$ due to more dispersed and smaller nanoparticle of Cu in the NMC-3.

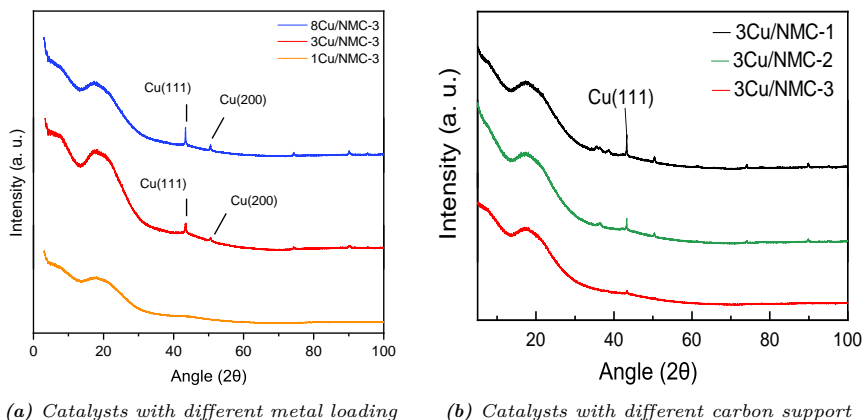


Figure 5.5: XRD pattern for prepared materials.

5.3.1.4 SEM

Figure 5.6 and 5.7 shows the SEM images of the as-synthesised ordered mesoporous carbon support. The materials showed different particle morphology with NMC-3 exhibiting hexagonal like structure while NMC-2 showed spherical like structure. NMC-1, on the other hand, showed a random structure. This structural variation for NMC-1, NMC-2 and NMC-3 accounts for the different reagent used for the synthesis of different mesoporous carbon.

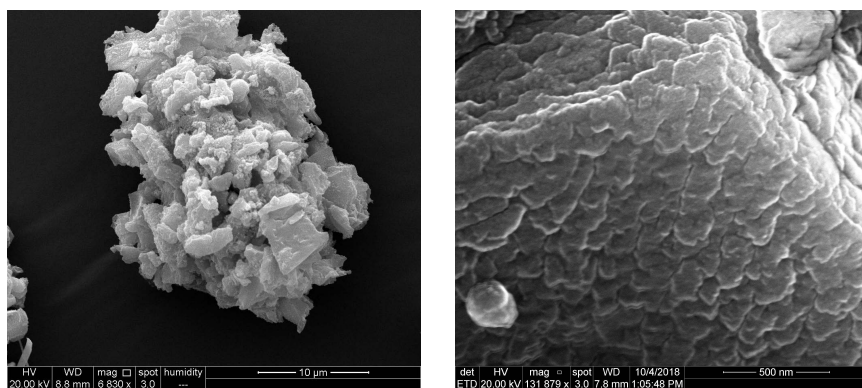


Figure 5.6: SEM images of NMC-1.

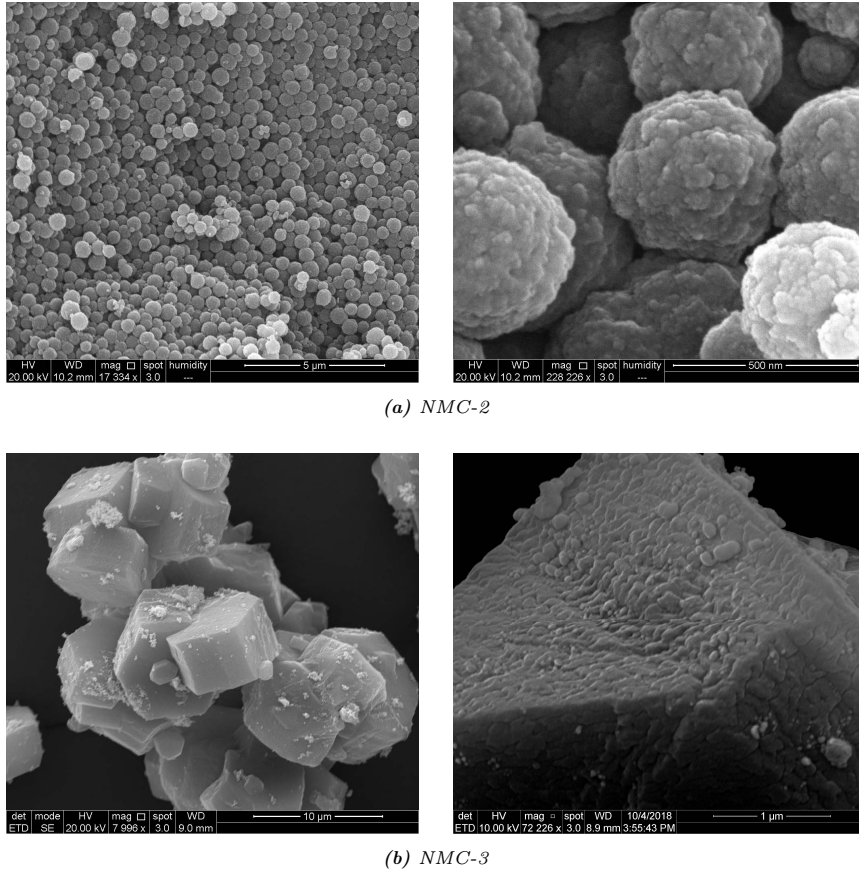
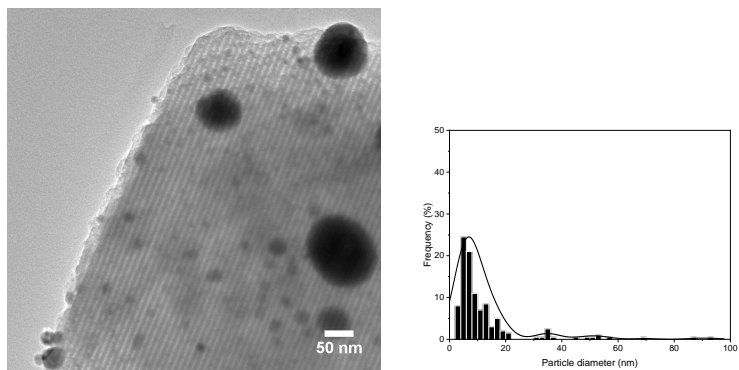


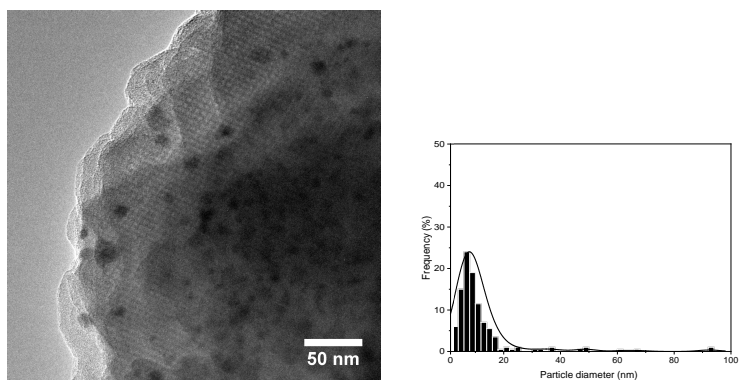
Figure 5.7: SEM images of prepared materials.

5.3.1.5 TEM

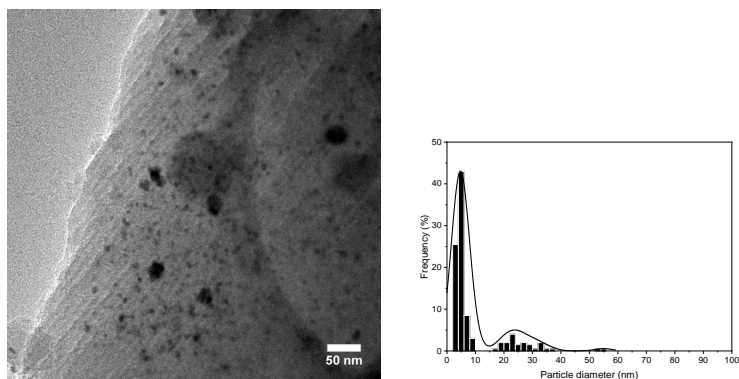
Figure 5.8 shows the TEM images and particle size distribution of Cu nanoparticles supported on NMC-1, NMC-2 and NMC-3 with metal loading 3 wt%. The particle size distribution was measured by picking > 200 particles in different images. The Cu nanoparticles in 3Cu/NMC-3 was small with an average particle size of 6.4 nm. In comparison to the 3Cu/NMC-3, the particle size distribution of 3Cu/NMC-1 and 3Cu/NMC-2 was broader with an average particle size of 12.4 nm and 11.5 nm, respectively.



(a) 3Cu/NMC-1



(b) 3Cu/NMC-2



(c) 3Cu/NMC-3

Figure 5.8: TEM images and particle size distribution of prepared materials.

Although few large particles can be seen in the image of 3Cu/NMC-3, the STEM-HAADF image showed almost all the particles with the size in the range of 4-6 nm (Figure 5.9). The TEM images for Cu nanoparticles supported on NMC-3 with metal loading 1 and 8 wt% are shown in Figure 5.10. Similar to 3Cu/NMC-3, TEM images for both these samples showed uniformly distributed nanoparticles throughout the mesoporous materials.

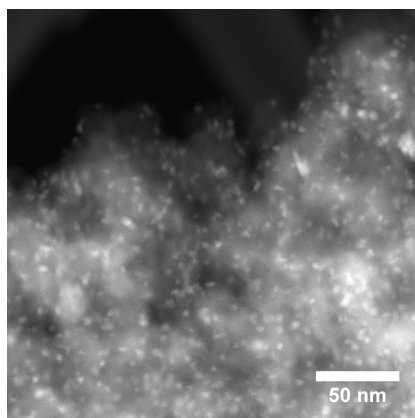


Figure 5.9: HAADF image of 3Cu/NMC-3.

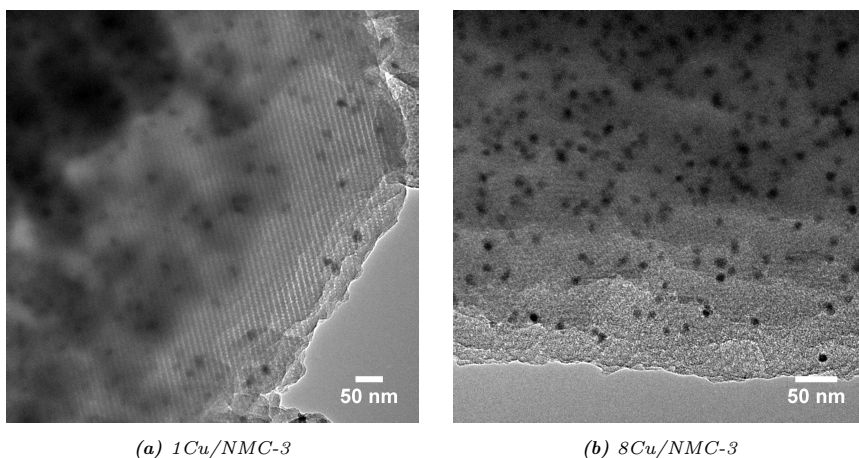
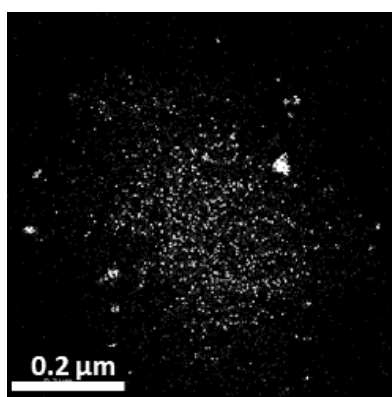


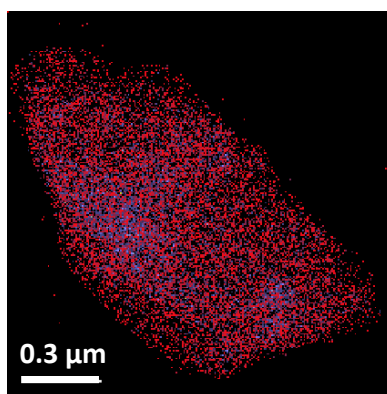
Figure 5.10: TEM images of prepared materials with different metal loadings.

5.3.1.6 EDX

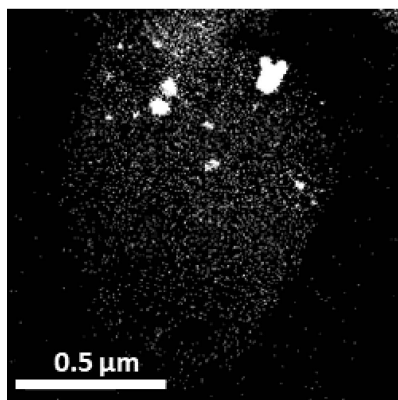
The surface elemental distribution of copper and nitrogen in 3Cu/NMC-3 and 3Cu/NMC-2 are shown in Figure 5.11. The EDS elemental mapping of both samples showed N signals. However, the intensity of N signals was comparatively less for 3Cu/NMC-2 as compared to 3Cu/NMC-3. The intensity of Cu signals in 3Cu/NMC-2 and 3Cu/NMC-3 were almost similar and were uniformly distributed.



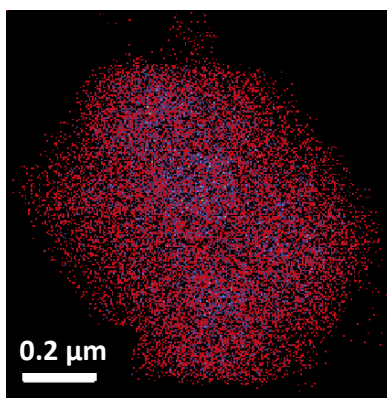
(a) Elemental mapping of Cu in 3Cu/NMC-3



(b) Elemental mapping of N in 3Cu/NMC-3



(c) Elemental mapping of Cu in 3Cu/NMC-2



(d) Elemental mapping of N in 3Cu/NMC-2

Figure 5.11: EDS elemental distribution of N and Cu in carbon support.

5.3.1.7 XPS

The surface composition of the catalyst materials were analysed using XPS technique. Figure 5.12 shows the N1s deconvolution spectra illustrating the effect of nitrogen species over NMC-2 and NMC-3 before and after Cu loading. Spectra can be attributed to 4 different peaks for NMC-3 denoted as N1, N2, N3 and N4 corresponding to pyridinic-N (398.2 eV), pyrrolic-N (399.9 eV), quaternary-N (400.7 eV) and pyridine N-oxide (402.7 eV), respectively [85, 179, 180]. The markable change in the spectra is owing to the Cu loading on mesoporous carbon support [181]. Both N1 and N2 peaks were shifted by approx. 1 eV towards higher binding energy due to the strong interaction of Cu with nitrogen species. A reduction in the relative intensity of N2 over N3 after impregnating Cu over NMC-3 stems from the interaction of Cu species with pyridinic-N [174, 175, 177, 182].

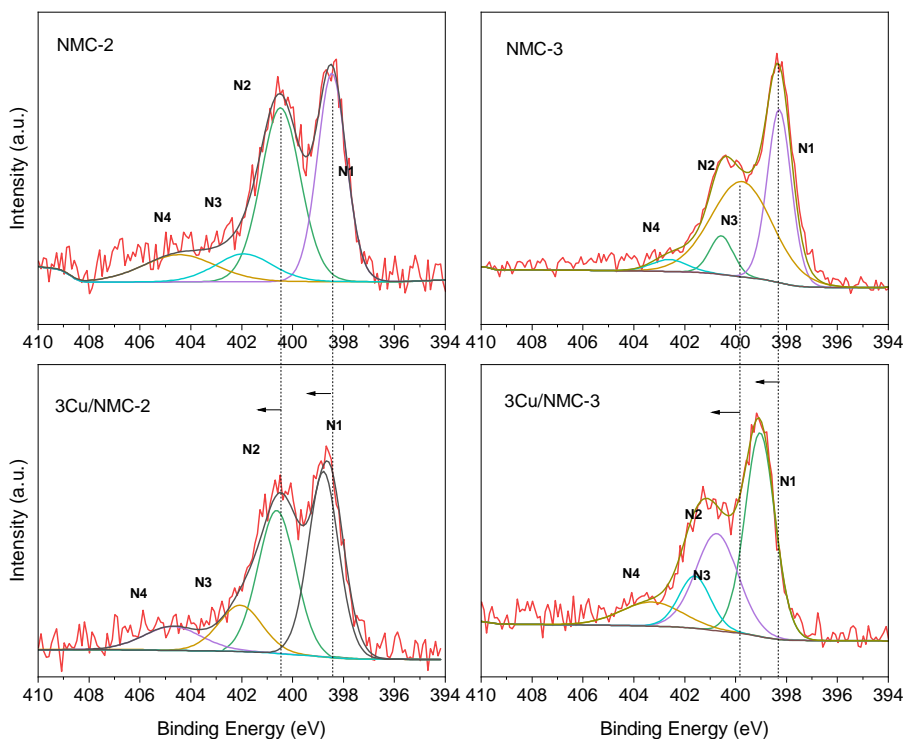


Figure 5.12: XPS N1s spectra of materials.

XPS analysis of Cu 2p_{3/2} peaks in as-synthesised catalysts is shown in Figure 5.13. As evident from the figure, there is a clear shift of binding energy for Cu⁰/Cu⁺

species for nitrogen-free (3Cu/NMC-1) and nitrogen-doped catalysts (3Cu/NMC-2 and 3Cu/NMC-3). Additionally, the absence of Cu^{2+} satellite peaks in Cu $2p_{3/2}$ spectra of 3Cu/NMC-3 implies the interaction between Cu and N in stabilisation [175, 177, 181].

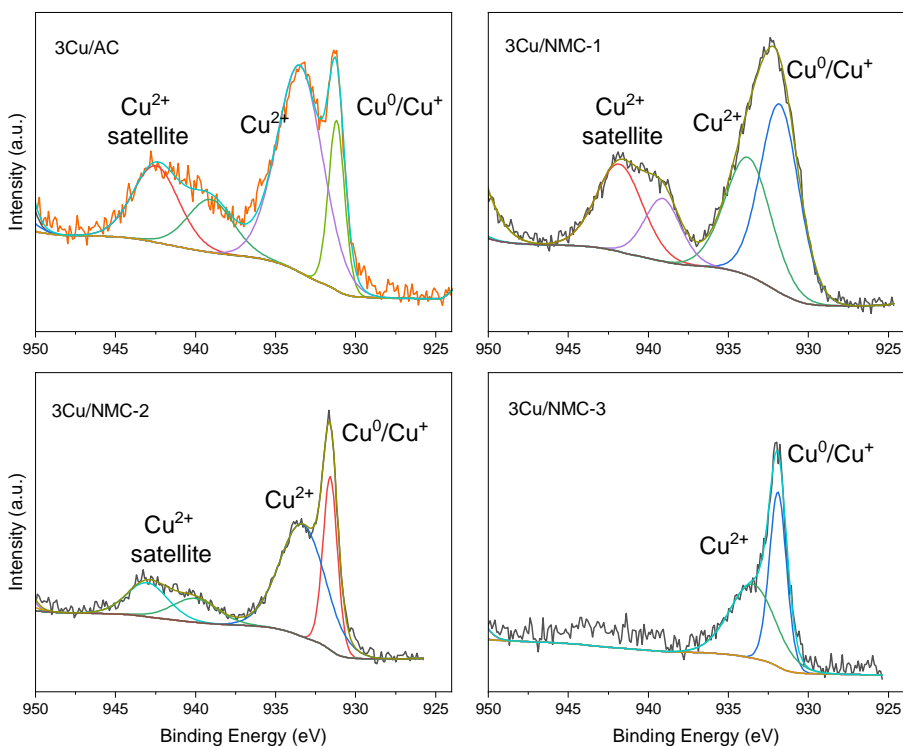


Figure 5.13: XPS Cu $2p_{3/2}$ spectra of materials.

Table 5.3: XPS data with surface elemental composition of synthesised catalysts.

Catalyst	Carbon (%)	Nitrogen (%)	Oxygen (%)	Copper (%)
3Cu/NMC-3	87.8	6.8	5.3	0.1
3Cu/NMC-2	88.6	1.5	8.8	1.1
3Cu/NMC-1	82.4	0.0	16.4	1.2

Table 5.3 shows the surface elemental composition measured through XPS data for 3Cu/NMC-1, 3Cu/NMC-2 and 3Cu/NMC-3. The results were in line with nitrogen

precursor used in the synthesis of ordered mesoporous carbon with a nitrogen content of 6.8% in NMC-3, 1.5% in NMC-2 and no traces of nitrogen on the surface of NMC-1. All samples showed Cu photopeaks with the concentration of 1.2, 1.1 and 0.1% for NMC-1, NMC-2 and NMC-3, respectively.

5.3.2 Catalytic activity

The dehydrogenation of ethanol to acetaldehyde was tested using all the prepared catalysts. Various parameters such as temperature, water content in ethanol, metal loading, precursors and stability over time were tested and analysed.

The reaction was carried out over a temperature range from 350 to 200 °C to study the effect of temperature over catalytic activity. The test was carried out using absolute ethanol as reactant feed with GHSV of 21250 h⁻¹. Figure 5.14 shows the yield of acetaldehyde as a function of temperature for 3Cu/NMC-1, 3Cu/NMC-2 and 3Cu/NMC-3. The same test is also carried out for 3 wt% copper on activated carbon (3Cu/AC) catalyst with pure ethanol under the same GHSV.

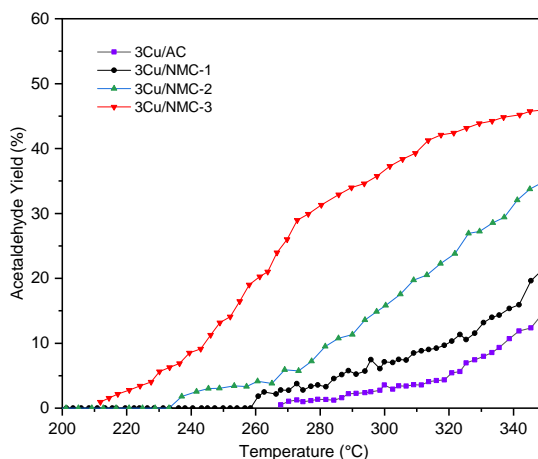


Figure 5.14: Effect of temperature on catalytic activity with pure ethanol as reactant feed.

The conversion and selectivity enhanced as the temperature increased and all catalysts showed > 99% selectivity towards acetaldehyde. The 3Cu/NMC-3 reached 46% yield of acetaldehyde at 350 °C. The commercially available 3Cu/AC showed the least conversion and selectivity as compared to the as-synthesised catalysts. It is worth to note here that 3Cu/NMC-3 showed higher catalytic activity from

a lower temperature of 210 °C as compared to 3Cu/NMC-2, 3Cu/NMC-1 and 3Cu/AC, which were only active from 238 °C, 260 °C and 268 °C, respectively. The catalytic performance illustrates the positive impact of small nanoparticles and/or high nitrogen content on catalytic activity.

As discussed in Chapter 1, ethanol produced through fermentation contains high water content and therefore dehydrogenation of ethanol to acetaldehyde has to be tested for ethanol with water content as the reactant feed to investigate the feasibility of using bioethanol for the production of acetaldehyde. For this reason, the reaction was carried out with 10% ethanol as reactant feed under the same GHSV and similar conditions as used for testing with absolute ethanol to study the catalytic activity.

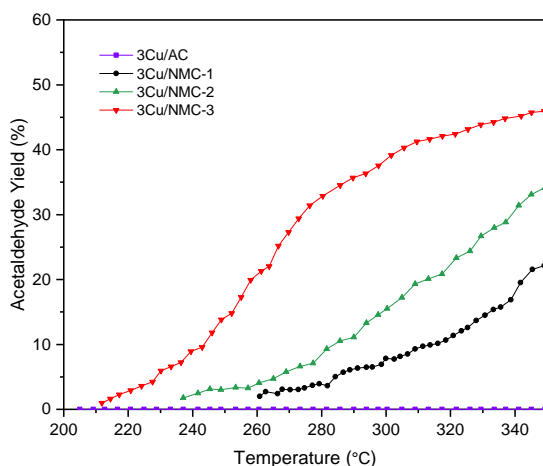


Figure 5.15: Effect of temperature on catalytic activity with bioethanol as reactant feed.

Figure 5.15 shows the yield of acetaldehyde and conversion as a function of temperature for bioethanol as reactant feed. As shown in the figure, 3Cu/AC showed no activity in the presence of water. This can be either due to the fast oxidation of Cu to its oxidised forms or by the sintering of Cu nanoparticles in the presence of steam. On the other hand, the catalytic activity of as-synthesised catalysts showed no markable influence of water. The conversion and yield of investigated catalysts followed the order NMC-3 > NMC-2 > NMC-1. The catalytic activity of the as-synthesised materials can be explained by the confinement effect of Cu in the mesopores of NMCs which stabilised the Cu nanoparticles in the presence of steam and high temperature. The small nanoparticles might be intact and strongly linked to

the NMC support and possibly inert hydrophobic ordered mesoporous carbon support (NMC-1, NMC-2 and NMC-3) which prevented the entry of water and allowed only ethanol to reach the Cu site. Moreover, the significant difference in the activity of investigated catalysts accounts for the difference in the size and dispersion of Cu nanoparticles. High activity of 3Cu/NMC-3 is possibly due to the effect of nitrogen loading resulting in highly dispersed Cu nanoparticles.

The effect of Cu loading of catalysts in the ethanol dehydrogenation is studied by testing 1Cu/NMC-3 and 8Cu/NMC-3 under the same reaction condition as for 3Cu/NMC-3. Figure 5.16 provides the comparison of the catalytic activity as a function of temperature for different metal loading using 10% ethanol as reactant feed. As shown in the figure, the higher the metal loading, the higher the conversion and yield. The 8Cu/NMC-3 showed 74% yield of acetaldehyde at 350 °C. The selectivity of the catalysts was > 99% in all cases. The higher activity of 8Cu/NMC-3 originates from high dispersion of Cu nanoparticles even at high Cu loading.

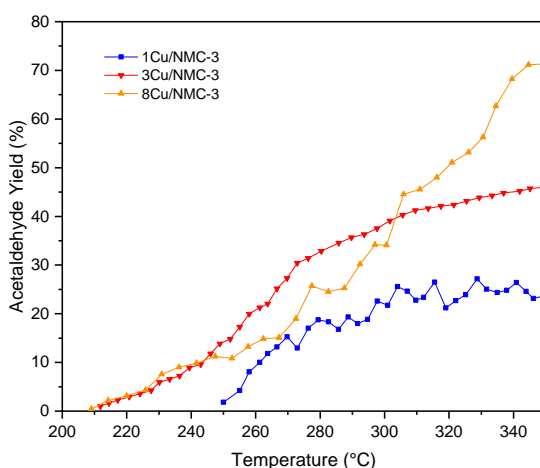


Figure 5.16: Effect of metal loading on catalytic activity.

To study the effect of different Cu precursors on nanoparticle dispersion, various Cu compounds such as copper methoxide, copper acetate, copper sulphate and copper carbonate were used and synthesised through either incipient wetness impregnation or wetness impregnation methods. In general, $\text{Cu}(\text{NO}_3)_2$ had the highest dissolution both in ethanol and water whereas other Cu compounds were difficult to dissolve in ethanol, water and other solvents.

Figure 5.17 shows the stability of the investigated materials tested at 260 °C with

GHSV of 21250 h^{-1} . The stability test for the materials 3Cu/AC and 3Cu/NMC-3 was carried out using absolute ethanol and the results are shown in Figure 5.17(a). Although both materials showed $> 99\%$ selectivity, the yield was significantly higher (26%) for 3Cu/NMC-3 as compared to 3Cu/AC ($< 4\%$). Additionally, 3Cu/NMC-3 showed very high stability even after 800 min whereas almost 50% of the activity declined for 3Cu/AC after 800 min. This difference in the activity is possibly due to the difference in the electronic structure of support and difference in the size of Cu nanoparticles.

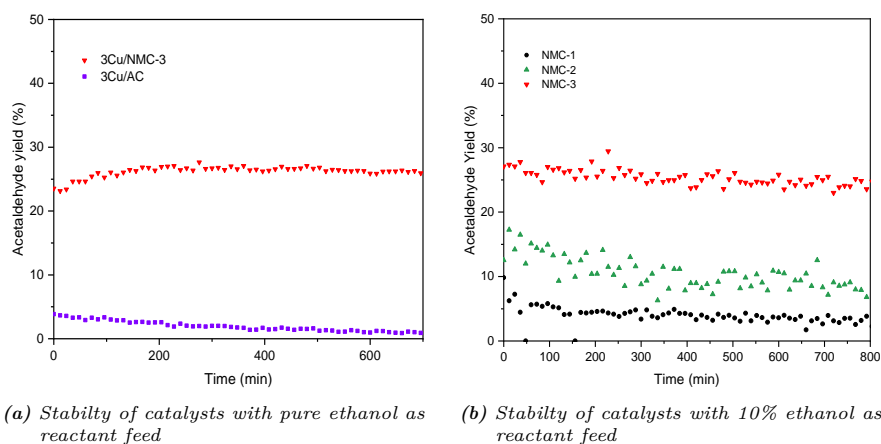


Figure 5.17: Stability test for prepared catalysts.

The stability tests were also conducted for as-synthesised materials using 10% ethanol and results are shown in Figure 5.17(b). All investigated catalysts showed good selectivity $>99\%$ throughout the reaction time. Similar to previous results, the activity of 3Cu/NMC-3 retained 93% even after 800 min. The results showed that the selectivity of as-synthesised materials was not sensitive to the presence of water content in the reaction feed. A decrease in activity was observed for 3Cu/NMC-1 and 3Cu/NMC-2.

Additionally, the stability test for 8Cu/NMC-3 and 8Cu/NMC-2 was performed at 260°C and the results are shown in Figure 5.18. 8Cu/NMC-3 and 8Cu/NMC-2 showed almost same activity until 100 min of reaction time. However, 8Cu/NMC-3 retained 75% of initial activity whereas 8Cu/NMC-2 retained 50% of its activity after 800 min. The high stability of 8Cu/NMC-3 is because of the well-dispersed small Cu nanoparticles and confinement of Cu nanoparticles in the ordered mesoporous carbon helping them become stable for the long-term reaction. The deactivation might have

emerged from sintering of very small Cu nanoparticles present in the catalysts and surface oxidation of active Cu nanoparticles.

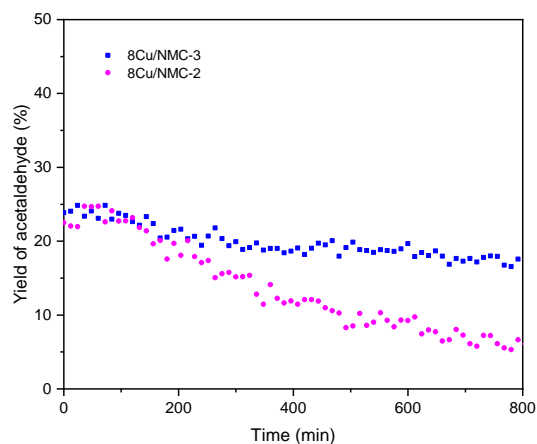


Figure 5.18: Stability test for 8Cu/NMC-2 and 8Cu/NMC-3.

The effect of GHSV on the performance of the catalysts was also analysed by changing the GHSV from 21250 h^{-1} to 26500 and 45450 h^{-1} with all other conditions remain unchanged. STY (site time yield), which is the measure of yield of acetaldehyde produced per amount of catalyst used in unit time, is used to analyse the catalytic performance. Figure 5.19 shows the effect of GHSV on the STY. The result shows that there is a direct relation between GHSV and STY with an increase in GHSV resulting in a higher STY and therefore an increased catalytic performance [78].

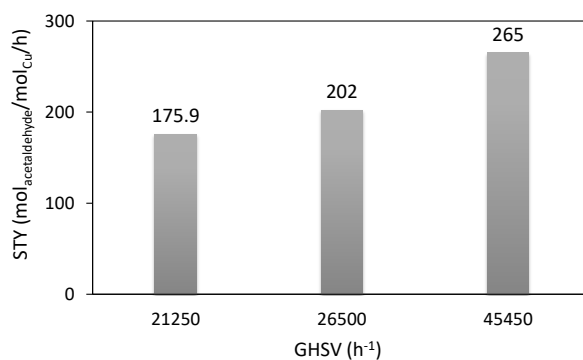


Figure 5.19: Effect of GHSV on STY.

To get insight into the deactivation of catalysts, the spent catalysts were characterised using TEM and XRD. Figure 5.20 shows the XRD of the investigated materials with 3 wt% Cu. All spent catalysts showed diffraction pattern of Cu(111) and Cu(200) plane and intensity of both peaks decreased in the order 3Cu/NMC-1 > 3Cu/NMC-2 > 3Cu/NMC-3. The 3Cu/NMC-1 showed very strong diffraction pattern of Cu(111) and Cu(200) planes. Additionally, 3Cu/NMC-1 exhibited a diffraction peak for Cu₂O(111) plane. The intense diffraction pattern of spent catalysts in comparison with fresh catalysts revealed the sintering or agglomeration of Cu nanoparticles under reaction condition [167, 183]. The appearance of Cu₂O can be correlated to the decrease in the activity under 10% ethanol reactant feed. This gave insight into the regeneration of the catalysts by re-reducing the spent catalyst.

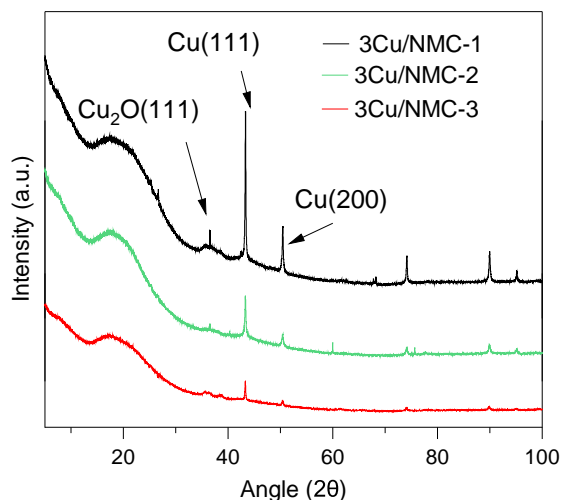


Figure 5.20: XRD pattern for spent catalysts after stability test.

Figure 5.21 shows the TEM images and particle size distribution of spent catalysts. The particle size distribution of the spent catalysts was measured by counting nearly 200 particles. The TEM images of investigated spent catalysts showed both small and large particles of Cu. The average particle size of 3Cu/NMC-1, 3Cu/NMC-2 and 3Cu/NMC-3 was approx. 15.4 nm, 13.2 and 6.9 nm, respectively. The particle size distribution of spent catalyst 3Cu/NMC-1 was broader in comparison with its fresh sample. The average size of nanoparticles of spent 3Cu/NMC-3 showed no significant difference in comparison with the fresh sample, which was 6.4 nm. This can be related to the high nitrogen doping in NMC-3 support.

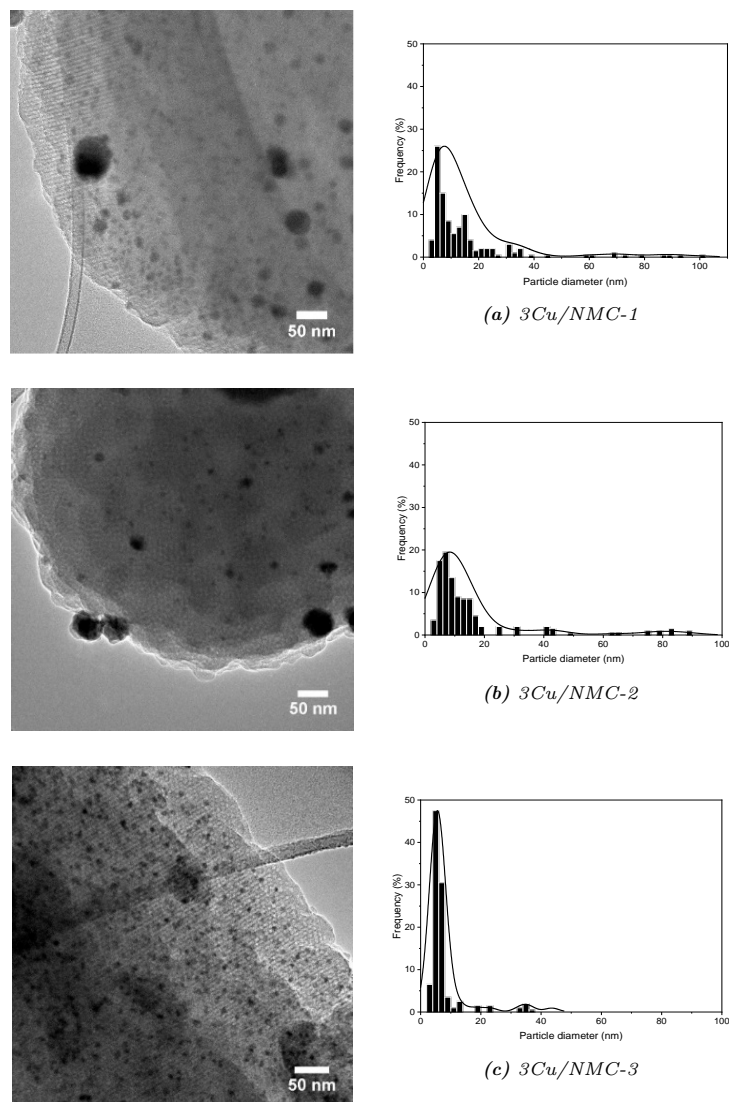


Figure 5.21: TEM images and particle size distribution of spent catalysts.

The catalysts 3Cu/NMC-1 and 3Cu/NMC-2 were tested for the reusability at 260 °C and same GHSV. Before testing, the materials were treated with H₂ at 450 °C inside the reactor for 90 min. Figure 5.22 shows the reusability of materials 3Cu/NMC-2 and 3Cu/NMC-1. 3Cu/NMC-1 retained 75% of the initial activity after the first cycle and 50% of the fresh catalyst activity in the second cycle. However,

the as-synthesised 3Cu/NMC-2 retained nearly 93% and 80% of the activity of its fresh catalytic test cycle in the first and second cycle, respectively. To sum up, both investigated materials showed a decrease in the activity on a continuous reaction stream with 3Cu/NMC-2 showing higher regenerative capability. 3Cu/NMC-3, when subjected to the regeneration test, showed almost 100% activity as that of its fresh catalytic test even after cycle 2.

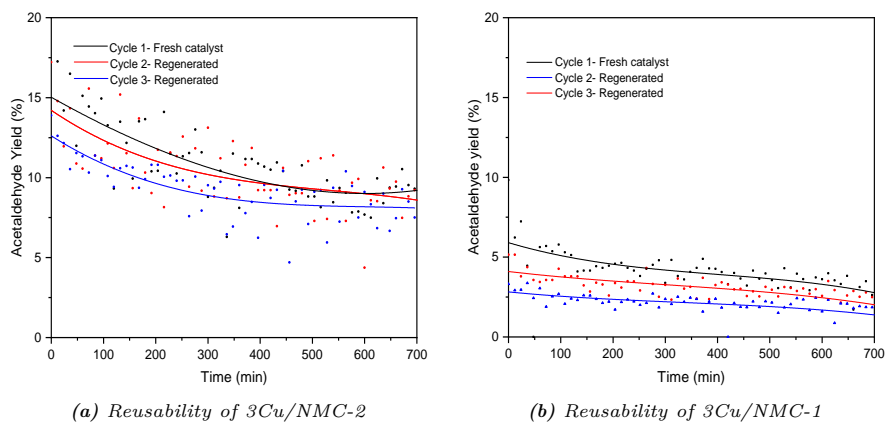


Figure 5.22: Reusability of prepared materials.

The role of nitrogen was more prominent in the catalytic activity of 3Cu/NMC-3 as it showed the highest yield of acetaldehyde and good stability. The influence

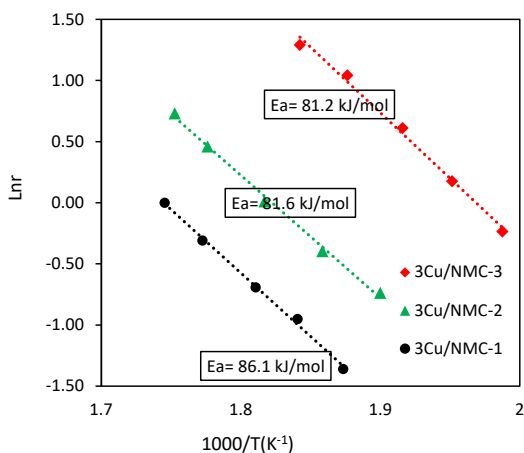


Figure 5.23: Arrhenius plot for synthesised catalysts.

of nitrogen in the activation energies of the catalyst was studied by Arrhenius plot. Figure 5.23 shows the Arrhenius plot of the investigated catalysts with 3 wt% Cu. The apparent activation energies were calculated from the slope of the relation between $1000/T(K^{-1})$ and $\text{Ln}r$, where $\text{Ln}r$ represents the natural logarithm of STY. The apparent activation energies were in the order 81.2, 81.6 and 86.1 kJ/mol for 3Cu/NMC-3, 3Cu/NMC-2 and 3Cu/NMC-1, respectively. With the activation energies not wide apart, it confirms that nitrogen has no significant effect on the rate-limiting step of the reaction.

To analyse the mechanism of the formation of acetaldehyde, in-situ DRIFTS was carried out. Figure 5.24 and Figure 5.25 shows the in-situ DRIFT spectra of 3Cu/NMC-3 and 3Cu/NMC-1. The DRIFT spectra were collected from temperature 50 to 350 °C. The catalysts were reduced in-situ at 450 °C before conducting in-situ DRIFTS studies. 3Cu/NMC-3 and 3Cu/NMC-1 were chosen for in situ-DRIFTS to study the effect of nitrogen in the mechanism of the formation of acetaldehyde. The study can provide information about the formation of species over the surface during the dehydrogenation of ethanol to acetaldehyde.

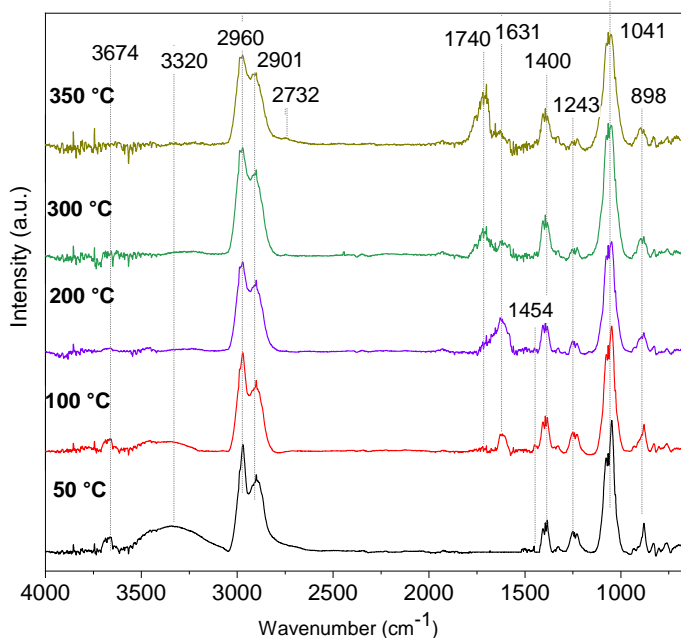


Figure 5.24: In-situ DRIFT spectra of 3Cu/NMC-3 for ethanol dehydrogenation.

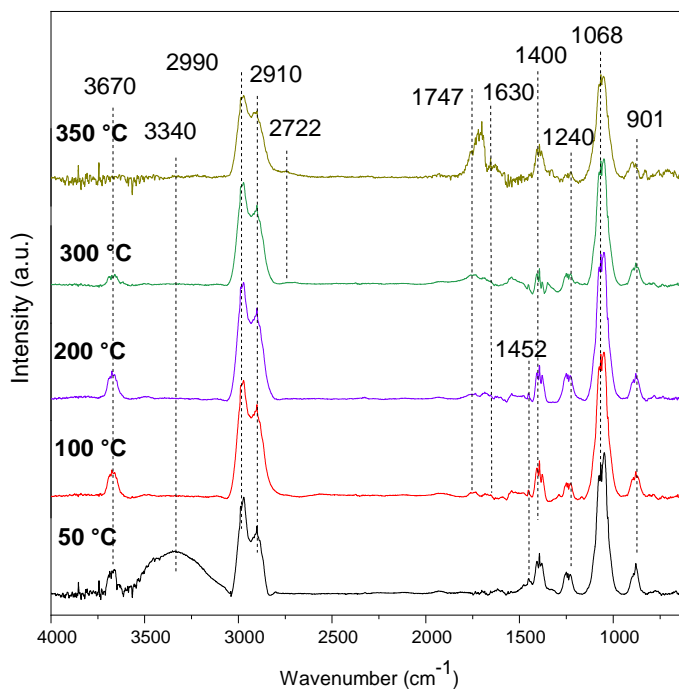


Figure 5.25: In-situ DRIFT spectra of 3Cu/NMC-1 for ethanol dehydrogenation.

Major observations from the in-situ DRIFT spectra are as follows.

- At 50 °C, both 3Cu/NMC-3 and 3Cu/NMC-1 showed major peaks at 3674 cm^{-1} and 3320 cm^{-1} corresponding to O—H stretching and 2960 cm^{-1} corresponding to C—H bond vibration of methyl asymmetric stretching. Additional peaks were also observed at 2901 cm^{-1} , 1400 cm^{-1} , 1243 cm^{-1} , 1041 cm^{-1} and 898 cm^{-1} corresponding to methylene asymmetric stretching, CH_3 bending, O—H bending, C—O stretching and C—C stretching, respectively [184–186].
- A temperature increase from 50 to 350 °C has resulted in a change in the intensity of certain peaks for both 3Cu/NMC-3 and 3Cu/NMC-1. For example, the peak intensity at 3674 cm^{-1} corresponding to adsorbed ethanol on the surface of catalyst and broad peak at 3320 cm^{-1} correlating to the stretching of hydrogen-bonded O—H group were both decreased. Additionally, the intensity of the peak at 1243 cm^{-1} is declined when the temperature is increased from 50 to 350 °C. This peak corresponds to the formation of hydroxyethyl (CH_3CHOH^*) by $\alpha\text{C—H}$ bond cleavage in the ethanol. The peak confirms the

formation of acetyl and ethoxy intermediate species in dehydrogenation [25, 184, 187].

- Formation of acyl intermediate at very low temperature is confirmed by the new peak at 1631 cm^{-1} at $100\text{ }^{\circ}\text{C}$ and $200\text{ }^{\circ}\text{C}$. Peak corresponding to $\text{C}=\text{O}$ stretching frequency of acetaldehyde started to appear at $200\text{ }^{\circ}\text{C}$ around 1740 cm^{-1} and becomes stronger as the temperature is increased. Furthermore, the formation of acetaldehyde is confirmed by the appearance of a new peak at $350\text{ }^{\circ}\text{C}$ around 2732 cm^{-1} .

In summary, in-situ DRIFT spectra provided an insight into the dehydrogenation reaction mechanism and confirmed that both catalysts behaved identically irrespective of nitrogen content with similar intermediate products.

5.4 Modification to mesoporous carbon for improved catalytic performance

As described in chapter 2, the surface area and total pore volume of porous support are important parameters in catalysis by supported nanoparticles and have a direct impact on the catalytic activity. Therefore, it is vital to investigate the factors contributing to the surface area of mesoporous carbon during the synthesis stage. The synthesis of mesoporous carbon involves two major processes, i.e, polymerisation and calcination. This section describes the effect of polymerisation and calcination temperature on the structural properties of mesoporous carbon like surface area, pore width and total pore volume and hence the catalytic activity. NMC-2 is chosen for the analysis. The materials were prepared with two different polymerisation temperatures 80 and $95\text{ }^{\circ}\text{C}$ followed by calcination at 600 , 700 , 800 and $900\text{ }^{\circ}\text{C}$. The as-synthesised materials were impregnated with $3\text{ wt}\%$ Cu and reduced at $450\text{ }^{\circ}\text{C}$ under the flow of H_2 . The synthesised materials were analysed through various characterisation techniques before it was tested for the dehydrogenation of ethanol to acetaldehyde. For the ease of distinguishing various mesoporous carbon materials synthesised, the terminology NMC-2-x/y is used, where x is the polymerisation temperature whereas y is the calcination temperature. For eg: NMC-2-80/800 represents NMC-2 synthesised with a polymerisation temperature of $80\text{ }^{\circ}\text{C}$ and calcined at $800\text{ }^{\circ}\text{C}$. In total, 8 materials were synthesised to analyse the physical properties.

5.4.1 Characterisation results

All the samples were characterised using various techniques including nitrogen physisorption, XPS, SEM and TEM. The equipment used and conditions applied for different analysis are specified in Chapter 3. This section describes the results obtained from various characterisation techniques.

5.4.1.1 Nitrogen physisorption

Table 5.4 shows the nitrogen physisorption data of synthesised materials. The polymer prepared with different polymerisation and calcination temperature showed different BET surface area. For instance, the surface area of NMC-2-80 increased from 455 to 785 m²/g when calcination temperature was changed from 600 to 900 °C, whereas the surface area of NMC-2-x/600 changed from 455 to 602 m²/g when polymerisation temperature was changed from 80 to 95 °C and calcined at 900 °C. Additionally, the total pore volume of the NMC-2-80 calcined at different temperature showed a gradual increase while NMC-2-95 calcined at different temperature showed no direct correlation between temperature and total pore volume. The pore size of the investigated materials showed no significant change with polymerisation and calcination temperature. The isotherm of all materials showed a typical H4 hysteresis loop, which is often associated with micro-mesoporous carbon.

Table 5.4: Nitrogen physisorption data for prepared materials.

Samples	S_{BET}^a m ² g ⁻¹	V_{micro}^b cm ³ g ⁻¹	V_{total}^c cm ³ g ⁻¹
NMC-2-80/600	455	0.130	0.257
NMC-2-80/700	626	0.199	0.345
NMC-2-80/800	695	0.223	0.386
NMC-2-80/900	785	0.260	0.423
NMC-2-95/600	602	0.177	0.333
NMC-2-95/700	596	0.182	0.320
NMC-2-95/800	712	0.219	0.385
NMC-2-95/900	790	0.217	0.385

^a S_{BET} calculated by the BET method.

^b V_{micro} calculated by the t -plot method.

^c V_{total} determined from the isotherm adsorption branch at around $p/p^0 = 0.95$.

5.4.1.2 XPS

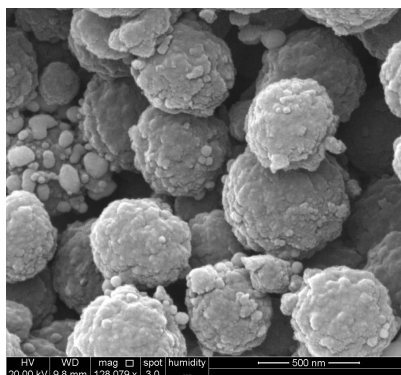
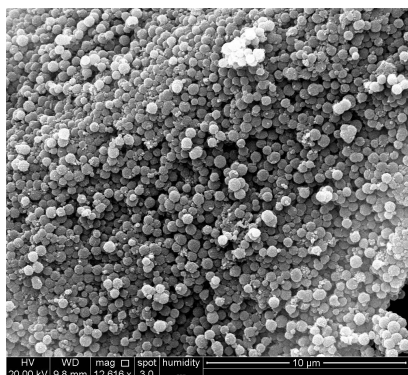
The surface nitrogen content was analysed using XPS method. Table 5.5 gives the XPS data of NMC-2 synthesised at different polymerisation and calcination temperatures. For the mesoporous carbon polymerised at 600 °C, NMC-2-80/600 showed the highest nitrogen content. As calcination temperature increased, the nitrogen content also decreased. In the case of sample polymerised at 95 °C, NMC-2-95/600 showed the highest nitrogen content with a decrease in nitrogen content, as the calcination temperature increased. Among all investigated materials, the sample NMC-2-95/600 calcined at 600 °C and polymerised at 95 °C showed the highest nitrogen content.

Table 5.5: XPS data for prepared materials.

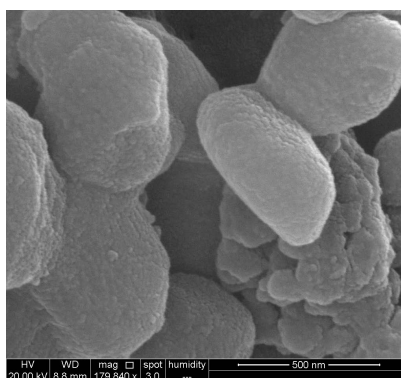
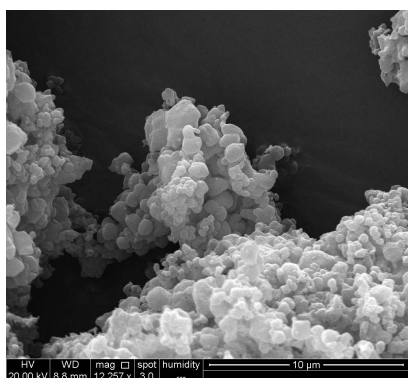
Samples	Nitrogen %	Carbon %	Oxygen %
NMC-2-80/600	1.80	94.30	3.90
NMC-2-80/700	1.35	90.72	6.59
NMC-2-80/800	1.10	94.40	3.85
NMC-2-80/900	0.42	96.38	3.20
NMC-2-95/600	3.12	89.38	7.50
NMC-2-95/700	2.44	90.05	7.50
NMC-2-95/800	1.88	89.47	8.64
NMC-2-95/900	1.14	89.96	8.90

5.4.1.3 SEM

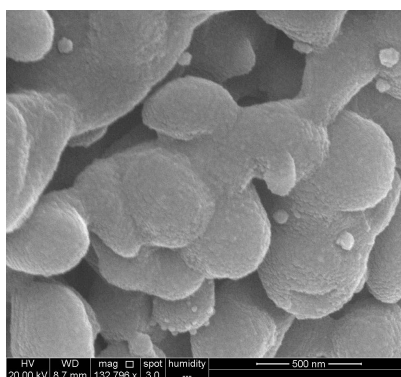
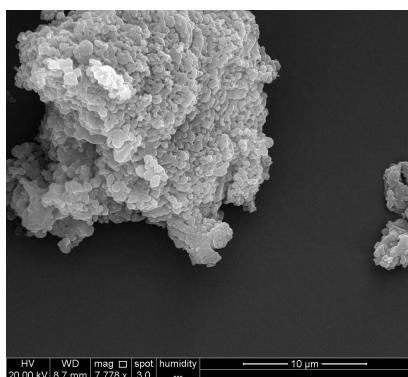
Figure 5.26(a) shows SEM images of NMC-2-80 synthesised at a calcination temperature of 800 °C. The images show discrete spherical shapes with an average size of 400 nm. The material showed uniform distribution in SEM image and size and shape did not change as compared with the SEM image of NMC-2 calcined at 600 °C (Figure 5.7). Figure 5.26(b-c) shows the SEM images of NMC-2-95 synthesised at calcination temperature 800 and 900 °C. The SEM images of NMC-2-95/800 showed neither spherical particles nor discrete structures. The images seemed to be the agglomeration of spherical carbon structures.



(a) NMC-2-80/800



(b) NMC-2-95/800



(c) NMC-2-95/900

Figure 5.26: SEM images of prepared materials.

5.4.1.4 TEM

Figure 5.27 shows the TEM images of NMC-2-80 and NMC-2-95 and loaded with 3 wt% copper which are calcined at 800 and 900 °C. The average size of nanoparticles was in the range of 12 - 17 nm and 16 - 25 nm for 3Cu/NMC-2-80/800 and 3Cu/NMC-2-80/900, respectively, whereas the average size of nanoparticles in 3Cu/NMC-2-95/800 and 3Cu/NMC-2-95/900 was in the range of 5 - 12 nm and 5 - 10 nm, respectively. All investigated samples showed a mixture of both small and large particles of Cu in the TEM image. The size of large particles was up to 100 nm in certain samples. Generally, the sample prepared at higher polymerisation temperature showed comparatively smaller nanoparticle distribution.

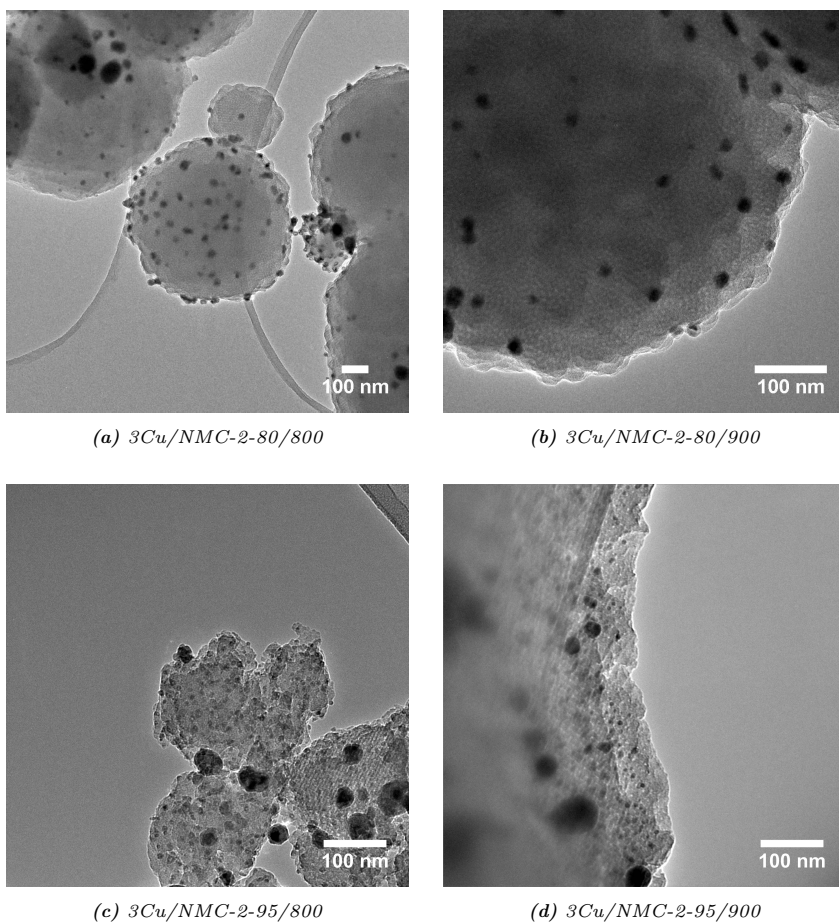


Figure 5.27: TEM images of prepared materials.

5.4.2 Catalytic activity

The catalytic performance of all synthesised samples was tested for the dehydrogenation of ethanol to acetaldehyde using 10% ethanol feed with GHSV 21250 h^{-1} . Figure 5.28 shows the yield of acetaldehyde as a function of temperature for the as-synthesised catalysts 3Cu/NMC-2-80 with different calcination temperature. All investigated materials showed selectivity $> 99\%$ towards acetaldehyde. As expected, the temperature had a direct impact on the yield and therefore the yield of acetaldehyde increased as the temperature increased for all investigated materials. 3Cu/NMC-2-80/700 showed the highest acetaldehyde yield (56%) at 350 °C whereas 3Cu/NMC-2-80/900 resulted in the least yield acetaldehyde yield (20%). At 350 °C, acetaldehyde yield followed the order 3Cu/NMC-2-80/700 $>$ 3Cu/NMC-2-80/600 $>$ 3Cu/NMC-2-80/800 $>$ 3Cu/NMC-2-80/900.

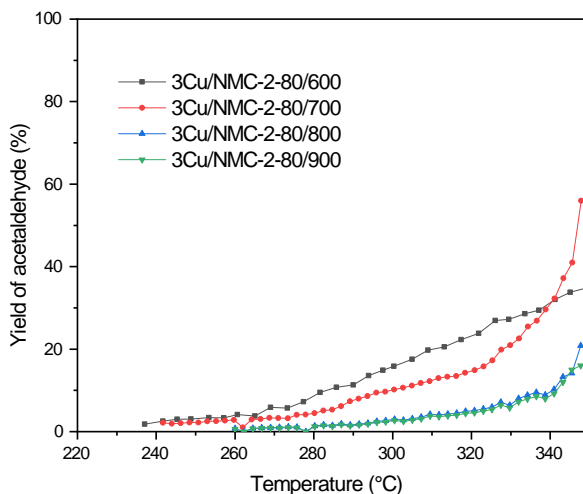


Figure 5.28: Catalytic activity of 3Cu/NMC-2-80 calcined at different temperature.

Although the conversion of ethanol was higher using 3Cu/NMC-2-80/700 as compared to 3Cu/NMC-2-80/600, the conversion with 3Cu/NMC-2-80/700 decreased rapidly as the temperature decreased whereas the conversion by Cu/NMC-2-80/600 was more stable and showed the least deactivation of catalysts. In general, the conversion of acetaldehyde yield showed no direct relations with calcination temperature. Additionally, of all investigated catalysts, 3Cu/NMC-2-80/800 showed the highest BET surface area with the size of Cu nanoparticles randomly distributed. This makes it unclear to find the link between the physical characteristics of

ordered mesoporous carbon support and catalytic performance. However, the size of nanoparticles in 3Cu/NMC-2-80/600 was more uniform with narrow distribution and higher nitrogen content. These factors help nanoparticles in 3Cu/NMC-2-80/600 to be stabilised resulting in a more stable catalyst with good acetaldehyde yield.

Figure 5.29 shows the acetaldehyde yield as a function of temperature for the samples 3Cu/NMC-2-95 with different calcination temperature. The acetaldehyde yield at 350 °C followed the order 3Cu/NMC-2-95/800 > 3Cu/NMC-2-80/900 > 3Cu/NMC-2-80/700. The yield of acetaldehyde was highest for 3Cu/NMC-2-95/800 ($\approx 89\%$). In general, the acetaldehyde yield of the catalyst polymerised at 95 °C was higher in comparison to the materials polymerised at 80 °C. The nitrogen physisorption data in Table 5.4 clearly showed a high BET surface area for all materials polymerised at 95 °C as compared to the materials polymerised at 80 °C with an exception for 3Cu/NMC-2-95/700. The sample 3Cu/NMC-2-80/600 and 3Cu/NMC-2-95/800 had the highest peak of pyridinic-N which stabilised the Cu nanoparticles. Additionally, the nanoparticles of 3Cu/NMC-2-95/800 and 3Cu/NMC-2-95/900 were more uniform and smaller. It is likely that these factors led to the highest catalytic activity of 3Cu/NMC-2-80/600 and 3Cu/NMC-95/800.

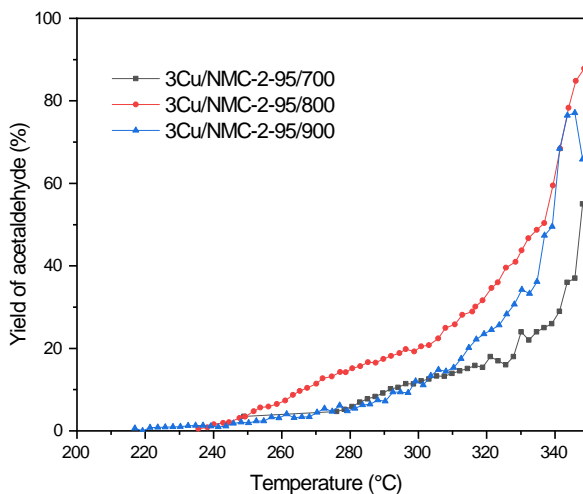


Figure 5.29: Catalytic activity of 3Cu/NMC-2-95 calcined at different temperature.

5.5 Summary

The work reports an efficient and highly selective heterogeneous catalyst comprised of Cu metal nanoparticles supported on nitrogen-doped ordered mesoporous carbon for the selective conversion of ethanol to acetaldehyde via dehydrogenation. Although all the synthesised catalysts showed high selectivity towards acetaldehyde, copper supported on nitrogen-rich mesoporous carbon, 3Cu/NMC-3, showed the highest acetaldehyde yield as compared to other synthesised materials. It was found that nitrogen plays a crucial role in the stabilisation of nanoparticles. Additionally, results have confirmed that the presence of water in reactant feed does not affect the catalytic activity of as-synthesised catalysts thereby extending the scope of this catalytic system for commercial purpose with biomass-derived bioethanol. It was also observed that varying the polymerisation and calcination temperature on the synthesis process of nitrogen-doped ordered mesoporous carbon has a direct impact on the structural properties of materials. This, in turn, affects the adsorption capability and the performance of the catalysts in the dehydrogenation reaction. However, a detailed investigation is required for finding the influence of synthesis temperature on the dispersion of Cu nanoparticles.

Considering the future need of biomass-derived chemicals, the heterogeneous catalyst with Cu supported on nitrogen-doped ordered mesoporous carbon is a potential candidate for large scale production of acetaldehyde from bioethanol.

CHAPTER 6

One-step Conversion of Ethanol to Butadiene

1,3-Butadiene is an important organic compound used as a chemical intermediate and in the production of synthetic rubber. This chapter describes a method to synthesise 1,3-butadiene from ethanol. The reaction utilises heterogeneous catalyst comprising Zn containing zeolite. The chapter addresses synthesis methodology, characterisation, catalytic test results and identifies the optimum catalyst for the conversion of ethanol to butadiene.

6.1 Introduction

1,3-Butadiene or butadiene, with the chemical formula $(\text{CH}_2=\text{CH})_2$, is an organic compound used as a monomer to produce different types of polymers. It is used in the production of various synthetic rubber such as styrene-butadiene rubber (SBR), polybutadiene rubber (BR) and acrylonitrile butadiene rubber (ABR). Among these, SBR is widely used in the manufacture of tyres in the automobile industry owing to its good abrasion resistance and improved ageing stability. Butadiene is also used as a chemical intermediate in the production of industrial chemicals [6, 188–190]. With the growing demand for vehicles like electric cars growing over the coming years, the demand for the butadiene is increasing globally [191]. The global demand for butadiene is close to 3.4 million tonnes annually with an incremental annual growth of 4.1% [192].

Currently, 95% of butadiene is produced as a side product in ethylene production from steam crackers. Butadiene produced from this process is purified using heavier fossil feedstock such as naphtha and gas oil [193]. An alternative method to synthesise butadiene from renewable feedstock-based chemicals is the conversion of ethanol

to butadiene [194, 195]. As described in Chapter 1, bioethanol produced through the fermentation process of biomass products used as a starting material for the synthesis of butadiene [2, 52, 194, 196, 197]. Although the feasibility of the ethanol to butadiene conversion route has been studied and proven a long time ago, significant improvements in both engineering and catalytic systems are vital to attain high butadiene yield and productivity and to activate the commercial implementation of the ethanol-butadiene conversion process [6, 198].

The pathway for the conversion of ethanol to butadiene has been studied extensively in the past for several decades. The conversion process can be broadly classified into one-step and two-step process [164, 199]. Both reaction processes involve a series of reactions via multiple pathways with different products ultimately leading to butadiene. The two-step process proposed by Ostromyslensky involves butadiene production through a catalytic route from a mixture of ethanol and acetaldehyde over alumina or clay catalysts at 440 - 460 °C [200]. Lebedev proposed a one-step process from ethanol alone as the starting material with the aid of a catalyst [28, 201–203]. The reaction process proposed by Lebedev is shown in Figure 6.1. Lebedev proposed a catalytic system comprised of a mixture of zinc oxide and alumina.

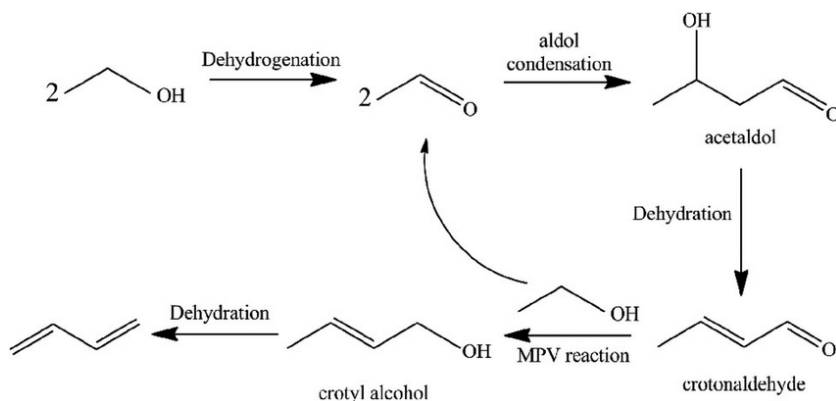


Figure 6.1: Conversion of ethanol to butadiene as proposed by Lebedev [186].

Over the years, several catalysts were proposed for the one-step process [158, 204]. Natta and Rigamonti reported a catalyst comprising of $\text{MgO-Al}_2\text{O}_3$ rich in magnesia, whereas Bhattacharyya et al. proposed alumina-based catalysts containing mono-, binary and ternary oxides [205, 206]. The proposed zinc-alumina catalyst with a small percentage of potassium oxide, silica and magnesia reported 34% butadiene

yield and 80% selectivity at 420 °C. At the same time, catalysts with magnesia on silica were also reported in several studies to show high catalytic performance [207]. However, most of these catalysts required high reaction temperature resulting in the formation of more side-products.

Recent researches on catalysts for the direct conversion of ethanol to butadiene have been predominantly focusing on the mixed metal oxide catalysts [136, 186, 194, 199, 208]. The catalytic system composed of acid, basic, or redox or a mixture of one or more properties. Even though the specific mechanism of the reaction is unclear, redox or basic site catalyses the dehydrogenation of ethanol to acetaldehyde, which is the first intermediate in the reaction. At the same time, the acidic or basic site participates in the dehydration or condensation reaction, which results in the formation of unwanted side products from ethanol like ethylene, while these sites are essential for aldol condensation of acetaldehyde to crotonaldehyde and further. Due to the complexity of reaction, a paradisaical balance between acidic, basic, redox and structural parameters of catalysts is required for the selective conversion of ethanol to butadiene [158, 186, 188, 209].

Zn is one of the most investigated metals with Zn-Zr, Zn-Y, Zn-Ta or supported on other metal oxides for the conversion of ethanol to butadiene. Zn is also used as a catalytic promoter to tune the redox and/or Lewis acidic properties of parent catalyst and has shown improved dehydrogenation properties and/or butadiene yield. The ethanol to butadiene mechanism reported in various literature had a varying rate-limiting step based on the catalytic system used. Therefore the focus is to optimise the catalytic system for high butadiene yield by tuning between dehydrogenation and dehydration. As described in Chapter 2, the mesoporous system containing metallosilicates can prevent the catalyst from becoming deactivated due to the formation of coke on the catalytic surface and can provide a higher conversion of ethanol to butadiene due to improved mass transfer. The presence of mesopores can facilitate the dispersion of metal nanoparticles due to the increased surface area.

As part of this Ph.D. work, Zn supported on different morphologies of HZSM-5 zeolite were used for the direct conversion of ethanol to butadiene. Four types of HZSM-5 zeolite support were synthesised by altering the pore size. i.e, conventional HZSM-5 denoted as HZSM-5, desilicated HZSM-5 denoted as DesHZSM-5, carbon-template assisted mesoporous HZSM-5 denoted as MesoHZSM-5 and surfactant F-127 assisted mesoporous HZSM-5 denoted as F127-HZSM-5. Moreover, Si/Al ratio for the HZSM-5 was varied to find the optimum catalyst.

6.2 Experimental section

6.2.1 Materials

Materials used for the synthesis of HZSM-5 are listed in Section 2.2.4.1. Additionally, zinc nitrate hexahydrate ($\text{Zn}(\text{NO}_3)_2 \cdot 6\text{H}_2\text{O}$, $\geq 98\%$) was used.

6.2.2 Synthesis of materials

This section describes the synthesis process of various zeolites and catalysts prepared for the ethanol to butadiene conversion reaction.

6.2.2.1 Synthesis of different zeolites

Conventional HZSM-5 zeolite with different Si/Al ratio was prepared by following the method described in Section 2.2.4.2. The Si/Al ratio was varied by changing the amount of NaAlO_2 . For instance, 0.022 g of NaAlO_2 gives Si/Al ratio = 150. Carbon templated mesoporous HZSM-5 zeolite with Si/Al = 150 was prepared by following the method described in Section 2.2.4.3. Desilicated HZSM-5 (DesHZSM-5) was synthesised using the method described in Section 2.2.4.4, whereas F-127 assisted soft template HZSM-5 was synthesised using the procedure described in Section 2.2.4.5.

6.2.2.2 Synthesis of Zn supported on HZSM-5 support

Zeolite (0.99 g) was vacuum dried at 50 °C overnight. An aqueous precursor solution of $\text{Zn}(\text{NO}_3)_2 \cdot 6\text{H}_2\text{O}$ (0.045 g) was prepared for the incipient wetness impregnation of Zn. This precursor solution was added dropwise over the zeolite and mixed thoroughly after the addition of each drops. The resulting materials were dried at room temperature overnight and calcined at 500 °C for 2 h with a heating ramp 5 °C/min.

6.2.3 Characterisation

All the samples were characterized using various techniques including XRD, nitrogen physisorption, TEM, ICP-OES, XPS and ammonia TPD. The equipment used and conditions applied for different analysis are specified in Chapter 3.

6.2.4 Gas-phase conversion of bioethanol to butadiene

The gas-phase direct conversion of bioethanol (10% ethanol + 90% water) to 1,3-butadiene was conducted in a continuous fixed bed reactor. In a typical reaction, 100 mg of fractionated catalyst (185-355 μm) was loaded in a quartz reactor with a 3 mm diameter. Bioethanol was pumped into an evaporator at 135 $^{\circ}\text{C}$ and mixed with nitrogen (50 ml/min) with a weight hourly space velocity (WHSV) of 2.36 g ethanol/g catalyst /h. The gas mixture was passed through the fixed catalyst bed containing 100 mg catalyst. The product mixture was analysed using an online GC-FID on a regular interval. The product mixture was collected externally and injected in GC-MS to identify all the unknown products. A simplified diagram of the reactor set up is given in Figure 6.2. All catalysts were tested at a temperature of 320 $^{\circ}\text{C}$ and atmospheric pressure. The set up was controlled by a pre-programmed LabVIEW script.

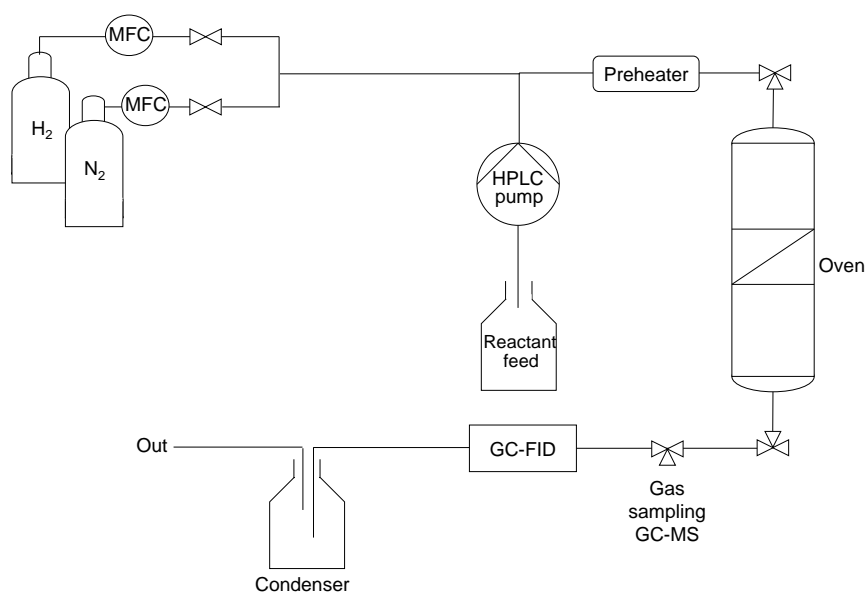


Figure 6.2: Schematic illustration of reactor flow setup.

6.3 Results and discussions

This section describes the results obtained through various characterisation techniques for as-synthesised materials. This is followed by the test for performance of catalysts in the butadiene synthesis from bioethanol. In total, seven different catalysts were considered for investigation. i.e, 5%Zn/HZSM-5 with Si/Al ratio 100, 150, 200 and 250, 5%Zn/MesoHZSM-5 with Si/Al ratio 150, 5%Zn/DesHZSM-5 with Si/Al ratio 150 and 5%Zn/F127-HZSM-5 with Si/Al ratio 150.

6.3.1 Characterisation results

6.3.1.1 XRD

Figure 6.3 shows the XRD pattern of 5 wt% Zn loaded on different zeolite supports. The XRD patterns of investigated materials were similar and showed a characteristic pattern of MFI zeolites [58]. In addition, two diffraction peaks at $2\theta = 31.8^\circ$ and 36.3° were identified for four material as shown in Figure 6.3. The appearance of this weak diffraction peaks could be possibly due to the presence of ZnO particles in the catalysts.

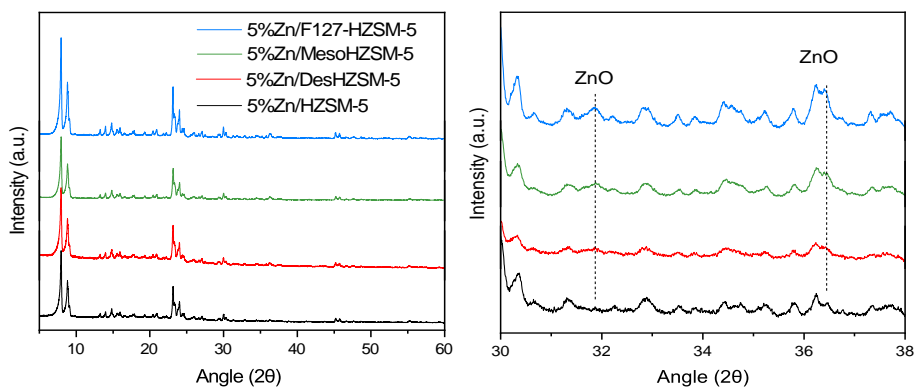


Figure 6.3: XRD pattern of investigated materials.

6.3.1.2 Nitrogen physisorption

Figure 6.4 shows the nitrogen physisorption isotherm of all investigated zeolite supports before the addition of Zn. The isotherm of HZSM-5, DesHZSM-5 and F127-

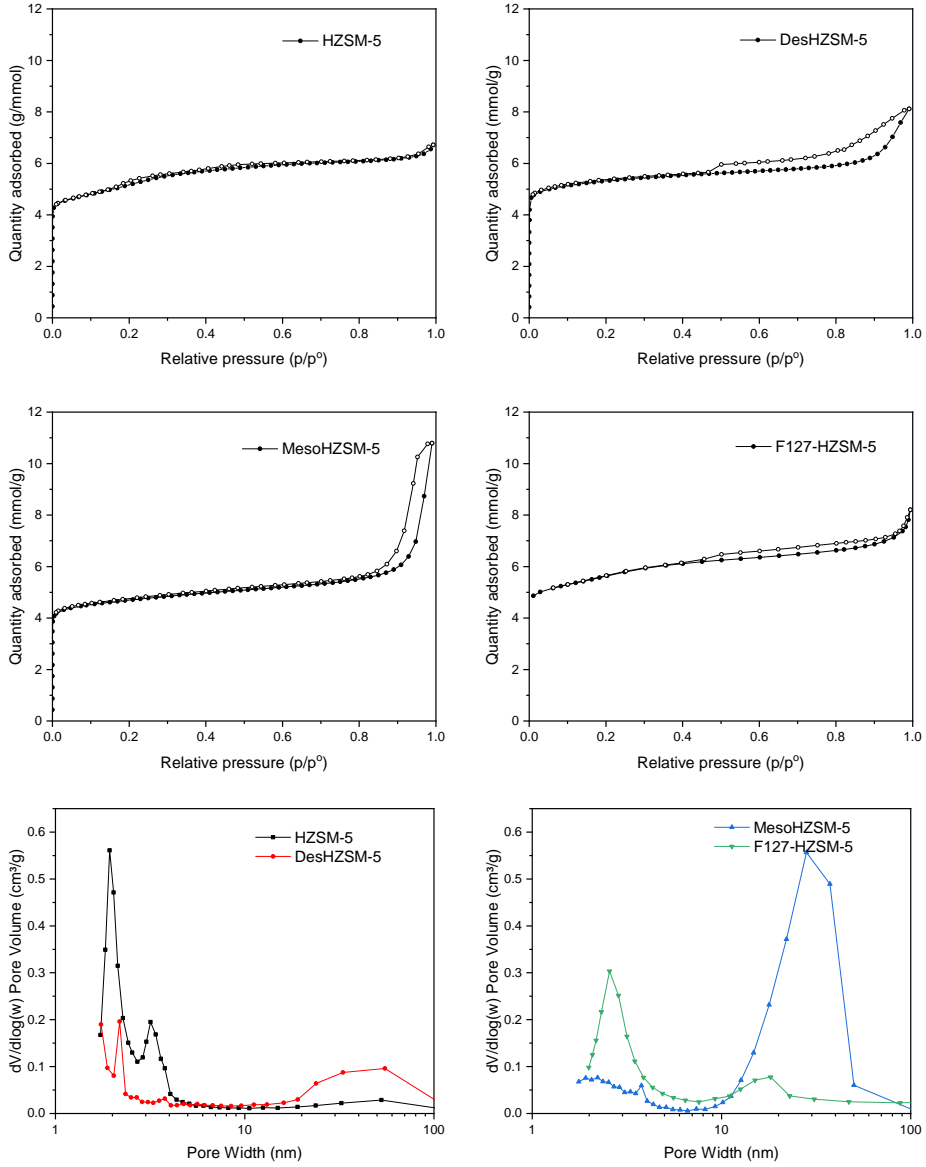


Figure 6.4: Nitrogen physisorption analysis of prepared materials.

HZSM-5 were a type I isotherm, which originate from the microporous materials. Moreover, DesHZSM-5 and F127-HZSM-5 showed an H4 hysteresis loop that closes around $p/p^0 = 0.42$, which can be attributed to the internal voids present in the

system [33, 64]. The isotherm of MesoHZSM-5 showed a type IV isotherm where the hysteresis loop closes around $p/p^0 = 0.8$. This type of isotherm is typical for the mesoporous zeolites with narrow pore size distribution [74]. The pore width distribution of the zeolites supports from the desorption branch of isotherm were also shown in Figure 6.4. The DesHZSM-5 showed the broad pore size distribution of 20 - 100 as compared to HZSM-5. The pore size distribution of MesoHZSM-5 and F127-HZSM-5 was 10 - 100 nm and 10 - 20 nm, respectively. All materials except HZSM-5 showed pores in the mesoporous region.

Additionally, Table 6.1 gives the total pore volume, BET surface area and micropore volume derived from t-plot. The DesHZSM-5 showed higher total pore volume compared to HZSM-5. F127-HZSM-5 showed the highest BET surface area and HZSM-5 showed the lowest total surface area. The materials F-127-HZSM-5 has larger BET surface in comparison to other materials. However, the total pore volume of MesoHZSM-5 was higher than F127-HZSM-5.

Table 6.1: Nitrogen physisorption data.

Material	S_{BET}^a m^2g^{-1}	V_{micro}^b cm^3g^{-1}	V_{total}^c cm^3g^{-1}
HZSM-5	302	0.112	0.211
DesHZSM-5	374	0.094	0.233
MesoHZSM-5	392	0.12	0.287
F127-HZSM-5	420	0.12	0.243

^a S_{BET} calculated by the BET method.

^b V_{micro} calculated by the t-plot method.

^c V_{total} determined from the isotherm adsorption branch at around $p/p^0 = 0.95$.

6.3.1.3 TEM

The TEM images of synthesised catalysts are shown in Figure 6.5. The zeolite supports HZSM-5 and DesHZSM-5 with 5%Zn showed similar crystals with the crystal size in the range 200 to 300 nm. 5%Zn/MesoHZSM-5 showed the largest crystals with a size 2 - 2.5 μm . The support F127-HZSM-5 showed irregularly sized crystals with size ranging from 400 nm to 1.2 μm . The irregularly shaped mesopores were observed for all materials except HZSM-5. Additionally, TEM images of catalysts showed no

evidence of Zn nanoparticles. This is probably due to the small size of Zn particles [70, 210].

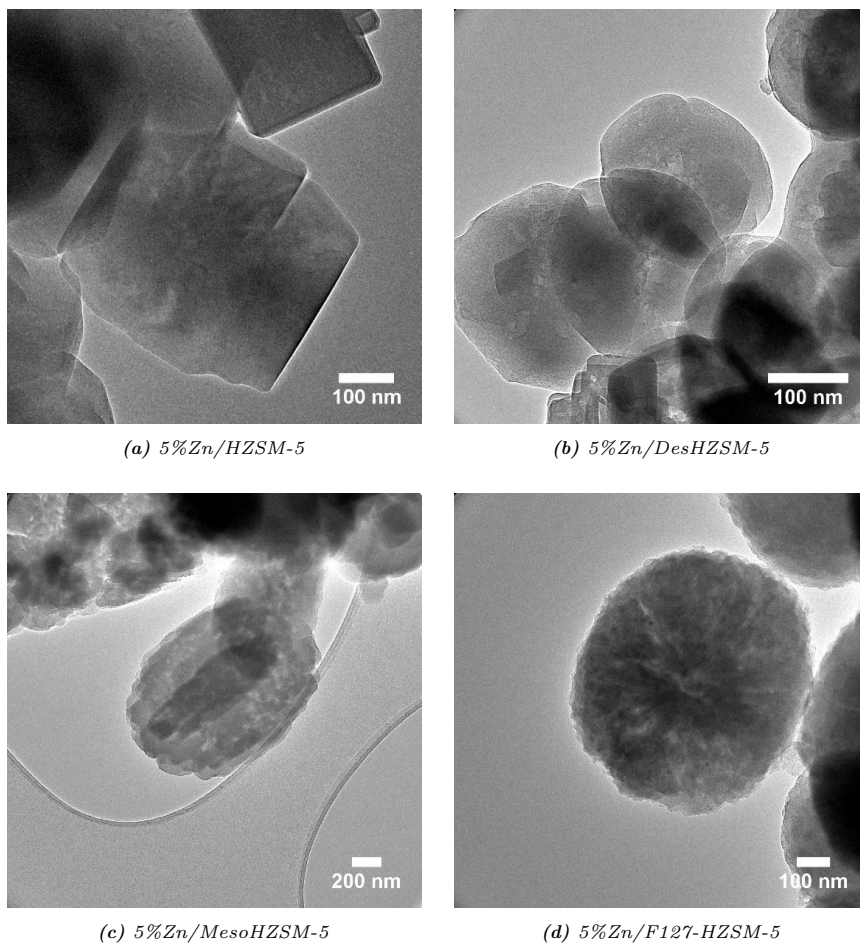


Figure 6.5: TEM images of prepared materials.

6.3.1.4 XPS

All catalysts (with 5% Zn) showed zinc oxide photopeaks in XPS as shown in Figure 6.6. The Zn2p showed two peaks in the binding energy region 1024.5 and 1047.1 eV for all catalysts. The binding energy of bulk ZnO usually appears in the region 1022.1 and 1045.2 eV. The binding energy of the four catalysts showed a shift of

2 eV as compared to bulk ZnO, which is possibly due to the Si-O-Zn bond formation [209].

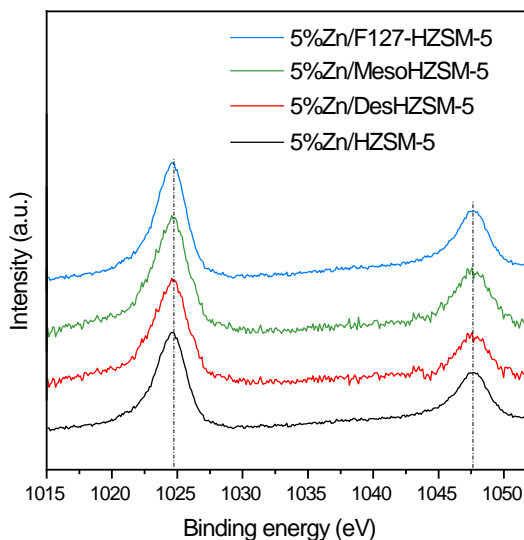


Figure 6.6: XPS spectra of synthesised materials.

6.3.1.5 NH_3 -TPD

Table 6.2 gives the data of NH_3 -TPD for different catalysts and zeolites supports. All investigated materials showed two distinct peaks in the NH_3 -TPD. The TPD peaks were classified as l (low temperature) and h (high temperature) peaks, with l peak appearing in the temperature range 160 -171 °C and h peak appearing in the range 360 – 368 °C. It was noticed that the strength of weak acid increased whereas the intensity of strong acid decreased after the addition of Zn to the zeolites support. It is evident from the literature that Zn species form a bond with zeolite support resulting in the coordination of Zn^{2+} species to the zeolites support [209, 211]. The low-temperature peak (l) can be considered as Lewis acid peak in the catalysts and therefore the addition of Zn to zeolite possibly form Lewis acid sites in the catalysts [53, 212]. Among different materials, 5%Zn/DesHZSM-5 had the highest density of weak acid sites and strong acid sites whereas 5%Zn/F127-HZSM-5 had the lowest density of weak acid sites.

Table 6.2: NH_3 -TPD data for synthesised materials.

Materials	Acidic strength	
	strong ^a	weak ^b
HZSM-5	0.029	0.018
5%Zn/HZSM-5	0.017	0.071
DesHZSM-5	0.034	0.027
5%Zn/DesHZSM-5	0.019	0.086
MesoHZSM-5	0.031	0.020
5%Zn/MesoHZSM-5	0.017	0.076
F127-HZSM-5	0.041	0.025
5%Zn/F127-HZSM-5	0.021	0.0680

^a Temperature range: 160 - 170 °C.^b Temperature range: 360 - 368 °C.

6.3.2 Catalytic activity

The performance of all synthesised catalysts was tested for the conversion of ethanol to butadiene. The reaction was carried out at a temperature 320 °C for 20 h of time on stream (TOS) using bioethanol (10% ethanol + 90% water) system at 1 bar with WHSV = 2.36 h⁻¹. The catalytic activity of HZSM-5 loaded with 5% Zn (5%Zn/HZSM-5) were compared for different Si/Al ratios. i.e, Si/Al = 100, 150, 200, 250. Figure 6.7 shows the conversion of ethanol and selectivity of butadiene for investigated catalysts. Among all catalysts tested, 5%Zn/HZSM-5 with Si/Al = 100 showed the highest conversion whereas 5%Zn/HZSM-5 with Si/Al = 200 showed the highest selectivity towards butadiene.

With the acidic strength of 5%Zn/HZSM-5 increased, the conversion of ethanol increased and followed the order Si/Al = 100 > 150 > 200 > 250. However, the selectivity of butadiene followed the reverse order, i.e, Si/Al = 250 > 200 > 150 > 100. In addition to butadiene, by-products such as ethylene, diethyl ether (DEE), acetaldehyde and crotonaldehyde were also formed in the reaction. The highest butadiene yield achieved with the catalyst having Si/Al = 150 is possibly due to a balance between redox site, Lewis and Brønsted acidic strength [186]. HZSM-5 with Si/Al = 100 having the highest acidic strength favoured the formation of dehydration products ethylene and diethyl ether whereas HZSM-5 zeolite with higher Si/Al favoured the dehydrogenation step for the formation of acetaldehyde, which is

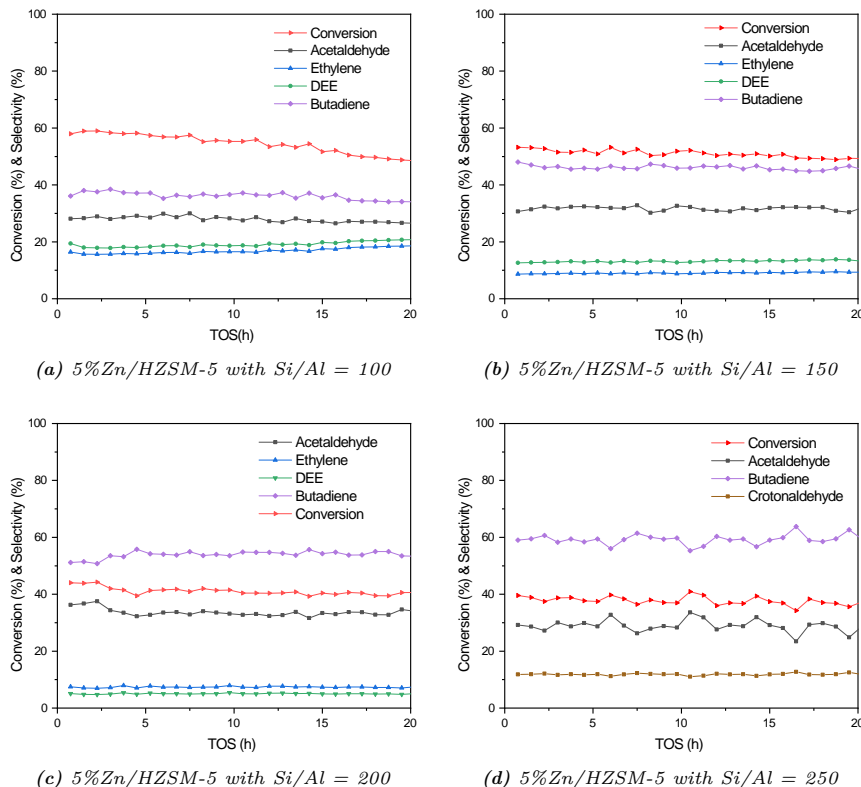


Figure 6.7: Catalytic performance of 5%/HZSM-5 with different Si/Al ratios at 320 °C and WHSV = 2.36 h⁻¹.

the rate-limiting step in the ethanol to butadiene reaction [213, 214].

Figure 6.8 shows the butadiene yield over various Si/Al ratio of 5%Zn/HZSM-5 for 20 h of TOS. Amongst four HZSM-5, Si/Al = 100 showed the least stability over time with butadiene yield decreased from 22% to 16% after 20 h of TOS. The butadiene yield followed the order of Si/Al = 150 > 200 = 250 > 100. Based on the results obtained, zeolite HZSM-5 (Si/Al = 150) with different morphology such as DesHZSM-5, MesoHZSM-5 and F127-HZSM-5 were tested for ethanol to butadiene reaction.

The role of the Brønsted acidic group was studied by carrying out the reaction under similar conditions using 5%Zn/NaHZSM5 and 5%Zn/Si1 (Si/Al = infinity). 5%Zn/NaHZSM-5 is the product formed just before the ion exchange in the catalytic synthesis procedure of 5%Zn/HZSM-5. The results are shown in Figure 6.9.

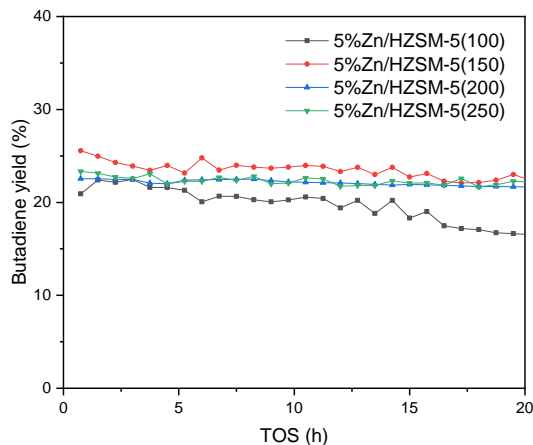


Figure 6.8: Butadiene yield for 5%Zn/HZSM-5 with different Si/Al ratio.

The catalyst 5%Zn/Si1 showed 9% conversion of ethanol and 100% selectivity for acetaldehyde with no traces of butadiene. This confirms the explanation made in the introduction, i.e, the conversion of ethanol to butadiene results in the formation of acetaldehyde as the first intermediate which requires redox metal and inert atmosphere [28]. The presence of Zn in the 5%Zn/Si1 provided the redox atmosphere for the formation of acetaldehyde. The catalyst 5%Zn/NaZSM-5 showed 20% conversion and 90% selectivity towards acetaldehyde. The catalysts showed around 10% selectivity for crotonaldehyde initially, the third intermediate in the ethanol to butadiene route. The presence of Al group in zeolite can act as a Lewis

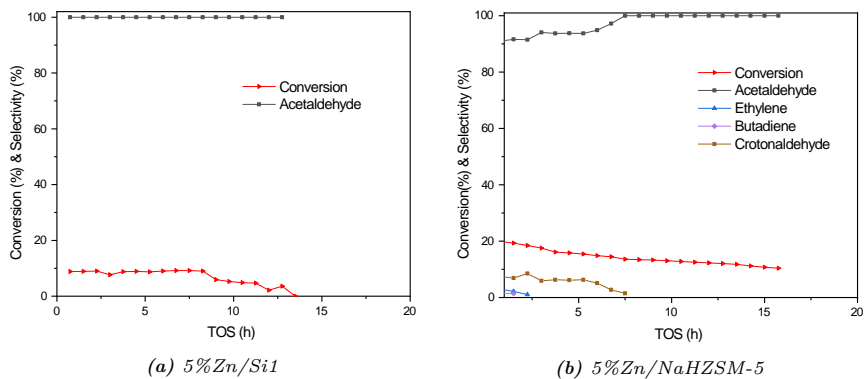


Figure 6.9: Catalytic performance of 5%/NaHZSM-5 and 5%Zn/Si1 at 320 °C and WHSV = 2.36 h⁻¹.

acid which can possibly catalyse the conversion of ethanol to butadiene [186].

Figure 6.10 shows the conversion of ethanol and butadiene selectivity of catalysts with different morphology tested at 320 °C and WHSV = 2.36 h⁻¹. The mesoporous HZSM-5 zeolite (5%Zn/MesoHZSM-5, 5%Zn/DesHZSM-5, 5%Zn/F127-HZSM-5) showed higher conversion and higher butadiene yield as compared to microporous HZSM-5 zeolite. Among all catalysts, the desilicated HZSM-5 zeolite loaded with 5% Zn (5%Zn/DesHZSM-5) showed the highest conversion and highest selectivity towards butadiene while 5%Zn/F127-HZSM-5 showed the lowest selectivity towards butadiene over 20 h of TOS. The catalyst 5%Zn/MesoHZSM-5 showed highest butadiene selectivity (82%) as compared to 5%Zn/DesHZSM-5. However, 5%Zn/MesoHZSM-5 showed the lowest conversion of all mesoporous zeolite.

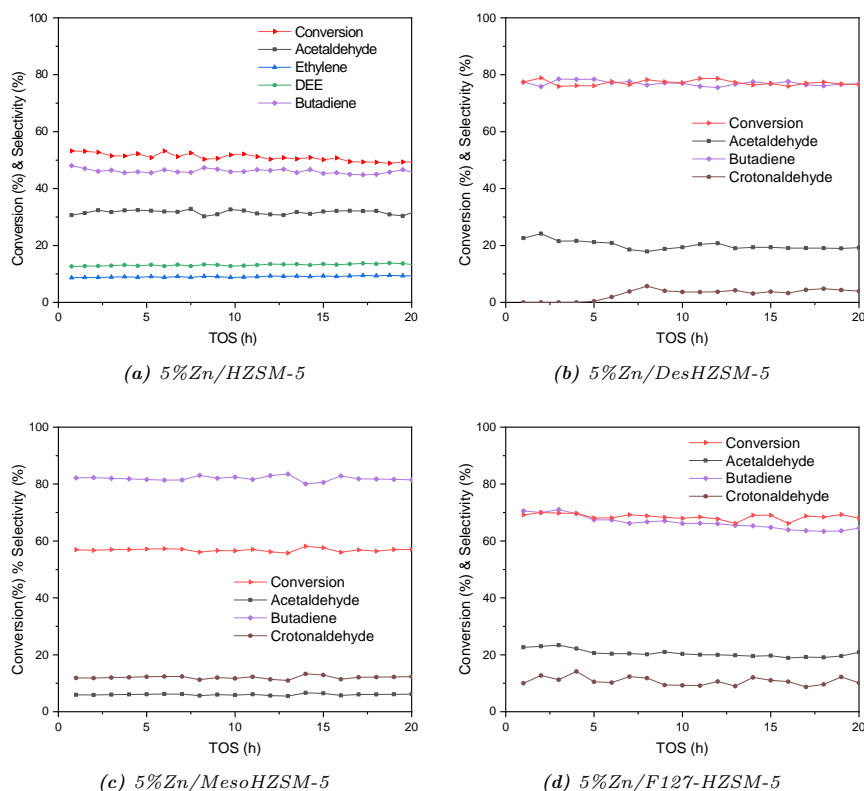


Figure 6.10: Catalytic performance with different morphology of HZSM-5 for Si/Al ratio = 150 at 320 °C and WHSV = 2.36 h⁻¹.

Moreover, the conversion of catalysts with 5% Zn followed the order

HZSM-5 < MesoHZSM-5 < F127-HZSM-5 < DesHZSM-5 as shown in Figure 6.11. The 5%Zn/DesHZSM-5 showed 79% butadiene selectivity. The catalysts 5%Zn/DesHZSM-5 and 5%Zn/MesoHZSM-5 showed no significant change in the stability for 20 h of TOS. In addition to butadiene, acetaldehyde and crotonaldehyde were formed as the by-products for mesoporous zeolites (DesHZSM-5, MesoHZSM-5 and F127-HZSM-5). The butadiene selectivity was dropped from 70 to 68% in the case of 5%Zn/F127-HZSM-5.

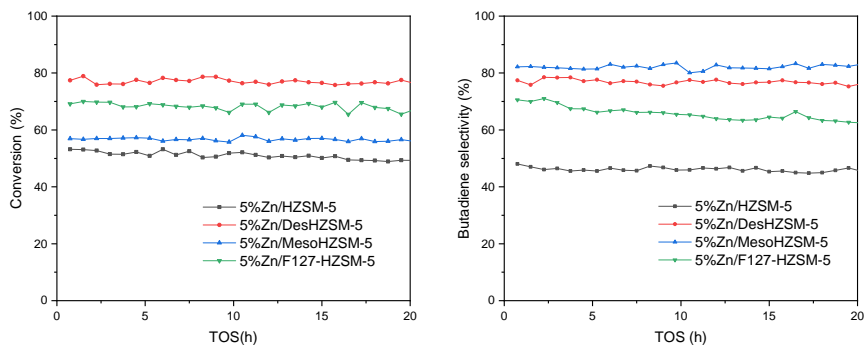


Figure 6.11: Conversion of ethanol and selectivity of butadiene for investigated catalysts.

The higher ethanol conversion over mesoporous zeolite as compared to microporous zeolite can be attributed to the larger surface area, which enables the fast adsorption of reactant bioethanol to the catalytic surface. Additionally, MesoHZSM-5 showed the largest crystal size (2-3 μm) and possibly limits the mass transfer of reactant through large crystal size. It was evident from the NH_3 -TPD that the density of weak acid was increased after loading with 5% Zn and this can attribute to an increase in the density of weak Lewis acid site. The density of weak acid sites were higher in the case of 5%Zn/DesHZSM-5 and followed the order DesHZSM-5 > MesoHZSM-5 > HZSM-5 > F127-HZSM-5 for 5%Zn loaded catalysts. The lower density of weak acid for 5%Zn/F127-HZSM-5 could be a possible explanation for lower butadiene yield among all mesoporous HZSM-5.

Goodarzi et al. have reported that Zn loaded in the zeolite can form two types of zinc species, one as spectator zinc and other as incorporated zinc. The spectator zinc can be easily reduced to its metallic form while the incorporated zinc was hardly reduced. The incorporated zinc exist as ZnOH^+ species resulting in the Lewis acidity of Zn species [211]. Additionally, various previous works have reported the role of zinc

in zeolite which can promote the aldol reaction and MPV reaction in the ETB reaction [208, 209, 213]. Therefore, the highest Lewis acidity resulted in the formation of the highest butadiene yield and ethanol conversion which in this case was DesHZSM-5. The optimum catalyst might have a balance between the Lewis-Brønsted acidity, redox property and porosity of the catalytic materials.

6.4 Summary

The work reports an efficient and highly selective heterogeneous catalyst comprised of Zn containing zeolite for the conversion of ethanol to 1,3-butadiene. Zn was supported in HZSM-5 zeolites with four different morphology. The hierarchical zeolite (DesHZSM-5, MesoHZSM-5 and F127-HZSM-5) showed highest conversion and selectivity as compared to conventional microporous HZSM-5 zeolite due to fast adsorption of reactant bioethanol to the catalytic surface and limited diffusion limitations. Among all synthesised materials, the desilicated HZSM-5 zeolite loaded with 5% Zn (5%Zn/DesHZSM-5) showed the highest conversion of almost 80% and highest yield of butadiene over 20 h of TOS. The highest activity of 5%Zn/DesHZSM-5 is possibly due to a balance between amount of Lewis acid sites, Brønsted acid sites, mesoporosity thereby attaining a close proximity of active centers. However, a detailed investigation on the zinc species and acidic strength is required to study the proximity of Zn species in the zeolite support.

Considering the demand for bio-based chemicals, the heterogeneous catalyst comprised of Zn containing desilicated HZSM-5 proved to be an optimum catalyst for the conversion of bioethanol to butadiene.

CHAPTER 7

One-step Conversion of Acetone to MIBK

Methyl isobutyl ketone (MIBK) is an organic solvent used commercially for gums, paints and varnishes. This chapter describes a novel one-step synthesis of MIBK from acetone at 150 °C and atmospheric pressure in a fixed bed continuous flow set-up. The reaction occurs over a heterogeneous bifunctional catalyst comprising Pd nanoparticles supported on HZSM-5 zeolite. The chapter addresses synthesis methodology, characterisation, catalytic test results and identifies the optimum catalyst for the synthesis of MIBK. Some of the results presented in this chapter are based on the article “Pd Nanoparticles Encapsulated in Mesoporous HZSM-5 Zeolite for Selective One-Step Conversion of Acetone to Methyl Isobutyl Ketone” [33].

7.1 Introduction

MIBK with the chemical formula $\text{CH}_3\text{COCH}_2\text{CH}(\text{CH}_3)_2$, is a colourless ketone, which is used as an organic solvent and chemical additive for the application in paints, surface coating, inks, adhesive, etc. MIBK has low solubility in water in comparison to other ketone solvents such as acetone and methyl ethyl ketone (MEK), and therefore makes MIBK a useful solvent for liquid-liquid extraction. It is identified as one of the top ten most popular organic solvents used in industry [215, 216]. A recent report on MIBK market in 2019 forecasted an increase in the MIBK global market with an estimated growth at a CAGR of 2.5 – 3.0% during the next five years. Due to the broad application of MIBK, demand for bio-based MIBK is increasing globally. Around 60% of global MIBK is produced from acetone [30, 217]. As discussed in Chapter 1, bioacetone can be synthesised from carbohydrates and starch with the aid of microorganism through the acetone-butanol-ethanol fermentation process.

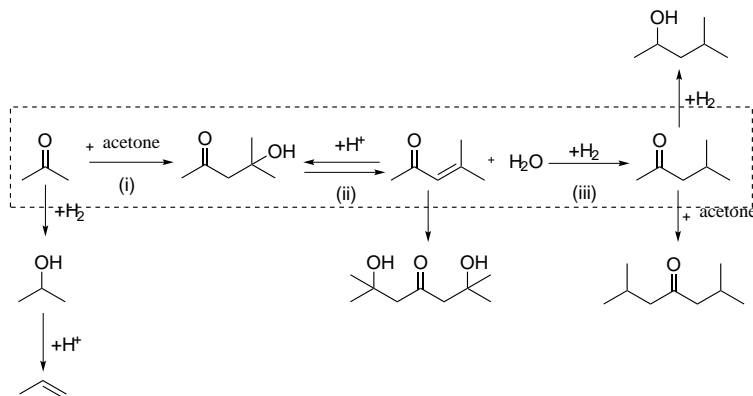


Figure 7.1: Conversion of MIBK to acetone using one-step synthesis.

Conversion of acetone to MIBK follows the scheme shown in Figure 7.1. Acetone first undergoes aldol reaction to produce diacetone alcohol (DAA) which then condenses to remove water molecule from DAA to form mesityl oxide (MO). Finally, C=C of MO undergoes selective hydrogenation to form MIBK.

Commercially, MIBK has been synthesised either by a one-pot direct conversion of acetone or by a three-stage process [218, 219]. The three-stage process requires additional purification and separation steps and results in a low MIBK yield [220, 221]. The single-stage catalytic system currently requires high operating pressure and harsh reaction condition resulting in fast deactivation of catalyst and poor selectivity. Bifunctional catalytic system with acidic or basic properties along with a reducing metal has been widely applied for the direct single-stage conversion. Palladium being particularly selective for the hydrogenation of double bond without affecting the carbonyl group was widely used for this reaction [222]. However, one of the challenges with the usage of palladium is the formation of side products during the reaction, for example an exposed and highly active palladium metal can reduce acetone to isopropanol. Additionally, highly acidic or basic sites present in the catalytic system can trigger an uncontrolled aldol condensation which results in the formation of higher hydrocarbon. Some of the side products formed are isophorones, diisobutyl ketone and methyl isobutyl carbinol [221, 223–226].

Depositing metal nanoparticles on supporting materials has proven to results in highly stable and selective catalysts [127, 131, 144, 152]. Although many supporting materials such as ZSM-5 [227, 228], CaO [229], ZnO–Cr₂O₃ [226, 230, 231] and SiO₂–MgO [232] have been reported in the literature, ZSM-5 zeolite is particularly

interesting for the single-stage conversion of acetone to MIBK due to its tunable acidity and improved selectivity and stability. However, the microporous structure of conventional HZSM-5 can induce diffusion limitation and act as a barrier for its efficient application in the MIBK synthesis process. A solution to overcome this drawback is to introduce mesopores on zeolites.

As part of this Ph.D. work, Pd nanoparticles supported on acidic HZSM-5 zeolite was used for the one-step synthesis of MIBK from acetone. Both conventional HZSM-5 and mesoporous HZSM-5 were synthesized to support Pd nanoparticles using incipient wetness impregnation and in-situ encapsulation methods. The porosity of the catalytic support and effect of encapsulation of metal nanoparticles were investigated for optimizing the catalytic activity. Additionally, the effect of acidity on the catalytic activity was studied by adjusting the Si/Al ratio of the HZSM-5 zeolite. List of bifunctional catalysts synthesised are shown in Table 7.1.

Table 7.1: *Bifunctional catalysts synthesised for one-step conversion of acetone to MIBK.*

Catalyst	Zeolite type	Method
Pd/HZSM-5	Conventional HZSM-5	Incipient wetness impregnation
Pd@HZSM-5	Conventional HZSM-5	In-situ encapsulation
Pd/MesoHZSM-5	Mesoporous HZSM-5	Incipient wetness impregnation
Pd@MesoHZSM-5	Mesoporous HZSM-5	In-situ encapsulation

7.2 Experimental section

7.2.1 Materials

Chemical used for the reaction includes tetrapropylammonium hydroxide (TPAOH, 1.0 M aqueous solution, Sigma Aldrich), tetraethylorthosilicate (TEOS, 99.99%, Sigma Aldrich), carbon black (Black Pearls 2000, Carbot Corporation), palladium chloride (PdCl_2 , 99%, Sigma Aldrich), ethylenediamine ($\text{NH}_2\text{CH}_2\text{CH}_2\text{NH}_3$, 99%, Sigma Aldrich), sodium aluminate (NaAlO_2 , 54 wt% AlO_2 and 41 wt% Na_2O , Riedel-de Haen), ammonium nitrate (NH_4NO_3 , 98%, Sigma Aldrich) and deionized water. All above chemicals were reagents grade and used without further purification.

7.2.2 Synthesis of materials

This section describes synthesis of various bifunctional catalysts prepared for the acetone conversion. This section is adapted by permission from Springer Nature [33].

7.2.2.1 Synthesis of Pd/HZSM-5

A series of HZSM-5 zeolite with different Si/Al ratio were prepared by following the method described in Section 2.2.4.2. This was followed by incipient wetness impregnation of the zeolite using an aqueous solution of PdCl_2 to synthesise Pd supported on conventional HZSM-5. Subsequently, the materials were dried and then reduced at 400 °C under flowing H_2 gas for 2 h. The as-synthesized materials include Pd/HZSM-5 with Si/Al ratio of 40, 80 and 120 and 0.3 wt% Pd.

7.2.2.2 Synthesis of Pd@HZSM-5

A modified literature procedure was used to synthesise in-situ encapsulated Pd nanoparticles in HZSM-5 [144]. In a 100 ml Teflon beaker, TPAOH (8.6 ml) was stirred with deionized water (6.9 ml) and NaAlO_2 (0.044 g) to get a clear solution. To the resulting solution, TEOS (4.46 ml) was added dropwise. After continuous stirring at room temperature for 6 h, a solution of ethylene diamine complex of Pd in deionized water was added to the mixture. This complex was prepared by mixing PdCl_2 (0.027 g) and ethylenediamine (0.22 ml) in deionized water (2.5 ml). The mixture was stirred at room temperature for another 30 min and then transferred to a Teflon-lined stainless steel autoclave. The crystallisation was conducted in a conventional oven at 170 °C for 96 h under static condition. The crystallised product was washed with water and ethanol several times and centrifugation at a speed of 1200 rpm. The resulting solid product was dried under 80 °C overnight and then calcined at 550 °C for 12 h. The as-synthesized material was then subjected to 3 consecutive steps of ion exchange to obtain the acidic HZSM-5 zeolite. For each ion-exchange step, zeolite (1 g) in 1 M aqueous NH_4NO_3 solution (80 ml) was stirred at 80 °C. The ion-exchanged product was dried at 80 °C overnight and calcined in air at 550 °C for 5 h to produce the desired H-form of the zeolite. The resulting material was reduced under a flow of H_2 at 400 °C for 2 h.

7.2.2.3 Synthesis of Pd/MesoHZSM-5

Mesoporous HZSM-5 zeolite was prepared by following the method described in Section 2.2.4.3. This was followed by incipient wetness impregnation of the zeolite using an aqueous solution of PdCl_2 to synthesise Pd supported MesoHZSM-5. Subsequently, the materials were dried and reduced at 400 °C under flowing H_2 gas for 2 h. The as-synthesised material assigned as Pd/MesoHZSM-5 with Si/Al ratio of 40 contained 0.3 wt% Pd.

7.2.2.4 Synthesis of Pd@Meso-HZSM5

The in-situ procedure for synthesis of encapsulated palladium nanoparticles in mesoporous HZSM-5 is as follows. A solution of Pd complex was prepared by mixing PdCl_2 (0.053 g) with ethylenediamine (0.4 ml) and deionized water (2.5 ml). The as-synthesized complex solution was then mixed with a clear solution of TPAOH (8.6 ml) and NaAlO_2 (0.015 g) and stirred for 15 min. Pre-dried carbon black (2 g) was taken in a Teflon beaker and impregnated with the homogeneous mixture of TPAOH and NaAlO_2 and dried at room temperature overnight. Following this, the material was impregnated with TEOS (4.46 ml) and dried at room temperature overnight. The Teflon beaker was placed in a Teflon-lined stainless steel autoclave (130 ml) containing distilled water (15 ml) and heated to 180 °C for 72 h. The product was collected and washed using distilled water. The material was dried at 80 °C overnight and calcined at 550 °C for 20 h. Finally, the product was ion-exchanged with NH_4NO_3 solution to obtain Pd@MesoHZSM-5 by following the same procedure mentioned for synthesis of Pd@HZSM-5 and reduced at 400 °C for 2 h under the flow of hydrogen.

7.2.3 Characterisation

All the samples were characterised using various techniques including XRD, nitrogen physisorption, SEM, TEM, XPS and TPD. The equipment used and conditions applied for different analysis are specified in Chapter 3.

7.2.4 Gas-phase conversion of acetone to MIBK

The gas-phase direct conversion of acetone to MIBK was conducted in a continuous fixed bed continuous flow reactor. In a typical reaction, 100 mg of fractionated catalyst (185-355 μm) was loaded in a stainless steel reactor having 3 mm diameter.

Acetone was pumped into an evaporator at 135 °C and mixed with hydrogen (50 ml/min) with a weight hourly space velocity of 23.5 g acetone/g catalyst /h. The gas mixture was passed through the fixed catalyst bed containing 100 mg catalyst. The product mixture was analysed using an online GC-FID on a regular interval. The product mixture was collected externally to identify all the unknown products and injected in GC-MS. A simplified diagram of the reactor set up is given in Figure 7.2. All catalysts were tested under similar conditions with a temperature range from 100 °C to 250 °C at atmospheric pressure. Furthermore, the stability test for the selected catalysts was carried out by keeping the temperature at 150 °C with same weight hourly space velocity for 20 h. The set up was controlled by a pre-programmed LabVIEW script.

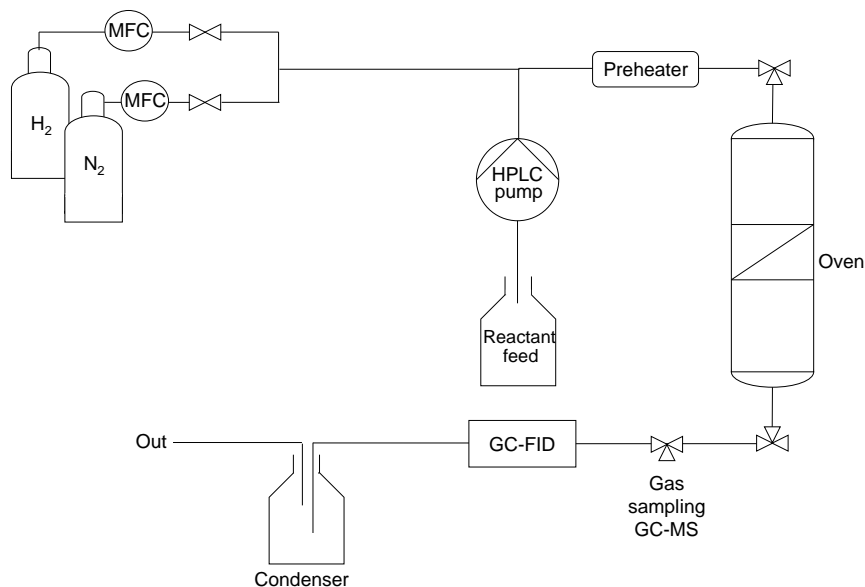


Figure 7.2: Schematic illustration of reactor flow setup.

7.3 Results and discussions

This section describes the results obtained through various characterisation techniques for as-synthesised materials. This was followed by the test for performance of catalysts for the MIBK synthesis from acetone. In total, seven different catalysts

were considered for investigation, i.e. Pd/HZSM-5 with Si/Al ratio 40, 80 and 120, Pd@HZSM-5 with Si/Al ratio 40, Pd/MesoHZSM-5 with Si/Al ratio 40 and Pd@MesoHZSM-5 with Si/Al ratio 40. All catalysts were synthesised with 0.3 wt% Pd loading.

7.3.1 Characterisation results

7.3.1.1 XRD

Figure 7.3 shows XRD pattern of Pd/HZSM-5, Pd@HZSM-5, Pd/MesoHZSM-5 and Pd@MesoHZSM-5 with Si/Al = 40. All four samples showed the typical diffraction pattern for MFI crystalline structure [233]. No additional peaks were observed for any of the materials. The diffraction peaks of Pd at $2\theta = 40.5^\circ$ and 46.8° corresponding to lattice plane (111) and (200), respectively were not observed in any of the samples [234]. This may be either due to the small size of Pd nanoparticles or overlapping of diffraction peaks of Pd and MFI structured zeolite.

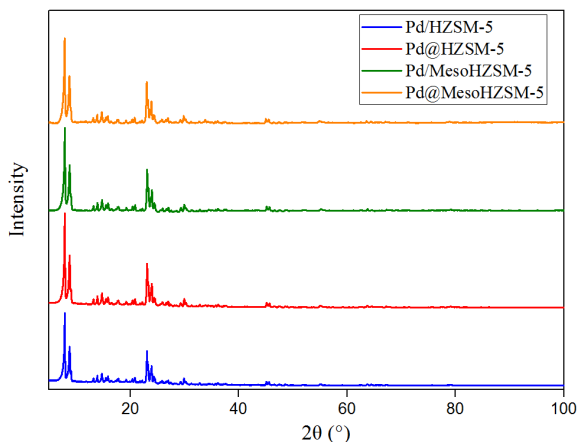


Figure 7.3: XRD pattern of the prepared samples. Reprinted by permission from Springer Nature [33].

7.3.1.2 Nitrogen physisorption

Figure 7.4 shows the nitrogen physisorption isotherm of synthesised catalysts with Si/Al = 40. Pd/HZSM-5 and Pd@HZSM-5 showed the type I isotherm which is characteristics of microporous materials, whereas Pd/MesoHZSM-5 and

Pd@MesoHZSM-5 showed type IV isotherm typical for mesoporous zeolites with H4 hysteresis loop [113]. This hysteresis loop originates from the narrow pore size distribution in the mesoporous zeolites. The small hysteresis loop around $p/p^0 = 0.18$

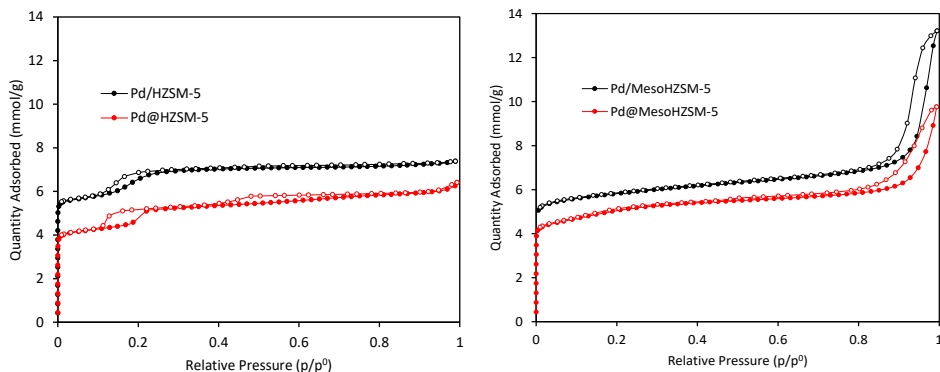


Figure 7.4: Isotherms of synthesised materials. Reprinted by permission from Springer Nature [33].

in the case of Pd/HZSM-5 and Pd@HZSM-5 is probably due to transition of fluid to crystal phase, which is typical for nitrogen in MFI micropores. However, a small hysteresis loop was observed for Pd@HZMS-5 that closes around $p/p^0 = 0.42$. This is originated from Tensile Strength Effect (TSE) owing to the capillary evaporation during the desorption of adsorbed gas molecule via a hemispherical meniscus [98].

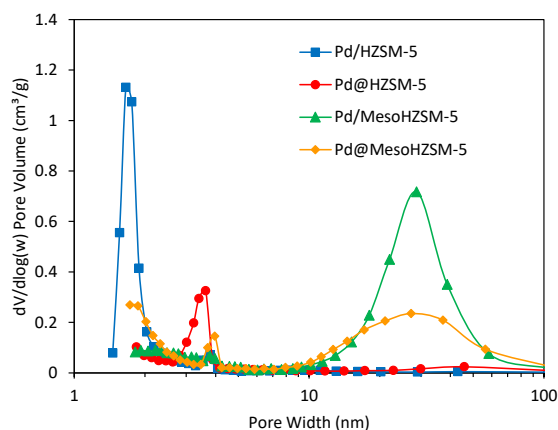


Figure 7.5: Pore width distribution of prepared samples. Reprinted by permission from Springer Nature [33].

Figure 7.5 shows the pore size distribution of the prepared materials derived from the desorption branch of isotherm by the BJH method. The pore size distribution of Pd/HZSM-5 and Pd@HZSM-5 showed a narrow peak in the region of 2-3 nm. The samples Pd/MesoHZSM-5 and Pd@MesoHZSM-5 showed a broad pore size distribution in the range 20-30 nm, which is consistent with a typical mesoporous zeolite.

Table 7.2: Nitrogen physisorption data of investigated materials. Reprinted by permission from Springer Nature [33].

Catalysts	V_{total}^a cm^3g^{-1}	V_{micro}^b cm^3g^{-1}	S_{BET}^c m^2g^{-1}	Metal loading
Pd/HZSM-5	0.232	0.102	388	0.30
Pd@HZSM-5	0.202	0.138	357	0.29
Pd/MesoHZSM-5	0.306	0.150	432	0.30
Pd@MesoHZSM-5	0.258	0.107	383	0.27

^a V_{total} determined from the isotherm adsorption branch at around $p/p^0 = 0.95$.

^b V_{micro} calculated by the t -plot method.

^c S_{BET} calculated by the BET method.

Table 7.2 shows the data obtained from nitrogen physisorption of prepared samples. The total pore volume of both Pd/MesoHZSM-5 and Pd@MesoHZSM-5 was higher than of Pd/HZSM-5 and Pd@HZSM-5. The specific surface area of Pd/MesoHZSM-5 was higher as compared to the other three materials. The specific surface area and total pore volume of Pd@MesoHZSM-5 was less as compared to Pd/MesoHZSM-5. This is probably due to some defect caused by the ethylene diamine complex used during the reaction.

7.3.1.3 SEM

The SEM images for the synthesised materials are shown in Figure 7.6. The crystal size of both Pd/HZSM-5 and Pd@HZSM-5 were in the range of 300 to 400 nm, whereas the crystal size of Pd/MesoHZSM-5 and Pd@MesoHZSM-5 were in the range of 2 - 2.5 μm . The small crystal size can benefit the catalytic activity due to improved mass transfer through the pores of the porous support. Additionally, both Pd/MesoHZSM-5 and Pd@MesoHZSM-5 showed non-crystallographic mesopores. The presence of these mesopores resulted in the relatively large average pore of single crystals samples. This is in line with the results obtained from nitrogen physisorption analysis.

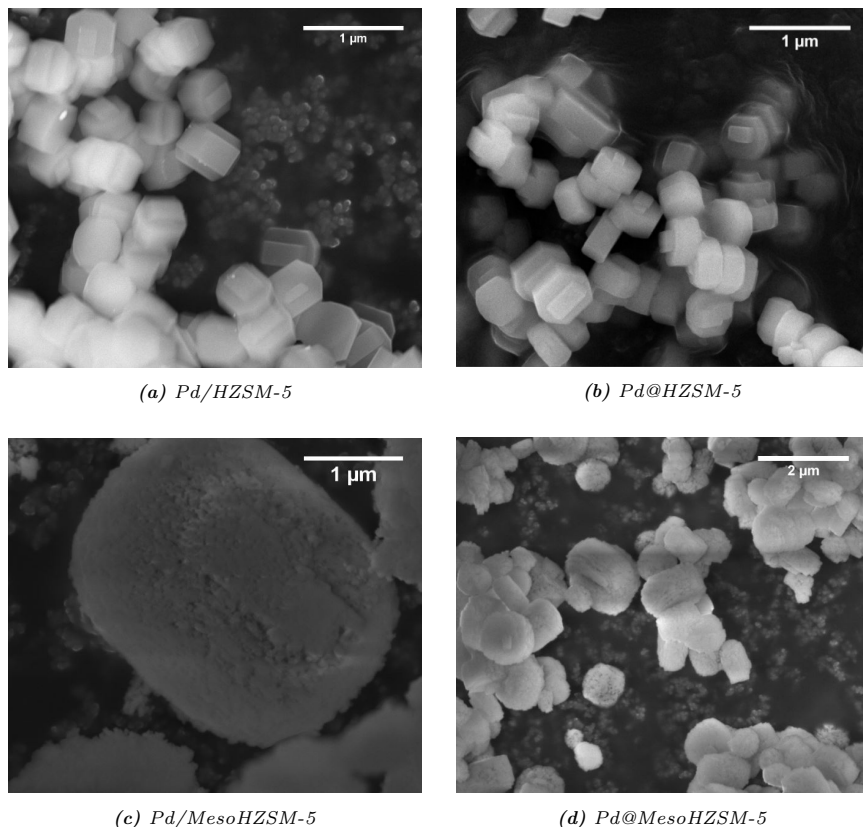


Figure 7.6: SEM images of prepared materials. Reprinted by permission from Springer Nature [33].

7.3.1.4 TEM

Figure 7.7 shows the TEM images of as-synthesized materials. The TEM image of Pd@HZSM-5 showed small and uniformly distributed palladium nanoparticles with size ranges from 1-2 nm. It is clear from the image that almost all nanoparticles are located on the interior part of zeolite crystals. The TEM image of Pd/HZSM-5 showed large nanoparticles with nanoparticles distributed both on the external surface and internal region. The size of the nanoparticles were in the range of 5 - 30 nm. The Pd nanoparticles in Pd/MesoHZSM-5 were in the size range of 5 - 7 nm with uniform distribution. Pd nanoparticles were not observed in TEM images of Pd@MesoHZSM-5 and this is probably due to the small size of nanoparticles.

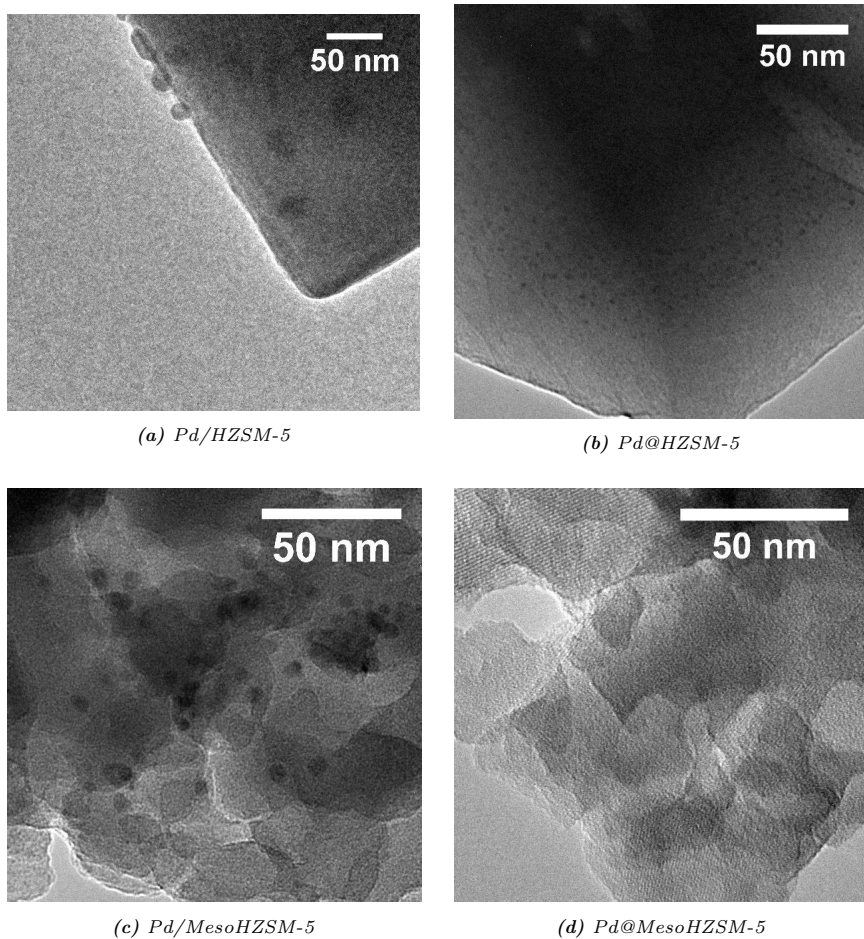


Figure 7.7: TEM images of prepared materials. Reprinted by permission from Springer Nature [33].

7.3.1.5 XPS

The 3D view of the zeolite crystals was not possible using the TEM image and therefore XPS image was used to detect the presence of Pd on the surface of the zeolite. Figure 7.8 shows the photopeak of Pd obtained from the XPS data of four samples. The appearance of Pd photopeak in Pd/HZSM-5 and Pd/MesoHZSM-5 samples shows that Pd nanoparticles are located on the surface of zeolite support. However, the Pd peak of Pd/MesoHZSM-5 was with more noise and the presence of Pd was nearly negligible. The absence of Pd photopeak for Pd@HZSM-5 and

Pd@MesoHZSM-5 samples indicates the encapsulation of the nanoparticles in the zeolite crystals.

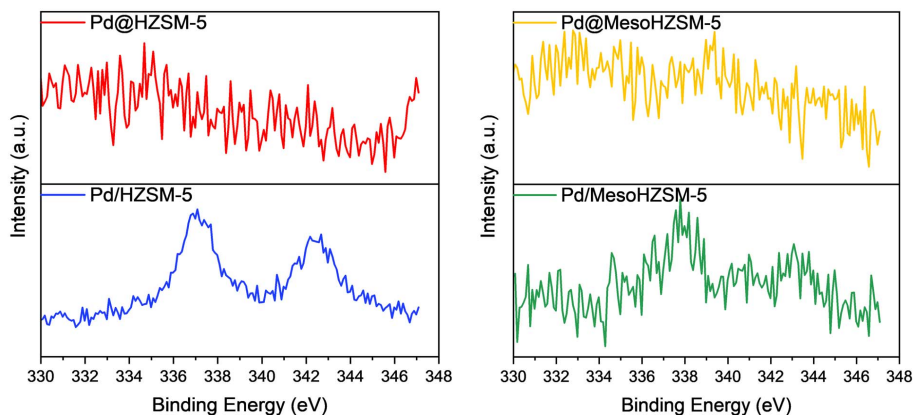


Figure 7.8: XPS analysis of prepared materials.

7.3.2 Catalytic activity

The one-step conversion of acetone to MIBK was tested using the prepared catalysts. The catalytic activity was carried out over a temperature range of 120 to 290 °C with 100 mg of catalyst. Various parameters like acidity, mesoporosity of zeolite support and encapsulation of nanoparticles were tested.

To study the influence of Si to Al ratio of HZSM-5 zeolite and hence the effect of acidity on conversion and selectivity, the Si/Al ratios were varied by changing the concentration of NaAlO_2 . Figure 7.9 shows the results from the one-step conversion of acetone as a function of temperature and time in a continuous flow reaction set up. The reaction was carried out from 120 to 290 °C. It is expected that a highly acidic group could favour the first two steps of the scheme in Figure 7.1. Since a higher Al content in the zeolite increases the acidic strength, Si/Al = 40 is expected to show highest conversion [220, 228]. In general, the conversion of acetone increased with the temperature upto 180 - 200 °C and then decreased. This decrease in the conversion at higher temperature is possibility due to the deactivation of catalysts by coking. The yield versus temperature plotted in Figure 7.9 showed the similar trend. The zeolite with Si/Al = 40 showed higher conversion and yield of MIBK. Other products formed during the reaction were propene and isopropyl alcohol.

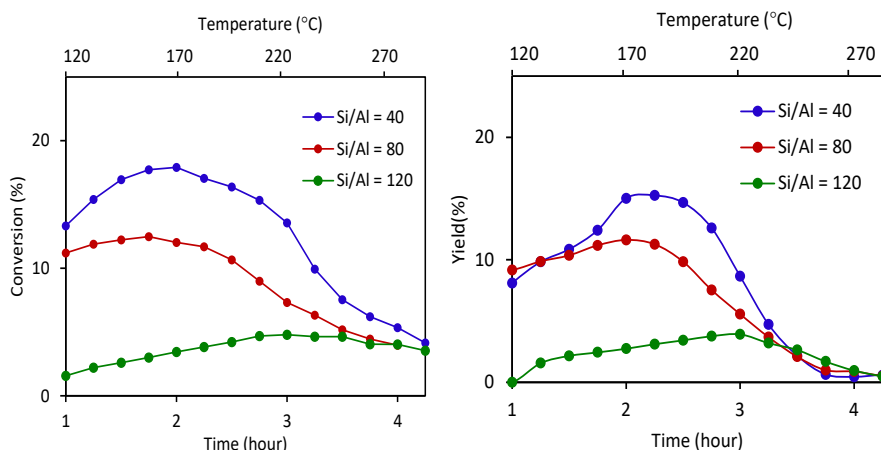


Figure 7.9: Effect of Si/Al ratio on acetone conversion and yield. Reprinted by permission from Springer Nature [33].

Pd nanoparticles were supported on HZSM-5 zeolite via in-situ encapsulation (Pd@HZSM-5 and Pd/MesoHZSM-5) and incipient wetness impregnation (Pd/HZSM-5 and Pd/MesoHZSM-5) and therefore its effect on selectivity and conversion were investigated to find the best suitable method for the MIBK synthesis. Figure 7.10 shows the conversion results obtained for catalyst with different preparation methods. Pd@MesoHZSM-5 showed higher conversion compared to other catalysts.

The influence of temperature on catalytic activity is also shown in Figure 7.10. The catalysts were tested at the temperature range of 120 °C to 290 °C for the Si/Al ratio of 40. The results illustrated almost all catalysts showing highest catalytic activity at the temperature between 160 °C to 200 °C with conversion rate decreasing at higher temperatures.

Additionally, selectivity was also plotted in Figure 7.11. As shown in the figure, selectivity for MIBK over Pd@MesoHZSM-5 was nearly 90% against Pd@HZSM-5, which was nearly 30%. In the case of Pd@HZSM-5, the side products were isopropyl alcohol (60%) and propylene (10%) at 150 °C. Pd/HZSM-5 showed nearly 70% selectivity towards MIBK. The lower selectivity of Pd/HZSM-5 and Pd@HZSM-5 can be related to the diffusion limitation of acetone over small pore size of HZSM-5 support thereby forming isopropyl alcohol and propylene [75]. This diffusion limitation of substrate was expected to improve by introducing secondary porosity on

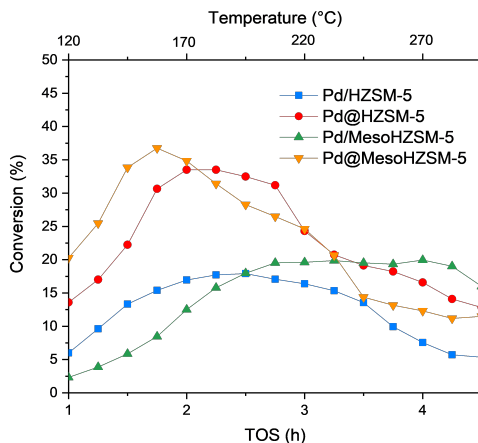


Figure 7.10: Effect of catalyst preparation methods and temperature on conversion. Reprinted by permission from Springer Nature [33].

HZSM-5. This is in agreement with the results obtained for Pd@MesoHZSM-5 which showed 99% selectivity at 150 °C towards MIBK. However, no such improvement in selectivity was observed for Pd/MesoHZSM-5.

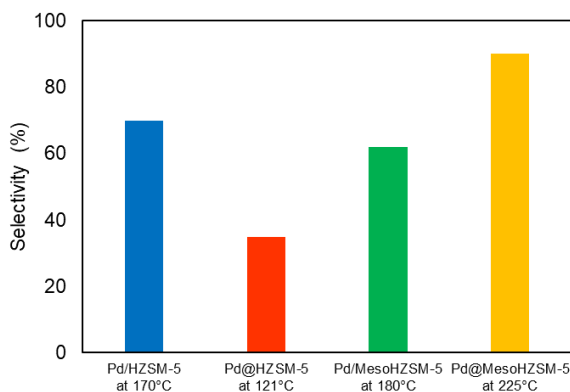


Figure 7.11: Effect of catalyst preparation methods on selectivity. Reprinted by permission from Springer Nature [33].

Figure 7.12 shows the stability test of the catalysts at 150 °C for 20 h. The Pd@MesoHZSM-5 showed highest conversion among the four tested catalysts at 150 °C. The conversion of acetone by Pd/MesoHZSM-5 showed only half of the activity exhibited by Pd@MesoHZSM-5 although they showed similar mesoporosity. The

highest activity of Pd@MesoHZSM-5 originates from the small Pd nanoparticles. All catalysts showed a deactivation after 20 h. Moreover, Pd@MesoHZSM-5 showed nearly 100% selectivity towards MIBK even after 20 h. The selectivity for MIBK was in the order Pd@MesoHZSM-5 > Pd@HZSM-5 > Pd/MesoHZSM-5 > Pd/HZSM-5. The high selectivity of Pd@MesoHZSM-5 towards MIBK is due to the fact that Pd nanoparticles were encapsulated in the mesopores of MesoHZSM-5 preventing the formation of unwanted side products.

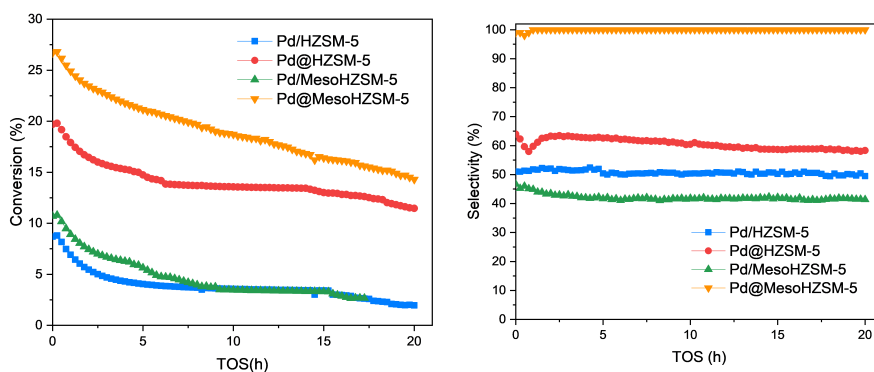


Figure 7.12: Stability test of the catalysts at 150 °C. Reprinted by permission from Springer Nature [33].

The catalyst were collected after stability tests for testing the reusability. The spent catalysts were analysed using thermogravimetry analysis (TGA). The results are shown in Figure 7.13.

Based on TGA analysis, Pd/HZSM-5 showed highest weight loss of about 5%, while Pd@HZSM-5 showed the least weight loss. The curve showed two weight losses over temperature 150 - 200 °C and 200 - 400 °C. The weight loss at temperature < 200 °C could be attributed to removal of adsorbed water while the weight loss at 200 - 400 °C was due to the removal of coke formed in the catalysts. All materials showed no loss of weight after 450 °C [37]. In order to reuse the catalysts, the spent catalysts were collected in silica crucible and calcined in a muffle oven at 500 °C for 1 h with a ramp of 10 °C per min. Figure 7.14 shows the regeneration of the catalyst Pd@MesoHZSM-5, where spent catalyst showed clear black colour and regained its original colour after calcination. During the calcination, the coke deposited on the material was oxidised and burned off. This coke deposited on the materials caused the mass transfer limitation and blocked the pores thereby making active sites inaccessible for reactant molecule.

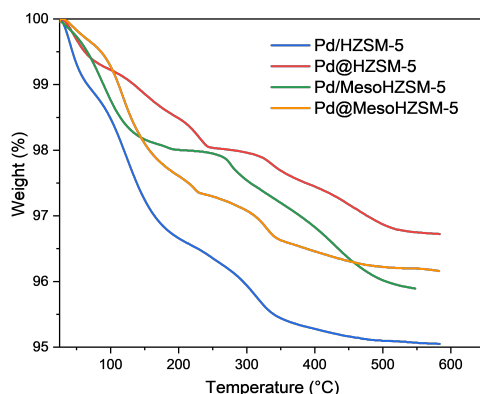


Figure 7.13: TGA of spent catalysts. Reprinted by permission from Springer Nature [33].

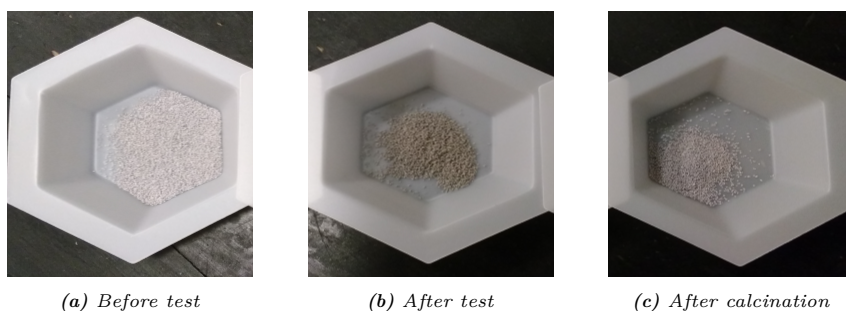


Figure 7.14: Regeneration of the catalyst Pd@MesoHZSM-5.

All catalysts were regenerated under the identical conditions. The results obtained for Pd/HZSM-5 and Pd@MesoHZSM-5 are shown in Figure 7.15. Both catalysts retained their initial activity after regeneration in their first cycle. However, cycle 2 of Pd/HZSM-5 showed fast deactivation as compared to cycle 1. Pd/HZSM-5 retained 30% of its initial activity after first cycle while it retained only 15% of its activity after 20 h of continuous flow reaction in cycle 2. Pd@MesoHZSM-5 retained almost 100% of its initial activity after regeneration. First regeneration retained 50% of initial activity of Pd@MesoHZSM-5 even after 20 h under continuous flow and showed good reusability even after cycle 4. The difference in the activity and regeneration is possibly due to the collective effect of encapsulation and mesoporosity. The encapsulation of Pd nanoparticles could stabilises the nanoparticles and inhibit

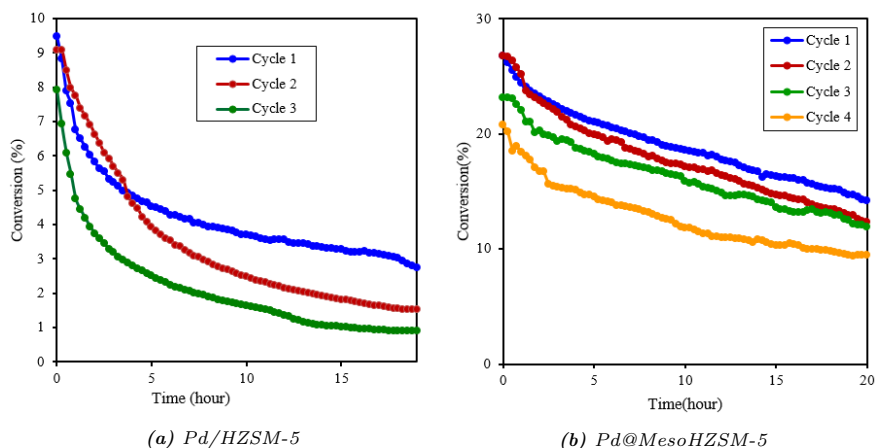


Figure 7.15: Conversion after regeneration of catalyst at 150 °C. Reprinted by permission from Springer Nature [33].

sintering. Additionally, the coke formation causing the mass transfer limitation is quite severe in the microporous Pd/HZSM-5.

The catalysts after regeneration were analysed using XRD to observe any deformation in MFI structure of zeolite and agglomeration or sintering of Pd nanoparticles. The XRD pattern of the spent catalysts shown in Figure 7.16 shows

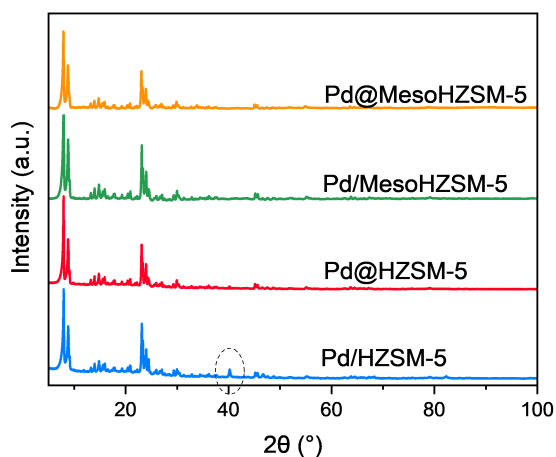


Figure 7.16: XRD pattern of spent catalysts.

that catalysts retained their MFI structure after regeneration. Among four catalysts, Pd/HZSM-5 showed a very small peak of Pd(111) = 40.5°. This is due to the formation of large Pd nanoparticles in Pd/HZSM-5. However, the absence of Pd peak in all other samples indicates less agglomeration of Pd nanoparticles [227].

7.4 Summary

The work reports a novel bifunctional catalyst comprising of Pd nanoparticles supported over zeolite for the selective synthesis of acetone to methyl isobutyl ketone at a low temperature of 150 °C. The nanoparticles were supported on conventional HZSM-5 and mesoporous HZSM-5 using both incipient wetness impregnation and in-situ encapsulation. Among all synthesised catalysts, Pd nanoparticles encapsulated on mesoporous zeolite via in-situ encapsulation, Pd@MesoHZSM-5, showed the best catalytic activity with 37% conversion and >99% selectivity for MIBK for the conversion of acetone to MIBK. Moreover, the catalyst showed nearly 100% selectivity towards MIBK even after 20 h. The mesoporous structure of the zeolite enabled the catalyst to overcome the diffusion limitation making it more active. The effect of acidity on the catalytic activity revealed the highest activity for HZSM-5 for Si/Al ratio of 40.

Considering the future need of bio-based chemicals, the bifunctional heterogeneous catalyst supported on mesoporous zeolite is a potential candidate for large scale production of MIBK from bioacetone. Furthermore, the study opens up application of zeolite catalysis for the production of industrially important chemicals by utilising mesoporous zeolites against the diffusion constraints.

CHAPTER 8

Conclusion

As a consequence of stringent environmental regulations on reducing the greenhouse gases and demand for developing energy-efficient sustainable solutions, conversion of biomass-derived compounds to value-added chemicals hold great promises for the future of the chemical industry. This thesis focused on the conversion of biomass-derived C_1 to C_3 chemicals to industrially significant compounds such as hydrogen, acetaldehyde, 1,3-butadiene and methyl isobutyl ketone by synthesising highly active, stable and selective heterogeneous catalysts comprised of supported metal nanoparticles.

Decomposition of formic acid to hydrogen provides a sustainable solution to utilize hydrogen for renewable energy storage application. Chapter 4 reports an efficient and highly selective bimetallic heterogeneous catalyst comprised of Au and Pd metal nanoparticles supported on zeolite silicalite-1 for the decomposition of formic acid to hydrogen and CO_2 . Au and Pd nanoparticles were supported on silicalite-1 using incipient wetness impregnation, in-situ encapsulation and pressure-assisted impregnation to demonstrate their stability, catalytic activity and selectivity for decomposition of formic acid to hydrogen. Among all synthesised materials, the bimetallic catalyst with Pd/Au mass ratio of 2:1 and in-situ encapsulated in silicalite-1 showed the best catalytic performance with 50% yield of H_2 at 85 °C and 99% yield of H_2 from 130 °C.

Chapter 5 describes the selective conversion of ethanol to acetaldehyde via dehydrogenation using Cu nanoparticles supported on nitrogen-doped ordered mesoporous carbon. Nitrogen-doped ordered mesoporous carbon support was prepared by carbonization of a templated polymer with nitrogen precursor. It was found that nitrogen-doped ordered mesoporous carbon can prevent steam induced sintering of nanoparticles, increases the metal-support interactions and improves the catalytic performance of the catalysts in ethanol dehydrogenation. Among all synthesised materials, Cu supported over mesoporous carbon with approx. 7% nitrogen

doping resulted in the selectivity of acetaldehyde with over 99% and STY of 175.9 mol_{acetaldehyde}/mol_{Cu}/h.

The heterogeneous catalytic system can be designed for its multifunctional application to catalyse more than one step in a reaction set-up. Chapter 6 describes the one step conversion of ethanol to 1,3-butadiene using a multifunctional catalytic system containing the optimum amount of a redox, Brønsted and Lewis acid sites. A set of Zn loaded acidic zeolites with four different morphologies: conventional HZSM-5, desilicated HZSM-5, carbon-template assisted mesoporous HZSM-5 and surfactant F-127 assisted mesoporous HZSM-5, were synthesised to find the optimum catalyst for ethanol to 1,3-butadiene conversion. Among all synthesised materials, the desilicated HZSM-5 with 5% zinc loading showed the highest conversion of almost 80% and highest yield of butadiene over 20 h of TOS. The introduction of mesoporosity into zeolite increased the fast adsorption of reactant bioethanol to the catalytic surface and improved diffusion limitations. It was concluded that improved mass transfer in mesoporous zeolite, high density of weak acid sites due to incorporation of Zn into zeolite and close proximity of active centers contributed to the high catalytic performance of desilicated HZSM-5.

Chapter 7 describes a novel bifunctional catalyst consisting of a reducing metal Pd supported on acidic zeolite for the one-step conversion of acetone to methyl isobutyl ketone. Pd nanoparticles were supported using both incipient wetness impregnation and in-situ encapsulation in conventional HZSM-5 and mesoporous HZSM-5. Among all synthesised materials, Pd nanoparticles encapsulated in mesoporous zeolite via in-situ encapsulation showed the best catalytic activity with 37% conversion and >99% selectivity for MIBK at 150 °C. The introduction of mesoporosity on the zeolite enabled the catalyst to overcome the diffusion limitation and improved the mass transfer limitation through the zeolite support and made the catalyst more active. Additionally, the catalyst showed good stability over time due to less particles migration and prevented the nanoparticles from sintering.

The work has shown that supported nanoparticles can help providing a green alternative to produce value-added chemicals from biomass-derived chemicals. This work, therefore, opens up numerous opportunities to synthesise industrially important chemicals from biomass-derived compounds using heterogeneous catalysis thereby helping to reduce the CO₂ emission and limit global warming.

Bibliography

- [1] Y. J. Zhou, E. J. Kerkhoven, J. Nielsen, *Nature Energy* **2018**, *3*, 925–935.
- [2] J. C. Serrano-Ruiz, R. Luque, A. Sepúlveda-Escribano, *Chemical Society Reviews* **2011**, *40*, 5266–5281.
- [3] W. Y. Chen, T. Suzuki, M. Lackner, *Handbook of climate change mitigation and adaptation, second edition, Vol. 1-4*, Springer, NY, **2016**.
- [4] A. Camia, N. Rober, R. Jonsson, R. Pilli, S. Garcia-Condado, R. Lopez-Lozano, M. van der Velde, T. Ronzon, P. Gurria, R. M'Barek, S. Tamosiunas, G. Fiore, R. Araujo, N. Hoepffner, L. Marelli, J. Giuntoli, *Biomass production, supply, uses and flows in the European Union. First results from an integrated assessment*, **2018**.
- [5] R. Harun, M. K. Danquah, G. M. Forde, *Journal of Chemical Technology and Biotechnology* **2010**, *85*, 199–203.
- [6] H. T. Abdulrazzaq, T. J. Schwartz, *Catalytic Conversion of Ethanol to Commodity and Specialty Chemicals*, Elsevier Inc., **2018**.
- [7] K. Kohli, R. Prajapati, B. K. Sharma, *Energies* **2019**, *12*, 233.
- [8] B. Voss, “Value-added Chemicals from Biomass by Heterogeneous Catalysis”, PhD thesis, Technical University of Denmark, **2011**.
- [9] S. Kim, Y. F. Tsang, E. E. Kwon, K. Y. A. Lin, J. Lee, *Korean Journal of Chemical Engineering* **2019**, *36*, 1–11.
- [10] C. Pischetola, L. Collado, M. Keane, F. Cárdenas-Lizana, *Molecules* **2018**, *23*, 2905.
- [11] J. Long, Y. Xu, W. Zhao, H. Li, S. Yang, *Frontiers in Chemistry* **2019**, *7*, 529.
- [12] S. Santoro, S. I. Kozhushkov, L. Ackermann, L. Vaccaro, *Green Chemistry* **2016**, *18*, 3471–3493.

- [13] T. Werpy, G. Petersen, Top Value Added Chemicals from Biomass: Volume I – Results of Screening for Potential Candidates from Sugars and Synthesis Gas, tech. rep., United States, **2004**.
- [14] M. Orazov, “Development and Characterization of Catalytic Systems for Biomass-Derived Chemical Feedstocks”, PhD thesis, California Institute of Technology, **2017**.
- [15] Q. N. Wang, L. Shi, W. Li, W. C. Li, R. Si, F. Schüth, A. H. Lu, *Catalysis Science and Technology* **2018**, *8*, 472–479.
- [16] K. Müller, K. Brooks, T. Autrey, *Energy & Fuels* **2017**, *31*, 12603–12611.
- [17] P. Preuster, J. Albert, *Energy Technology* **2018**, *6*, 501–509.
- [18] V. P. Muiuane, M. Ferreira, P. Bignet, A. P. Bettencourt, P. Parpot, *Journal of Environmental Chemical Engineering* **2013**, *1*, 1237–1244.
- [19] A. Bušić, N. Mardetko, S. Kundas, G. Morzak, H. Belskaya, M. Ivancic Santek, D. Komes, S. Novak, B. Šantek, *Food Technology and Biotechnology* **2018**, *56*.
- [20] J. Peña-Castro, S. Del Moral, L. Núñez-López, B. Barrera-Figueroa, L. Amaya-Delgado, *BioMed Research International* **2017**, *2017*, 1–10.
- [21] J. Sun, Y. Wang, *ACS Catalysis* **2014**, *4*, 1078–1090.
- [22] CropEnergies AG, Renewable ethanol as a growth market, **2018**, http://www.cropenergies.com/en/Ethanol/Markt/Dynamisches_Wachstum/ (visited on 02/10/2020).
- [23] J. Mielby, J. O. Abildstrøm, F. Wang, T. Kasama, C. Weidenthaler, S. Kegnaes, *Angewandte Chemie - International Edition* **2014**, *53*, 12513–12516.
- [24] L. V. Mattos, G. Jacobs, B. H. Davis, F. B. Noronha, *Chemical Reviews* **2012**, *112*, 4094–4123.
- [25] G. M. Lari, K. Desai, C. Mondelli, J. Pérez-Ramírez, *Catalysis Science and Technology* **2016**, *6*, 2706–2714.
- [26] E. A. Redina, A. A. Greish, I. V. Mishin, G. I. Kapustin, O. P. Tkachenko, O. A. Kirichenko, L. M. Kustov, *Catalysis Today* **2015**, *241*, 246–254.
- [27] S. Tayrabekova, P. Mäki-Arvela, M. Peurla, P. Paturi, K. Eränen, G. E. Ergazieva, A. Aho, D. Y. Murzin, K. Dossumov, *Comptes Rendus Chimie* **2018**, *21*, 194–209.

- [28] P. I. Kyriienko, O. V. Larina, S. O. Soloviev, S. M. Orlyk, C. Calers, S. Dzwigaj, *ACS Sustainable Chemistry and Engineering* **2017**, *5*, 2075–2083.
- [29] M. D. Jones, C. G. Keir, C. D. Iulio, R. A. M. Robertson, C. V. Williams, D. C. Apperley, *Catal. Sci. Technol. Catal. Sci. Technol* **2011**, *1*, 267–272.
- [30] D. M. Zhao, X. P. Liu, *Advanced Materials Research* **2012**, *577*, 101–104.
- [31] Y. Wang, H. Janssen, H. Blaschek, *Fermentative Biobutanol Production: An Old Topic with Remarkable Recent Advances*, John Wiley Sons, **2014**, pp. 227–260.
- [32] K. Karimi, M. Tabatabaei, I. S. Horváth, R. Kumar, *Biofuel Research Journal* **2015**, *2*, 301–308.
- [33] R. Pulikkal Thumbayil, J. Mielby, S. Kegnaes, *Topics in Catalysis* **2019**, *62*, 678–688.
- [34] J. G. De Vries, S. D. Jackson, *Catalysis Science and Technology* **2012**, *2*, 2009–2009.
- [35] O. Deutschmann, H. Knözinger, K. Kochloeff, T. Turek, *Ullmann's Encyclopedia of Industrial Chemistry* **2009**, 1–95.
- [36] E. E. Wolf, *Chemical Engineering Education* **1981**, *15*, 214–217.
- [37] G. Ertl, H. Knözinger, J. Weitkamp, *Handbook of Heterogeneous Catalysis, Vol. 1-5*, **2008**.
- [38] M. Boudart, *Chemical Reviews* **1995**, *95*, 661–666.
- [39] F. Zaera, *Chemical Society Reviews* **2013**, *42*, 2746–2762.
- [40] E. K. Rideal, *Nature* **1928**, *122*, 589–590.
- [41] C. A. Tolman, J. P. Jesson, *American Association for the Advancement of Science* **1973**, *181*, 501–505.
- [42] F. Mathey, *Transition Metal Organometallic Chemistry*, Springer, Singapore, **2013**.
- [43] S. Singh, P. Tandon, *Journal of Energy and Chemical Engineering(JECE)* **2014**, *2*, 106–115.
- [44] H. Tsunoyama, N. Ichikuni, H. Sakurai, T. Tsukuda, *Journal of the American Chemical Society* **2009**, *131*, 7086–7093.
- [45] J. Mielby, A. J. Kunov-Kruse, S. Kegnaes, *Journal of Catalysis* **2017**, *345*, 149–156.

- [46] T. S. Rodrigues, A. G. Da Silva, P. H. Camargo, *Journal of Materials Chemistry A* **2019**, *7*, 5857–5874.
- [47] Q. L. Zhu, N. Tsumori, Q. Xu, *Journal of the American Chemical Society* **2015**, *137*, 11743–11748.
- [48] P. Kattan, *Ratio of Surface Area to Volume in Nanotechnology and Nanoscience*, Petra Books, **2011**.
- [49] I. V. Zibareva, L. Y. Ilina, A. A. Vedyagin, *Reaction Kinetics Mechanisms and Catalysis* **2019**, *127*, 19–24.
- [50] C. Xia, J. Chen, F. Cui, X. Zhang, H. Kang, Z. Huang, *Chemistry of Materials* **2008**, *20*, 5090–5099.
- [51] L. Melo, Y. Díaz, M. Mediavilla, A. Llanos, A. Albornoz, J. L. Brito, *Catalysis Today* **2008**, *133–135*, 99–105.
- [52] M. Shamzhy, M. Opanasenko, P. Concepción, A. Martínez, *Chemical Society Reviews* **2019**, *48*, 1095–1149.
- [53] X. Liu, W. Zhou, Y. Yang, K. Cheng, J. Kang, L. Zhang, G. Zhang, X. Min, Q. Zhang, Y. Wang, *Chemical Science* **2018**, *9*, 4708–4718.
- [54] P. Munnik, P. E. De Jongh, K. P. De Jong, *Chemical Reviews* **2015**, *115*, 6687–6718.
- [55] J. Kärger, D. Freude, *Chemical Engineering and Technology* **2002**, *25*, 769–778.
- [56] D. H. Olson, G. T. Kokotailo, S. L. Lawton, *Journal of Physical Chemistry* **1981**, *85*, 2238–2243.
- [57] L. Zoubida, B. Hichem, The Nanostructure Zeolites MFI-Type ZSM5, **2018**, <https://www.intechopen.com/books/nanocrystals-and-nanostructures/the-nanostructure-zeolites-mfi-type-zsm5> (visited on 02/10/2020).
- [58] C. B. L. B. M. D. Olson, *Atlas of Zeolite Framework Types 6th Edition*, Elsevier Science, **2007**.
- [59] D. R. Gama, “Investigations of the Long Term Catalytic Activity and Stability of Zeolite-based Catalysts in the Conversion of Dissertation for the degree of Philosophiae Doctor Faculty of Mathematics and Natural Sciences”, PhD thesis, University of Oslo, **2017**.

- [60] K. P. Prasanth, R. S. Pillai, H. C. Bajaj, R. V. Jasra, H. D. Chung, T. H. Kim, S. D. Song, *International Journal of Hydrogen Energy* **2008**, *33*, 735–745.
- [61] J. Weikamp, *Solid State Ionics* **2000**, *131*, 175–188.
- [62] C. T. Kresge, S. S. Dhingra, *Kirk-Othmer Encyclopedia of Chemical Technology*, **2004**.
- [63] Z. S. Čejka Jiří, Corma Avelino, *Zeolites and Catalysis: Synthesis, Reactions and Applications*, Wiley-VCH, **2010**.
- [64] Y. Tao, H. Kanoh, L. Abrams, K. Kaneko, *Chemical Reviews* **2006**, *106*, 896–910.
- [65] C. Vercaemst, “Isomeric Olefinic Periodic Mesoporous Organosilicas : An Emerging Class of Versatile Nano- materials”, PhD thesis, Ghent University, **2009**.
- [66] M. Hartmann, A. Machoke, W. Schwieger, *Chemical Society reviews* **2016**, *45*, 3313–3330.
- [67] J. J. J. Yu, A. Corma, *Angew. Chemie* **2010**, *49*, 3120–3145.
- [68] K. Möller, T. Bein, *Chem. Soc. Rev.* **2013**, *42*, 3689–3707.
- [69] J. O. Abildstrøm, M. Kegnæs, G. Hytoft, J. Mielby, S. Kegnæs, *Microporous and Mesoporous Materials* **2016**, *225*, 232–237.
- [70] M. G. Ruiz, D. A. Casados, J. A. Pliego, C. M. Álvarez, E. S. de Andrés, D. S. Tartalo, R. S. Vaque, M. G. Casas, *Reaction Kinetics Mechanisms and Catalysis* **2020**, 471–490.
- [71] C. Huertas, “Improvement of the methanol-to-hydrocarbons catalytic performance for one-dimensional zeolites obtained by post-synthetic modifications”, PhD thesis, University of Oslo, **2017**.
- [72] A. Silvestre-Albero, A. Grau-Atienza, E. Serrano, J. García-Martínez, J. Silvestre-Albero, *Catalysis Communications* **2014**, *44*, 35–39.
- [73] D. Verboekend, J. Pérez-Ramírez, *Catalysis Science and Technology* **2011**, *1*, 879–890.
- [74] L. S. da Silva, C. A. Araki, S. M. P. Marcucci, V. L. d. S. T. da Silva, P. A. Arroyo, *Materials Research* **2019**, *22*.
- [75] K. Wang, M. Dong, J. Li, P. Liu, K. Zhang, J. Wang, W. Fan, *Catalysis Science and Technology* **2017**, *7*, 560–564.

- [76] J. Pérez-Ramírez, S. Abelló, A. Bonilla, J. C. Groen, *Advanced Functional Materials* **2009**, *19*, 164–172.
- [77] I. I. Ivanova, E. E. Knyazeva, *Chemical Society Reviews* **2013**, *42*, 3671–3688.
- [78] P. Zhang, L. Wang, S. Yang, J. A. Schott, X. Liu, S. M. Mahurin, C. Huang, Y. Zhang, P. F. Fulvio, M. F. Chisholm, S. Dai, *Nature Communications* **2017**, *8*, 1–10.
- [79] J. Lee, J. Kim, T. Hyeon, *Advanced Materials* **2006**, *18*, 2073–2094.
- [80] A. Eftekhari, Z. Fan, *Materials Chemistry Frontiers* **2017**, *1*, 1001–1027.
- [81] N. Yoshida, Y. Hirota, Y. Uchida, T. Asada, N. Kobayashi, N. Nishiyama, *Microporous and Mesoporous Materials* **2018**, *272*, 217–221.
- [82] X. H. Li, K. Wan, Q. B. Liu, J. H. Piao, Y. Y. Zheng, Z. X. Liang, *Cuihua Xuebao/Chinese Journal of Catalysis* **2016**, *37*, 1562–1567.
- [83] S. Tanaka, N. Nishiyama, Y. Egashira, K. Ueyama, *Chemical Communications* **2005**, 2125–2127.
- [84] H. Song, Z. Liu, H. Gai, Y. Wang, L. Qiao, C. Zhong, X. Yin, M. Xiao, *Frontiers in Chemistry* **2019**, *7*, 1–12.
- [85] G. Shen, X. Sun, H. Zhang, Y. Liu, J. Zhang, A. Meka, L. Zhou, C. Yu, **2015**, 24041–24048.
- [86] G. H. Wang, Z. Cao, D. Gu, N. Pfänder, A. C. Swertz, B. Spliethoff, H. J. Bongard, C. Weidenthaler, W. Schmidt, R. Rinaldi, F. Schüth, *Angewandte Chemie - International Edition* **2016**, *55*, 8850–8855.
- [87] A. H. Lu, F. Schüth, *Advanced Materials* **2006**, *18*, 1793–1805.
- [88] F. Zaera, Z. Ma, *Characterization of Heterogeneous Catalysts*, CRC Press, **2006**, pp. 1–38.
- [89] M. Thommes, K. Kaneko, A. V. Neimark, J. P. Olivier, F. Rodriguez-Reinoso, J. Rouquerol, K. S. Sing, *Pure and Applied Chemistry* **2015**, *87*, 1051–1069.
- [90] F. J. Sotomayor, K. A. Cychosz, M. Thommes, *Acc. Mater. Surf. Res* **2018**, *3*, 34–50.
- [91] D. Dollimore, P. Spooner, A. Turner, *Surface Technology* **1976**, *4*, 121–160.
- [92] A. Galarneau, F. Villemot, J. Rodriguez, F. Fajula, B. Coasne, *Langmuir* **2014**, *30*, 13266–13274.

- [93] A. Kaech, *Center for Microscopy and Image Analysis* **2002**, 1–26.
- [94] W. Zhou, R. Apkarian, Z. L. Wang, D. Joy, *Scanning Microscopy for Nanotechnology: Techniques and Applications* **2007**, 1–40.
- [95] A. Nanakoudis, ThermoFisher Scientific, **2019**, <https://www.thermofisher.com/blog/microscopy/sem-types-electrons-and-the-information-they-provide/> (visited on 02/10/2020).
- [96] M. Intelligence, Single walled carbon nanotube, **2020**, <https://www.nanoshel.com/product/single-walled-carbon-nanotube> (visited on 02/10/2020).
- [97] N. Marturi, “Vision and visual servoing for nanomanipulation and nanocharacterization in scanning electron microscope.”, PhD thesis, University of Franche-Comté, **2013**.
- [98] J. J. Mielby, “Selective Oxidations using Nanostructured Heterogeneous Catalysts”, PhD thesis, Technical University of Denmark, **2014**.
- [99] S. D. Findlay, N. Shibata, H. Sawada, E. Okunishi, Y. Kondo, Y. Ikuhara, *Ultramicroscopy* **2010**, *110*, 903–923.
- [100] S. Bals, B. Kabius, M. Haider, V. Radmilovic, C. Kisielowski, **2004**, *130*, 675–680.
- [101] M. Fadoni, L. Lucarelli, *Temperature programmed desorption, reduction, oxidation and flow chemisorption for the characterisation of heterogeneous catalysts. Theoretical aspects, instrumentation and applications*, Elsevier, **1999**, pp. 177–225.
- [102] Z. P. GmbH, Temperature-programmed Desorption / Reduction / Oxidation (TPD / TPR / TPO) and Pulse-Sorption / Chemisorption, **2018**, http://www.zeta-pa.de/pics/ZetA-tpd-info_e.pdf (visited on 02/10/2020).
- [103] F. Hermes, M. Bertmer, L. Rodrı, U. Simon, E. Rodrı, **2007**, *328*, 174–182.
- [104] T. N. Abduljabbar, B. L. Sharp, H. J. Reid, N. Barzegar-Befroeid, T. Peto, I. Lengyel, *Talanta* **2019**, *204*, 663–669.
- [105] C. Grochowski, E. Blicharska, P. Krukow, K. Jonak, M. Maciejewski, D. Szczepanek, K. Jonak, J. Flieger, R. Maciejewski, *Frontiers in Chemistry* **2019**, *7*, 115.
- [106] M. Thompson, CHNS Elemental Analysers, tech. rep., Analytical Methods Committee, The Royal Society of Chemistry, **2008**.

- [107] V. P. Fadeeva, V. D. Tikhova, O. N. Nikulicheva, **2008**, *63*, 1094–1106.
- [108] S. Hanukovich, A. Dang, P. Christopher, *ACS Catalysis* **2019**, *9*, 3537–3550.
- [109] M. Navlani-garcía, K. Mori, Y. Kuwahara, H. Yamashita, *NPG Asia Materials* **2018**, 277–292.
- [110] M. Navlani-García, K. Mori, D. Salinas-Torres, Y. Kuwahara, H. Yamashita, *Frontiers in Materials* **2019**, *6*, 1–18.
- [111] A. Kumar, R. Prasad, Y. C. Sharma, *International Journal of Environmental Research and Development* **2014**, *4*, 2249–3131.
- [112] Y. Ren, Y. Wang, X. Li, Z. Zhang, Q. Chi, *New Journal of Chemistry* **2018**, *42*, 16694–16702.
- [113] J. Oskar, “Design of porous nanostructured solid catalysts”, PhD thesis, Technical University of Denmark, **2016**.
- [114] F. Nitze, “Synthesis and characterization of palladium based carbon nanostructure-composites and their clean-energy application”, PhD thesis, Umeå University, **2013**.
- [115] T. Bhowmik, M. K. Kundu, S. Barman, *ACS Catalysis* **2016**, *6*, 1929–1941.
- [116] D. S. Singh, A. Singh, A. Kumar, *Catalysis Science Technology* **2015**, *6*, 1–26.
- [117] J. R. Salge, G. A. Deluga, L. D. Schmidt, *Journal of Catalysis* **2005**, *235*, 69–78.
- [118] I. I. Soykal, H. Sohn, U. S. Ozkan, *ACS Catalysis* **2012**, *2*, 2335–2348.
- [119] K.-w. Huang, *ACS Energy Letters* **2017**, *2*, 188–195.
- [120] N. Onishi, M. Iguchi, X. Yang, R. Kanega, H. Kawanami, Q. Xu, Y. Himeda, *Advanced Energy Materials* **2019**, *9*, 1–14.
- [121] E. Gianotti, M. Taillades-Jacquin, J. Rozière, D. J. Jones, *ACS Catalysis* **2018**, *8*, 4660–4680.
- [122] K. M. Thomas, *Journal of the Chemical Society. Dalton Transactions* **2009**, 1487–1505.
- [123] B. Sakintuna, F. Lamari-darkrim, M. Hirscher, *International Journal of Hydrogen Energy* **2007**, *32*, 1121–1140.
- [124] N. T. Mahendra Yadav, Ashish Kumar Singh, Q. Xu, *Journal of Materials Chemistry* **2012**, 19146–19150.

- [125] C. H. Christensen, R. Z. Sørensen, T. Johannessen, U. J. Quaade, K. Honkala, T. D. Elmøe, R. Køhler, J. K. Nørskov, *Journal of Materials Chemistry* **2005**, *15*, 4106–4108.
- [126] M. Trincado, D. Banerjee, H. Grützmacher, *Energy and Environmental Science* **2014**, *7*, 2464–2503.
- [127] A. Gallas-hulin, J. Mielby, S. Kegnæs, *ChemistrySelect* **2016**, *1*, 3942–3945.
- [128] P. Zhao, W. Xu, D. Yang, W. Luo, G. Cheng, *ChemistrySelect* **2016**, *1*, 1400–1404.
- [129] N. Onishi, G. Laurenczy, M. Beller, Y. Himeda, *Coordination Chemistry Reviews* **2018**, *373*, 317–332.
- [130] W. Ye, W. Pei, S. Zhou, H. Huang, Q. Li, J. Zhao, *Journal of Materials Chemistry A* **2019**, 10363–10371.
- [131] M. Navlani-García, M. Martis, D. Lozano-Castelló, D. Cazorla-Amorós, K. Mori, H. Yamashita, *Catalysis Science and Technology* **2015**, *5*, 364–371.
- [132] K. Tedsree, T. Li, S. Jones, C. Wong, A. Chan, K. Man, K. Yu, P. A. J. Bagot, E. A. Marquis, G. D. W. Smith, S. Chi, E. Tsang, *Nature nanotechnology* **2011**, *6*, 2–7.
- [133] X. Wang, Q. Meng, L. Gao, Z. Jin, J. Ge, *International Journal of Hydrogen Energy* **2018**, *43*, 7055–7071.
- [134] N. Hoshi, M. Nakamura, K. Kida, *Electrochemistry Communications* **2007**, *9*, 279–282.
- [135] J. J. A. Celaje, Z. Lu, E. A. Kedzie, N. J. Terrile, J. N. Lo, T. J. Williams, **2016**, 1–6.
- [136] X. Wang, Q. Meng, L. Gao, J. Liu, J. Ge, *International Journal of Hydrogen Energy* **2019**, *44*, 28402–28408.
- [137] Z. Xing, Z. Guo, X. Chen, P. Zhang, W. Yang, **2019**, 588–592.
- [138] X. Yang, P. Pachfule, Y. Chen, Q. Xu, *Chemical Communications* **2016**, *52*, 4171–4174.
- [139] W.-y. Yu, G. M. Mullen, D. W. Flaherty, C. B. Mullins, *Journal of the American Chemical Society* **2014**, *136*, 11070–11078.
- [140] Z. Zhang, Y. Luo, S. Liu, Q. Yao, S. Qing, Z.-h. Lu, *Journal of Materials Chemistry A* **2019**, 21438–21446.

- [141] M. Martis, K. Mori, K. Fujiwara, W.-s. Ahn, H. Yamashita, *J. Phys. Chem. C* **2013**, *117*, 22805–22810.
- [142] J. Cheng, X. Gu, X. Sheng, P. Liu, H. Su, *Journal of Materials Chemistry A* **2016**, 1887–1894.
- [143] Y. Wang, Y. Qi, D. Zhang, C. Liu, *J. Phys. Chem.* **2014**, *118*, 2067–2076.
- [144] N. Wang, Q. Sun, R. Bai, X. Li, G. Guo, J. Yu, *Journal of the American Chemical Society* **2016**, *138*, 7484–7487.
- [145] D. W. Yuan, Z. R. Liu, *Journal of Power Sources* **2013**, *224*, 241–249.
- [146] Y. Karatas, A. Bulut, M. Yurderi, I. Efekan, O. Alal, M. Gulcan, M. Celebi, H. Kivrak, M. Kaya, M. Zahmakiran, *"Applied Catalysis B Environmental"* **2016**, *180*, 586–595.
- [147] C. Hu, X. Mu, J. Fan, H. Ma, X. Zhao, G. Chen, Z. Zhou, N. Zheng, *ChemNanoMat* **2016**, *2*, 28–32.
- [148] C. Hsu, C. Huang, Y. Hao, F. Liu, *Journal of Power Sources* **2013**, *243*, 343–349.
- [149] S. Wu, F. Yang, P. Sun, T. Chen, *RSC Advances* **2014**, 44500–44503.
- [150] Y. Jiang, M. Chen, Y. Yang, X. Zhang, *Nanotechnology* **2018**, *29*, 335402.
- [151] O. Kadlec, M. M. Dubinin, *Journal of Colloid And Interface Science* **1969**, *31*, 479–489.
- [152] J. Mielby, J. O. Abildstrøm, F. Wang, T. Kasama, C. Weidenthaler, S. Kegnaes, *Angewandte Chemie - International Edition* **2014**, *53*, 12513–12516.
- [153] Y. Jiang, X. Fan, M. Chen, X. Xiao, Y. Zhang, C. Wang, L. Chen, *J. Phys. Chem* **2018**, *122*, 4792–4801.
- [154] S. Seraj, P. Kunal, H. Li, G. Henkelman, S. M. Humphrey, C. J. Werth, *ACS Catalysis*, *7*, 3268–276.
- [155] P. D. Srinivasan, B. S. Patil, H. Zhu, J. J. Bravo-Suárez, *React. Chem. Eng.* **2019**, *4*, 862–883.
- [156] D. A. Bulushev, M. Zacharska, S. Beloshapkin, Y. Guo, I. Yuranov, *Applied Catalysis A General* **2018**, *561*, 96–103.
- [157] M. Gulcan, E. Ozensoy, M. Zahmakiran, *ACS Catalysis* **2015**, *5*, 6099–6110.
- [158] W. E. Taifan, G. X. Yan, J. Baltrusaitis, *Catalysis Science and Technology* **2017**, *7*, 4648–4668.

- [159] M. Watch, Acetaldehyde Market 2019 Global Industry Demand, Recent Trends, Size and Share Estimation by 2025 with Top Players - ResearchReportsWorld.com ‘, **2010**, <https://www.marketwatch.com/press-release/acetaldehyde-market-2019-global-industry-demand-recent-trends-size-and-share-estimation-by-2025-with-top-players---researchreportsworldcom-2019-04-15> (visited on 02/10/2020).
- [160] U. N. L. of Medicine, COMPOUND SUMMARY Acetaldehyde, **2019**, <https://pubchem.ncbi.nlm.nih.gov/compound/Acetaldehyde> (visited on 02/10/2020).
- [161] G. Garbarino, P. Riani, M. Villa García, E. Finocchio, V. Sanchez Escribano, G. Busca, *Catalysis Today* **2019**, 0–1.
- [162] W. D. Lu, Q. N. Wang, L. He, W. C. Li, F. Schüth, A. H. Lu, *ChemNanoMat* **2018**, *4*, 505–509.
- [163] A. Rodriguez-Gomez, J. P. Holgado, A. Caballero, *ACS Catalysis* **2017**, *7*, 5243–5247.
- [164] J. M. R. Gallo, U. Schuchardt, *Journal of the Brazilian Chemical Society* **2014**, *25*, 2229–2243.
- [165] D. I. Enache, J. K. Edwards, P. Landon, B. Solsona-espriu, A. F. Carley, A. A. Herzing, M. Watanabe, C. J. Kiely, D. W. Knight, G. J. Hutchings, *Science* **2006**, *311*, 362–366.
- [166] G. M. Mullen, E. J. Evans, I. Sabzevari, B. E. Long, K. Alhazmi, B. D. Chandler, C. B. Mullins, *ACS Catalysis* **2017**, *7*, 1216–1226.
- [167] E. Santacesaria, G. Carotenuto, R. Tesser, M. Di Serio, *Chemical Engineering Journal* **2012**, *179*, 209–220.
- [168] A. Segawa, A. Nakashima, R. Nojima, N. Yoshida, M. Okamoto, *Industrial and Engineering Chemistry Research* **2018**, *57*, 11852–11857.
- [169] S. Velu, L. Wang, M. Okazaki, K. Suzuki, S. Tomura, *Microporous and Mesoporous Materials* **2002**, *54*, 113–126.
- [170] M. Ohira, H. Liu, D. He, Y. Hirata, M. Sano, T. Suzuki, T. Miyake, *Journal of the Japan Petroleum Institute* **2018**, *61*, 205–212.
- [171] F. Zaccheria, N. Ravasio, R. Psaro, A. Fusi, *Chemistry - A European Journal* **2006**, *12*, 6426–6431.

- [172] P. Zhang, Q. N. Wang, X. Yang, D. Wang, W. C. Li, Y. Zheng, M. Chen, A. H. Lu, *ChemCatChem* **2017**, *9*, 505–510.
- [173] E. A. Ponomareva, I. V. Krasnikova, E. V. Egorova, V. Mishakov, A. A. Vedyagin, *Mendeleev Commun* **2017**, *27*, 210–212.
- [174] M. V. Morales, E. Asedegbega-Nieto, B. Bachiller-Baeza, A. Guerrero-Ruiz, *Carbon* **2016**, *102*, 426–436.
- [175] D. A. Bulushev, A. L. Chuvilin, V. I. Sobolev, S. G. Stolyarova, Y. V. Shubin, I. P. Asanov, A. V. Ishchenko, G. Magnani, M. Riccò, A. V. Okotrub, L. G. Bulusheva, *Journal of Materials Chemistry A* **2017**, *5*, 10574–10583.
- [176] P. Zhang, Y. Gong, H. Li, Z. Chen, Y. Wang, *Nature Communications* **2013**, *4*, 1593.
- [177] Y. Xie, C. Zhang, X. He, J. W. Su, T. Parker, T. White, M. Griep, J. Lin, *Applied Surface Science* **2019**, *464*, 344–350.
- [178] J. Mondal, R. Gomes, A. Modak, A. Bhaumik, *Recyclable Catalysis* **2013**, *1*, 9–33.
- [179] S. S. Park, S. W. Chu, C. Xue, D. Zhao, C. S. Ha, *Journal of Materials Chemistry* **2011**, *21*, 10801–10807.
- [180] A. Vinu, *Advanced Functional Materials* **2008**, *18*, 816–827.
- [181] G. D. M. Dabera, M. Walker, A. M. Sanchez, H. J. Pereira, R. Beanland, R. A. Hatton, *Nature Communications* **2017**, *8*, 1894.
- [182] Y. Gao, J. Li, L. Wang, Y. Hou, X. Lai, W. Zhang, X. Chen, P. Zhang, Y. Huang, B. Yue, *Nanotechnology* **2020**, *31*, 055705.
- [183] J. M. Conesa, M. V. Morales, C. López-Olmos, I. Rodríguez-Ramos, A. Guerrero-Ruiz, *Applied Catalysis A: General* **2019**, *576*, 54–64.
- [184] A. Kumar, A. Ashok, R. R. Bhosale, M. A. H. Saleh, F. A. Almomani, M. Al-Marri, M. M. Khader, F. Tarlochan, *Catalysis Letters* **2016**, *146*, 778–787.
- [185] J. Llorca, N. Homs, P. Ramirez de la Piscina, *Journal of Catalysis* **2004**, *227*, 556–560.
- [186] T. Yan, W. Dai, G. Wu, S. Lang, M. Hunger, N. Guan, L. Li, *ACS Catalysis* **2018**, *8*, 2760–2773.
- [187] A. G. Sato, D. P. Volanti, I. C. De Freitas, E. Longo, J. M. C. Bueno, *Catalysis Communications* **2012**, *26*, 122–126.

- [188] G. M. Cabello González, P. Concepción, A. L. Villanueva Perales, A. Martínez, M. Campoy, F. Vidal-Barrero, *Fuel Processing Technology* **2019**, *193*, 263–272.
- [189] I. A. for Research on Cancer, *Chemical Agents and Related Occupations*, Vol. 100F, **2012**.
- [190] U. N. L. of Medicine, COMPOUND SUMMARY 1,3-Butadiene, **2019**, <https://pubchem.ncbi.nlm.nih.gov/compound/BUTADIENE> (visited on 02/10/2020).
- [191] Z. Zhang, L. Zhang, Y. Li, H. Xu, *Polymer* **2005**, *46*, 129–136.
- [192] M. Intelligence, BUTADIENE MARKET - GROWTH, TRENDS, AND FORECAST (2020 - 2025), **2020**, <https://www.mordorintelligence.com/industry-reports/butadiene-market> (visited on 02/10/2020).
- [193] W. C. White, *Chemico-Biological Interactions* **2007**, *166*, 10–14.
- [194] G. Pomalaza, M. Capron, V. Ordonsky, F. Dumeignil, *Catalysts* **2016**, *6* (12), 203.
- [195] N. Rahimi, R. Karimzadeh, *Applied Catalysis A: General* **2011**, *398*, 1–17.
- [196] J. C. Bauer, G. M. Veith, L. F. Allard, Y. Oyola, S. H. Overbury, S. Dai, *ACS Catalysis* **2012**, *2*, 2537–2546.
- [197] J. Rass-Hansen, H. Falsig, B. Jørgensen, C. Christensen, *Journal of Chemical Technology and Biotechnology* **2007**, *82*, 329–333.
- [198] S. Shylesh, A. A. Gokhale, C. D. Scown, *ChemSusChem: Energy and Materials* **2016**, 1462–1472.
- [199] M. M. Kurmach, O. V. Larina, P. I. Kyriienko, P. S. Yaremov, V. V. Trachevsky, O. V. Shvets, S. O. Soloviev, *ChemistrySelect* **2018**, *3*, 8539–8546.
- [200] A. Klein, K. Keisers, R. Palkovits, *Applied Catalysis A: General* **2016**, *514*, 192–202.
- [201] N. Godová, B. Horváth, *Acta Chimica Slovaca* **2018**, *11*, 11–20.
- [202] C. Angelici, M. E. Z. Velthoen, B. M. Weckhuysen, P. C. A. Bruijnincx, **2015**, 2869–2879.
- [203] S. V. Lebedev, *Chem.-Ztg.* **1936**, *60*, 313–316.
- [204] Q. Zhu, B. Wang, T. Tan, *ACS Sustainable Chem. Eng.* **2017**, 722–733.
- [205] C. Angelici, M. E. Z. Velthoen, B. M. Weckhuysen, P. C. A. Bruijnincx, *Royal Society of Chemistry* **2015**, 2869–2879.

- [206] S. K. Bhattacharyya, N. D. Ganguly, *Journal of Applied Chemistry* **2007**, *12*, 105–110.
- [207] G. O. Ezinkwo, V. P. Tretyakov, A. Aliyu, *ChemBioEng Reviews* **2014**, 194–203.
- [208] O. V. Larina, I. M. Remezovskyi, P. I. Kyriienko, S. O. Soloviev, S. M. Orlyk, *Reaction Kinetics Mechanisms and Catalysis* **2019**, *127*, 903–915.
- [209] W. Dai, S. Zhang, Z. Yu, T. Yan, G. Wu, N. Guan, L. Li, *ACS Catalysis* **2017**, *7*, 3703–3706.
- [210] T. Liang, S. Fadaeeraeyeni, J. Shan, T. Li, H. Wang, J. Cheng, H. Toghiani, Y. Xiang, *Industrial and Engineering Chemistry Research* **2019**, *58*, 17699–17708.
- [211] F. Goodarzi, R. P. Thumbayil, K. Enemark-Rasmussen, J. Mielby, T. T. Nguyen, P. Beato, F. Joensen, S. Kegnæs, *ChemCatChem* **2020**, 1–9.
- [212] M. Orazov, M. E. Davis, *Chemical Science* **2016**, *7*, 2264–2274.
- [213] C. Angelici, B. M. Weckhuysen, P. C. Bruijninx, *ChemSusChem* **2013**, *6*, 1595–1614.
- [214] T. De Baerdemaeker, M. Feyen, U. Müller, B. Yilmaz, F. S. Xiao, W. Zhang, T. Yokoi, X. Bao, H. Gies, D. E. De Vos, *ACS Catalysis* **2015**, *5*, 3393–3397.
- [215] P. Patnaik, *Methyl Isobutyl Ketone*, Lewis Publishers, **1997**, pp. 4–5.
- [216] F. Winter, “Hydrotalcite-Based Catalysts for the Synthesis of Methyl Isobutyl Ketone”, PhD thesis, Utrecht University, **1976**.
- [217] J. I. Di Cosimo, G. Torres, C. R. Apesteguía, *Journal of Catalysis* **2002**, *208*, 114–123.
- [218] D. Bomboş, F. Bacalum, M. Bomboş, G. Bozga, *Revue Roumaine de Chimie* **2006**, *51*, 69–74.
- [219] G. Waters, O. Richter, B. Kraushaar-Czarnetzki, *Industrial and Engineering Chemistry Research* **2006**, *45*, 5701–5707.
- [220] S.-m. Yang, Y. M. Wu, *Applied Catalysis A : General* **2000**, *192*, 211–220.
- [221] M. Liu, G. Liu, Y. Zhou, K. Han, H. Ye, *Journal of Molecular Catalysis A: Chemical* **2015**, *408*, 85–90.
- [222] H. Duan, Z. Wang, L. Cui, B. Lin, Y. Zhou, *Industrial and Engineering Chemistry Research* **2018**, *57*, 12358–12366.

- [223] D. Bombos, G. Bozga, M. Bombos, A. Stefan, I. Stanciu, *Chemical Papers-Slovak Academy of Sciences* **2000**, *54*, 171–176.
- [224] Y. Pan, B. Yuan, Y. Li, D. He, *Chemical Communications* **2010**, *46*, 2280–2282.
- [225] J. J. Gamman, S. D. Jackson, F. A. Wigzell, *Ind. Eng. Chem. Res.* **2010**, *49*, 8439–8443.
- [226] A. A. Al-rabiah, *Synthesis and Use of a Nano-Crystalline Zinc Chromite Catalyst, Compromising Nano-Palladium*, EP Patent : 2418017A1, **2016**.
- [227] Y. Liu, K. Sun, X. Xu, X. Wang, *Catalysis Communications* **2010**, *11*, 322–325.
- [228] P. Y. Chen, S. J. Chu, W. C. Lin, K. C. Wu, C. L. Yang, *Studies in Surface Science and Catalysis* **1994**, *83*, 481–488.
- [229] B. Y. Coh, J. M. Hur, H. I. Lee, *Korean Journal of Chemical Engineering* **1997**, *14*, 464–468.
- [230] E. F. Kozhevnikova, I. V. Kozhevnikov, *Journal of Catalysis* **2006**, *238*, 286–292.
- [231] F. Al-Wadaani, E. F. Kozhevnikova, I. V. Kozhevnikov, *Journal of Catalysis* **2008**, *257*, 199–205.
- [232] J. J. Gamman, S. D. Jackson, F. A. Wigzell, *Industrial & Engineering Chemistry Research* **2010**, *49*, 8439–8443.
- [233] J. B. Higgins, M. M. J. Treacy, *Collection of Simulated XRD Powder Patterns for Zeolites-5th Edition*, Elsevier Science, **2007**.
- [234] Y. Z. Chen, B. J. Liaw, H. R. Tan, K. L. Shen, *Applied Catalysis A: General* **2001**, *205*, 61–69.

APPENDIX A

Publications and Disseminations

Publications

1. Pulikkal Thumbayil. Rouzana, Mielby. Jerrik and Kegnæs. Søren, “Pd Nanoparticles Encapsulated in Mesoporous HZSM-5 Zeolite for Selective One-Step Conversion of Acetone to Methyl Isobutyl Ketone”. *Topics in Catalysis*, 10.1007/s11244-019-01153-6.
2. Goodarzi. Farnoosh, Pulikkal Thumbayil. Rouzana, Enemark-Rasmussen. Kasper, Mielby. Jerrik, Nguyen. Thoa, Beato. Pablo, Joensen. Finn and Kegnæs. Søren, “Enhanced catalytic performance of Zn-containing HZSM-5 upon selective desilication in ethane dehydroaromatization process”, *ChemCatChem*, 10.1002/cctc.201902123.
3. Pulikkal Thumbayil. Rouzana, Benjamin Christensen. David, Mielby. Jerrik, Kegnæs. Søren, “Dehydrogenation of bioethanol using Cu nanoparticles supported on N-doped ordered mesoporous carbon”, *manuscript*.

Conference Proceedings

1. Highly Selective Dehydrogenation of Bioethanol to Acetaldehyde using Copper Catalyst Supported on Mesoporous Carbon, Pulikkal Thumbayil, Rouzana; Benjamin Christensen, David; Mielby, Jerrik; Kegnæs, Søren, 14th European Congress on Catalysis, EuropaCat, Aachen, **2019**.
2. Selective Dehydrogenation of Bioethanol using Copper Supported on Mesoporous Carbon, Pulikkal Thumbayil, Rouzana; Mielby, Jerrik; Kegnæs, Søren, PhD Symposium, DTU Denmark **2019**.

3. Conversion of Acetone to Methyl Isobutyl Ketone using a Bifunctional Zeolite Catalyst, Pulikkal Thumbayil, Rouzana; Mielby, Jerrik; Kegnæs, Søren, 18th Nordic Symposium on Catalysis (NSC), **2018**.
4. Highly dispersed heterogeneous nanocatalyst for the synthesis of methyl isobutyl ketone, Pulikkal Thumbayil, Rouzana; Mielby, Jerrik; Kegnæs, Søren, PhD Symposium, DTU Denmark, **2018**.
5. Conversion of acetone to methyl isobutyl ketone using a bifunctional zeolite catalyst, Pulikkal Thumbayil, Rouzana; Mielby, Jerrik; Kegnæs, Søren, 13th European Congress on Catalysis, EuropaCat Florence, **2017**.
6. Encapsulated Palladium Nanoparticles for the Synthesis of Methyl Isobutyl Ketone, Pulikkal Thumbayil, Rouzana; Mielby, Jerrik; Kegnæs, Søren, EuCheMS Inorganic Chemistry Conference, **2017**.
7. Selective catalysis with metal nanoparticles in porous materials, Pulikkal Thumbayil, Rouzana; Mielby, Jerrik; Kegnæs, Søren, PhD Symposium, DTU Denmark, **2016**.

APPENDIX B

Declaration of Co-authorship

Paper 1

Pulikkal Thumbayil. Rouzana, Mielby. Jerrik and Kegnæs. Søren, “Pd Nanoparticles Encapsulated in Mesoporous HZSM-5 Zeolite for Selective One-Step Conversion of Acetone to Methyl Isobutyl Ketone”. *Topics in Catalysis*, 10.1007/s11244-019-01153-6.

Paper 2

Pulikkal Thumbayil. Rouzana, Benjamin Christensen. David, Mielby. Jerrik, Kegnæs. Søren, “Dehydrogenation of bioethanol using Cu nanoparticles supported on N-doped ordered mesoporous carbon”, *manuscript*.

Declaration of co-authorship at DTU

If a PhD thesis contains articles (i.e. published journal and conference articles, unpublished manuscripts, chapters, etc.) written in collaboration with other researchers, a co-author statement verifying the PhD student's contribution to each article should be made.

If an article is written in collaboration with three or less researchers (including the PhD student), all researchers must sign the statement. However, if an article has more than three authors the statement may be signed by a representative sample, cf. article 12, section 4 and 5 of the Ministerial Order No. 1039, 27 August 2013. A representative sample consists of minimum three authors, which is comprised of the first author, the corresponding author, the senior author, and 1-2 authors (preferably international/non-supervisor authors).

DTU has implemented the Danish Code of Conduct for Research Integrity, which states the following regarding attribution of authorship:

"Attribution of authorship should in general be based on criteria a-d adopted from the Vancouver guidelines¹, and all individuals who meet these criteria should be recognized as authors:

- a. Substantial contributions to the conception or design of the work, or the acquisition, analysis, or interpretation of data for the work, *and*
- b. drafting the work or revising it critically for important intellectual content, *and*
- c. final approval of the version to be published, *and*
- d. agreement to be accountable for all aspects of the work in ensuring that questions related to the accuracy or integrity of any part of the work are appropriately investigated and resolved."²

For more information regarding definition of co-authorship and examples of authorship conflicts, we refer to DTU Code of Conduct for Research Integrity (pp. 19-22).

By signing this declaration, co-authors permit the PhD student to reuse whole or parts of co-authored articles in their PhD thesis, under the condition that co-authors are acknowledged in connection with the reused text or figure.

It is **important** to note that it is the responsibility of the PhD student to obtain permission from the publisher to use the article in the PhD thesis³

¹ International Committee of Medical Journal Editors – Recommendations for the Conduct, Reporting, Editing, and Publication of Scholarly Work in Medical Journals, updated December 2016

² DTU Code of Conduct for Research Integrity (E-book p. 19)

³ Many journals will allow you to use only the post-print version of your article, meaning the accepted version of the article, without the publisher's final formatting. In the event that your article is submitted, but still under review, you should of course use the latest submitted version of your article in your thesis. Always remember to check your publisher's guidelines on reuse of published articles. Most journals, unless open access, have an embargo period on published articles, meaning that within this period you cannot freely use the article. Check your publisher's rules on this issue.

Office for PhD and Continuing Education
March 2020 | page 2/3

Technical University
of Denmark



Title of article		
Pd Nanoparticles Encapsulated in Mesoporous HZSM-5 Zeolite for Selective One-Step Conversion of Acetone to Methyl Isobutyl Ketone		
Journal/conference		
Journal		
Author(s)		
Rouzana Pulikkal Thumbayil, Jerrik Mielby, Søren Kegnæs		
Name (capital letters) and signature of PhD student		
ROUZANA PULIKKAL THUMBAYIL		
PhD student's date of birth		
12.07.1991		
Declaration of the PhD student's contribution		
<i>For each category in the table below, please specify the PhD student's contribution to the article as appropriate (please do not fill in with names or x's)</i>		
Category	Minor contribution to the work <i>(please specify the nature of the PhD student's contribution)</i>	Substantial contribution to the work <i>(please specify the nature of the PhD student's contribution)</i>
Formulation of the conceptual framework and/or planning of the design of the study including scientific questions		Literature study, selecting reaction conditions, preparing paper outline and discussing key points with other authors
Carrying out of experiments/data collection and analysis/interpretation of results		Analyzing the literature to select appropriate information to include into reviews, carrying out the synthesis of all catalysts, performance of catalysts characterization such as nitrogen physisorption, SEM, TEM and testing the performance of the catalysts. Collecting data and interpreting the results
Writing of the article/revising the manuscript for intellectual content		Writing the initial draft, applying the comments and corrections from the co-authors and revising it continuously. Preparing the final draft.
Signatures		

Office for PhD and Continuing Education
March 2020 | page 3/3

Technical University
of Denmark



Title of article			
Pd Nanoparticles Encapsulated in Mesoporous HZSM-5 Zeolite for Selective One-Step Conversion of Acetone to Methyl Isobutyl Ketone			
Journal/conference			
Journal			
Author(s)			
Rouzana Pulikkal Thumbayil, Jerrik Mielby, Søren Kegsnæs			
Name (capital letters) and signature of PhD student			
ROUZANA PULIKKAL THUMBAYIL			
PhD student's date of birth			
12.07.1991			
Date	Name	Title	Signature
3/3-2020	Rouzana Pulikkal Thumbayil	PhD student	
3/3-2020	Jerrik Mielby	Senior Researcher	
3/3-2020	Søren Kegsnæs	Professor	

Please note that by signing this declaration, co-authors permit the PhD student to reuse whole or parts of co-authored articles in their PhD thesis, under the condition that co-authors are acknowledged in connection with the reused text or figure.



Declaration of co-authorship at DTU

If a PhD thesis contains articles (i.e. published journal and conference articles, unpublished manuscripts, chapters, etc.) written in collaboration with other researchers, a co-author statement verifying the PhD student's contribution to each article should be made.

If an article is written in collaboration with three or less researchers (including the PhD student), all researchers must sign the statement. However, if an article has more than three authors the statement may be signed by a representative sample, cf. article 12, section 4 and 5 of the Ministerial Order No. 1039, 27 August 2013. A representative sample consists of minimum three authors, which is comprised of the first author, the corresponding author, the senior author, and 1-2 authors (preferably international/non-supervisor authors).

DTU has implemented the Danish Code of Conduct for Research Integrity, which states the following regarding attribution of authorship:

"Attribution of authorship should in general be based on criteria a-d adopted from the Vancouver guidelines¹, and all individuals who meet these criteria should be recognized as authors:

- a. Substantial contributions to the conception or design of the work, or the acquisition, analysis, or interpretation of data for the work, *and*
- b. drafting the work or revising it critically for important intellectual content, *and*
- c. final approval of the version to be published, *and*
- d. agreement to be accountable for all aspects of the work in ensuring that questions related to the accuracy or integrity of any part of the work are appropriately investigated and resolved."²

For more information regarding definition of co-authorship and examples of authorship conflicts, we refer to DTU Code of Conduct for Research Integrity (pp. 19-22).

By signing this declaration, co-authors permit the PhD student to reuse whole or parts of co-authored articles in their PhD thesis, under the condition that co-authors are acknowledged in connection with the reused text or figure.

It is **important** to note that it is the responsibility of the PhD student to obtain permission from the publisher to use the article in the PhD thesis³

¹ International Committee of Medical Journal Editors – Recommendations for the Conduct, Reporting, Editing, and Publication of Scholarly Work in Medical Journals, updated December 2016

² DTU Code of Conduct for Research Integrity (E-book p. 19)

³ Many journals will allow you to use only the post-print version of your article, meaning the accepted version of the article, without the publisher's final formatting. In the event that your article is submitted, but still under review, you should of course use the latest submitted version of your article in your thesis. Always remember to check your publisher's guidelines on reuse of published articles. Most journals, unless open access, have an embargo period on published articles, meaning that within this period you cannot freely use the article. Check your publisher's rules on this issue.

Office for PhD and Continuing Education
March 2020 | page 2/3

Technical University
of Denmark



Title of article		
Dehydrogenation of bioethanol using Cu nanoparticles supported on N-doped ordered mesoporous carbon		
Journal/conference		
Journal (Manuscript)		
Author(s)		
Rouzana Pulikkal Thumbayil, David Benjamin Christensen, Jerrik Mielby, Søren Kegnæs		
Name (capital letters) and signature of PhD student		
ROUZANA PULIKKAL THUMBAYIL		
PhD student's date of birth		
12.07.1991		
Declaration of the PhD student's contribution		
<i>For each category in the table below, please specify the PhD student's contribution to the article as appropriate (please do not fill in with names or x's)</i>		
Category	Minor contribution to the work <i>(please specify the nature of the PhD student's contribution)</i>	Substantial contribution to the work <i>(please specify the nature of the PhD student's contribution)</i>
Formulation of the conceptual framework and/or planning of the design of the study including scientific questions		Literature study, selecting reaction conditions, preparing paper outline and discussing key points with other authors
Carrying out of experiments/data collection and analysis/interpretation of results		Analyzing the literature to select appropriate information to include into reviews, carrying out the synthesis of all catalysts, performance of catalysts characterization such as nitrogen physisorption, SEM, TEM and testing the performance of the catalysts. Collecting data and interpreting the results
Writing of the article/revising the manuscript for intellectual content		Writing the initial draft, applying the comments and corrections from the co-authors and revising it continuously. Preparing the final draft.
Signatures		

Office for PhD and Continuing Education
March 2020 | page 3/3

Technical University
of Denmark



Title of article			
Dehydrogenation of bioethanol using Cu nanoparticles supported on N-doped ordered mesoporous carbon			
Journal/conference			
Journal (Manuscript)			
Author(s)			
Rouzana Pulikkal Thumbayil, David Benjamin Christensen, Jerrik Mielby, Søren Kegnæs			
Name (capital letters) and signature of PhD student			
ROUZANA PULIKKAL THUMBAYIL			
PhD student's date of birth			
12.07.1991			
Date	Name	Title	Signature
3/3-2020	Rouzana Pulikkal Thumbayil	PhD student	
3/3-2020	Jerrik Mielby	Senior Researcher	
3/3-2020	Søren Kegnæs	Professor	

Please note that by signing this declaration, co-authors permit the PhD student to reuse whole or parts of co-authored articles in their PhD thesis, under the condition that co-authors are acknowledged in connection with the reused text or figure.